Petroleum Research 11 (2026) 361–398

Contents lists available at ScienceDirect

Petroleum Research

journal homepage: http://www.keaipublishing.com/en/journals/petroleum-research/

Review Article

Comprehensive permeability-transform solutions for shale and sandstones using data sets from around the globe

Ruud Weijermars [a,b,*]

[a] Department of Petroleum Engineering, College of Petroleum Engineering and Geosciences (CPG), King Fahd University of Petroleum & Minerals, KFUPM, Dhahran, Saudi Arabia
[b] Center for Integrative Petroleum Research (CIPR), College of Petroleum Engineering and Geosciences (CPG), King Fahd University of Petroleum & Minerals, KFUPM, Dhahran, Saudi Arabia

ARTICLE INFO

Article history:
Received 5 September 2024
Received in revised form
24 August 2025
Accepted 27 August 2025
Available online 3 October 2025

Keywords:
Permeability transforms
Permeability-reduction factor
Kozeny-Carman
Tortuosity
Shale
Sandstone

ABSTRACT

This study uses 13 proprietary data sets from sedimentary basins around the globe to constrain the permeability and porosity ranges occupied by clastic rocks (sandstones and shale). The combined data sets represent a total sample size of 21,767 data pairs of measured porosity and permeability. The data are combined in various ways and analyzed in considerable detail, in what is presently assumed the most comprehensive permeability analysis of clastic data sets. First, comprehensive porosity-permeability transforms are plotted with the aim to understand how well the two quantities actually correlate, and what may be the root cause(s) of the huge variation in their correlation. The analysis of the empirical data is embedded in a review of prior work related to permeability transforms. The Kozeny-Carman relationship is revisited and a modified scaling approach is proposed. First, it is shown how hydraulics of pore tubes of various shapes and tortuosity relate to macroscopic permeability. The key scaling factor, called here the permeability-reduction factor, β/τ, is the ratio of the coefficient of hydraulically effective pore space, β, and the tortuosity, τ. Whereas it is concluded that the porosity is a very poor predictor of the permeability, there appears to exist a close relationship between the permeability-reduction factor and the permeability, confirming the fundamental physical nature of β/τ as an excellent predictor of hydraulic transmissibility in porous media made up of sedimentary mineral aggregates. The inferred relationship provides the basis for a new method to construct permeability transforms, from bootstrapped data sets, using Monte-Carlo simulation.

1. Introduction

Permeability of porous media is an important attribute in material science, mechanical engineering, petroleum engineering, hydrogeology, geothermal engineering, environmental engineering, and geotechnical applications (Bear, 1972; Oliver et al., 2008). Models of fluid migration in subsurface reservoirs and the response to related well interventions critically depend on reliable permeability inputs (Sun and Zhang, 2020). Likewise, the productivity index of extraction wells (for petroleum fluids such as oil and gas, water and geothermal fluids; Guo, 2019) and the injectivity index of injection wells (for wastewater disposal, carbon dioxide sequestration, and hydrogen or natural gas storage; Afagwu and Weijermars, 2024a) all are critically dependent on having an accurate permeability value for the completion zone where the fluid flow between the well system and the reservoir occurs.

Darcy's Law indicates that the flow rate, q_j, into a well is linear proportional to the permeability, k_{ij}, of the reservoir it draws from by imposing a certain pressure gradient, $\partial_i P$ (Darcy, 1856):

$$\partial_i P = -\frac{\mu}{k_{ij}} q_j, \tag{1a}$$

Darcy's Equation (1a) scales the macroscopic fluid transmission rate vector components by the ratio of the fluid viscosity scalar and the permeability tensor in a quantified response to the

* Department of Petroleum Engineering, College of Petroleum Engineering and Geosciences (CPG), King Fahd University of Petroleum & Minerals, KFUPM, Dhahran, Saudi Arabia.
E-mail address: ruud.weijermars@kfupm.edu.sa.

Peer review under the responsibility of Editorial Office of Petroleum Research.

https://doi.org/10.1016/j.ptlrs.2025.08.006
2096-2495/

components $\partial_i P$ of the pressure gradient vector imposed on the porous medium. The fluid viscosity, μ, does not affect the permeability measure but reservoir sections with a certain permeability and a low viscosity fluid will produce at higher flow rates at the wellhead then when the fluid is more viscous (for example due to near-wellbore condensation), assuming the same pressure gradient is imposed by the well system.

Darcy's Law assumes strictly laminar flow, and no turbulence may occur in the pores due to the turbulence factor ξ being very small, which is when the inertia term in the below pressure balance equation becomes negligibly small:

$$\partial_i P = -\left(\frac{\mu}{k_{ij}} q_j + \xi \rho q_j^2\right), \tag{1b}$$

Crucially, the permeability tensor, k_{ij}, represents the inferred scaling quantities measured directionally under dynamic flow. One should realize that permeability is a material response quantity. While porosity is a scalar quantity – not affected by the direction of flow – being only a measure of static pore space, permeability is a dynamic scaling parameter of fluid transmissibility. Fluid commonly needs to be flown through the rock to infer a reasonably precise global value for the permeability (Darcy, 1856).

Rather than conducting cumbersome flow-tests in a Darcy flow-cell, the Kozeny-Carman (KC) relationship was developed in attempts to predict permeability based on geometric inputs only (grain size, porosity and tortuosity). Building forward on KC-type of reasoning, numerous studies have attempted to establish a correlation between porosity and permeability. The reason is that the porosity is relatively easy to measure as compared to the permeability. The porosity can be measured without testing the fluid transmission rate. For example, porosity can be directly measured on core samples using a variety of *direct methods*, such as fluid saturation, helium injection, or nuclear magnetic resonance (NMR), which can establish the ratio of pore volume to total volume of the rock (Liu et al., 2022). Separately, *indirect methods* include wire line-logs of resistivity, density, and sonic velocity, which correlate to porosity via empirical equations (Zhao et al., 2021). Acoustic impedance and seismic velocity in rock layers can also be used to infer the porosity (Kassab and Weller, 2011).

In the permeability transform approach, the permeability is assumed isotropic and no longer direction-dependent, essentially reducing the tensor quantity k_{ij} to a scalar quantity k, which can be correlated to other scalar quantities, like porosity.

The permeability and its spatial variation in a reservoir can be estimated (independently from the porosity) using a variety of methods (Weller et al., 2015; Weller and Slater, 2015). Wireline logs, core analysis, production data, pressure build-up data and tracer tests may all provide estimates of reservoir permeability near the wellbore. However, the principal methods include the following three approaches: (1) Laboratory measurements to construct porosity-permeability transforms used as a baseline to subsequently predict from porosity measurements (only) what will be the associated (or corresponding) permeability, (2) The computation of permeability using Kozeny-Carman type of equations, using the porosity as a principal input parameter, and (3) In situ well-tests. Each method will be reviewed in some detail to embed in context the new method proposed here for analytically estimating the permeability of porous media.

As a baseline for the model development, the present study uses empirical data comprising 21,767 pairs of measured permeability and porosity (see Appendix A). These data come from various sources and were either availed to the author (1) for research purposes, and (2) for petroleum engineering educational capstone projects, or (3) publicly available. The latter applies to data from the Hooray sandstone and other aquifers in the Great Artesian Basin (GAB) of Australia. The GAB data set comprises 18,646 data pairs. The non-GAB data (3121 data pairs) come from cores taken in pilot wells from oil and gas reservoirs, in both sandstones and shale formations. Exactly 2400 samples came from 7 conventional sandstone formations (Oseberg, Troll, Hugin, Tarbert, M65-M66, Flag Sandstone and Fontainebleau). Separately, 4 datasets come from three unconventional shale formations (Bakken, Eagle Ford and Wolfcamp), jointly providing 721 data pairs. Analyzing these data in concise fashion revealed unique insights, as will become apparent in the course of the present analysis. The data sets are described in some detail in Appendix A. In order to analyze the data in a meaningful way, it is first necessary to develop a theoretical framework against which the data will be tested. This framework is provided in Sections 2 and 3.1-3.3. The data are next analyzed in depth in Sections 3.4 and 4.

The present analysis embodies a new approach for the theoretical estimation of permeability of rocks and sedimentary aggregates, based on the natural range of possible pore structures, grain-packing models and grain shapes. Topological insights are used to derive a novel theoretical expression, relying on the geometrical characterization of the pore morphology in the rock samples. The new approach advocated here shares communality with prior KC-approaches, but also claims to be different in critical aspects, as explained in detail later in this study. In the course of this research project, a mature workflow for operational implementation has been developed. The workflow steps and technical actions are given in Table 1.

Although the samples used are limited to data from consolidated, clastic sedimentary rocks, the method is claimed to be universally valid; it can be applied to estimate the permeability for any porous medium. The method can also easily be extended to apply to porous media with transversely isotropic permeability (see discussion section).

2. State-of-the-art review

In order to embed the analysis method of permeability transforms developed in the current study in historic context, a brief review of existing methods for estimating rock permeability will be given below. By far the most reliable method is the measurement of permeability in physical laboratory experiments by placing drill-core samples in a core-flood vessel (Krause et al., 2011a, b). Such core-flood experiments are costly, and time-consuming, while resulting in only a limited number of data points. However, the vast dataset analyzed later in this study will provide important grounding in real-world data. Before discussing permeability measurements and transforms, it seems warranted to first provide a theoretical basis for later translation attempts of pore structure to permeability behavior, by reviewing the state-of-the-art. The subject is vast and only the most essential studies are cited here, given the need for practical conciseness.

2.1. Pore structure characterization

In naïve views, the permeability of a porous medium is intuitively assumed to be connected to porosity. This intuition appears very misleading; this will be particularly apparent if one evaluates the content of Section 2.3. Before moving to the concept of permeability, we shall consider the nature of rock porosity in granular, clastic rocks that are the subject of the present analysis (Sections 2.1 and 2.2).

If one tries to infer 3D porosity from 2D slices through rocks, as often done when visually inspecting rock samples in thin sections

Table 1
Workflow steps and technical actions for analyzing classic porosity-permeability transforms and developing a new type of permeability transform involving the permeability-reduction factor.

Step	Technical Action
1	Understand physics of pore systems in clastic sediments
2	Understand detailed role of porosity and permeability in flow through porous media
3	Understand the nature of porosity-permeability transforms
4	Review methods of measuring porosity and permeability
5	Review prior attempts to correlate pore space and permeability
6	Rigorous model adaptation: Less focus on porosity and more focus on typical pore sizes and stream tube topology
7	Introduction of the permeability-reduction factor
8	Examination of data sets (A) Conventional reservoirs (sandstones); (B) Unconventional reservoirs (shales)
9	Translation of classic porosity-permeability transforms to permeability-reduction factor versus permeability transforms
10	Probabilistic modeling of porosity-permeability transforms using lessons learned from permeability-reduction factor plots
11	Implementation of resulting permeability and porosity distributions (with correlation dependency) in reserves estimation and storage capacity estimations of field projects to determine probabilistic reserves and storage capacity sub-classification (P90, P50, P10), in line with SPE guidelines (PRMS, 2024; SRMS, 2024).

using a polarized light microscope, a high risk of erroneous conclusions arises, as can be succinctly explained by relating insights from idealized 3D-sphere packing studies to 2D-circle packing studies.

Kepler first showed, in 1611, that unit spheres packed in a regular face-centered (hexagonal) packing (Fig. 1a) occupy $\pi/\sqrt{18} = 74.4048\%$ of the available 3D space, leaving a complementary 3D-void of 0.255952 percent. Not until Hales (2005) was conclusive mathematical proof given that hexagonal packing has indeed the highest material density amongst all possible ordered sphere-packing structures, something Gauss had already conjured in 1831 (without conclusive proof). Consequently, a porosity of ~0.256 is the minimum possible with tightly packed spherical grains of equal radius. Slightly altering the hexagonal packing of the spheres into a regular, body-centered arrangement (Fig. 1b), results in a loosening up with 68% of the 3D-pace occupied by the spheres and interstitial porosity of 0.32. Finally, the packing efficiency of unit spheres in a regular cubic packing (Fig. 1c) is the lowest, having a 52.36% mass occupancy, with a relatively large complementary porosity of 0.476. Considering sphere packing models we must observe porosity limits of 0.256 for hexagonal, to 0.32 for body-centered and 0.476 for cubic packing of spherical grains (Table 2).

Spherical granular aggregates in nature, even when of approximately well-sorted uniform grain size, are more likely to occur in a random packing order rather than in regular packing structures. Such randomly packed spheres have a packing efficiency of about 63.5%; the implied porosity is 0.365 (Campos et al., 2023; Wu et al., 2003). A summary of the range in porosity is given in Table 2.

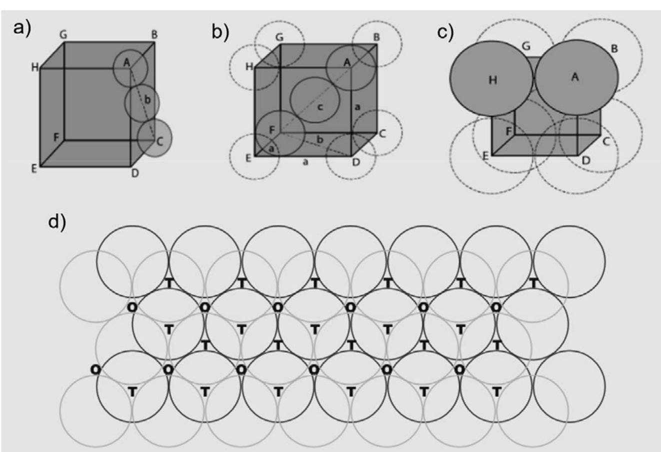

Fig. 1. (a)–(c) Three principal regular packing orders for equal spheres: face-centered hexagonal, body-centered and cubic. (d) Projection of hexagonal packing with pore space seen as tetrahedral voids or octahedral voids, depending upon position.

When we next consider granular aggregates of unequal spheres, limiting our attention first to bimodal grain size distributions with one set of radii much smaller ($r_2 < 0.4142r_1$), it becomes possible to arrange the larger spheres in a closely packed arrangement, with the smaller spheres fitting fully in the octahedral and tetrahedral gaps (Hudson, 1949). For such cases the minimum porosity of 0.256 obtained for regular dense hexagonal packing still applies, and for random packing, the porosity again approaches 0.365 (Table 2). Differently, bimodal grain distributions with radii r_2 of the smaller spheres ranging between $0.4142r_1<r_2<r_1$ will outsize the octahedral holes. However, for grain ratios $0.4142r_1<r_2 < 0.659786r_1$, denser packing than for uniform unit spheres appears actually possible (Marshall and Hudson, 2010). When the range of grain sizes is very large, very low porosity packing may result (Laat et al., 2014; Oquendo-Patiño and Estrada, 2020).

There exists an expansive body of literature on spherical and non-spherical grain-packing (Rodrigues et al., 2023). The introductory insights and the summary of Table 2 can be expanded to include maximum packing densities of basic 3D-shape approximations of mineral aggregates. Table 3 uses results from mathematical optimization studies, showing that, for example, cubes in random packing will have a maximum density of ~0.78 (Li et al., 2010). However, for general rectangles, the random packing will be less dense, getting as low as 0.56 (Liu et al., 2017a, b), implying maximum porosity (up is 0.44). Applying this to shale, one must realize that after deposition the clay deposit is typically loaded by overlying sediments, which compresses the pore spaces between the relatively flexible clay minerals, and the porosity is significantly reduced (max porosity measured is 0.15; see Section 2.4).

2.2. *Translating voids in 2D sections to 3D porosity*

If one tries to infer 3D porosity from 2D slices through rocks a high risk of erroneous conclusions arises, as can be succinctly explained by reviewing 2D-circle packing studies, and then relating them to the 3D-sphere packing insight summarized in Tables 2 and

Table 2
Packing of equal sphereas; lso valid for bimodal sphere sizes with ($r_2 < 0.4142r_1$).

Packing Type	Density	Porosity
Regular simple cubic	0.524	0.476
Random	0.635	0.365
Regular body-centered	0.680	0.320
Regular hexagonal	0.744	0.256

3. For example, Lagrange showed in 1773 that hexagonally packed circles occupy 90.69% of the section in view, leaving a 'pore'-space fraction of only 0.0931 (Fig. 2a). However, if we now compare this result with the minimum porosity of 0.256 occurring for hexagonally packed spheres (Table 2), we can conclude the following. If we measure a minimum porosity of 0.0931 in a 2D cross-section of tightly fitting, spherical grains with equal radii (Fig. 3a), the actual porosity in 3D may be 0.256 (Table 2), which is ~2.75 times larger than what appears in the 2D section.

Similarly, for rocks made up of spherical pore spaces (Fig. 2b), like in dissolved ooids (Fig. 3b), the 2D section is again deceptive, but the prior logic now needs to be reversed, because the circles are the pores and the ridges in between is the rock mass. Tightly hexagonal-packed pores occupy 90.69% of the space in a 2D-section view (Fig. 2b), which means the porosity may appear as high as 0.9069. But we know that for the hexagonal packing of spheres a density maximum of about 74.4048% occurs, which means that the maximum possible porosity is 0.744, not 0.9069; the 3D pore space reality is ~0.82 times smaller than the apparent porosity appearance in a 2D section.

Some practical implications based on the geometrical considerations of pore-space constraints are as follows:

- Rocks like sandstones made up of randomly packed spherical mineral grains, or limestone made of solid ooids (Fig. 3a) will have a 3D porosity no less than 0.265, but misleadingly may appear in equatorial 2D-sections as having an apparent porosity of only 0.0931 (Fig. 2a). However, arbitrary cross-sections are unlikely to show the lowest 0.0931 apparent pore space in 2D sections, and likely may show 'porosities' between 0.0931 and 0.265.
- Rocks made of hexagonally packed spherical pores (see Fig. 3b) may have a maximum 3D porosity of 0.744, but misleadingly may appear with as much as 0.907 apparent pore space in equatorial 2D-sections (Fig. 2b). However, arbitrary 2D cross-sections showing thickened pore walls (Fig. 3b), will not necessarily exhibit the maximum possible 0.9069 apparent porosity, but something in between 0.9069 and 0.744, or if the pore walls are thickened, still lesser porosities are possible.
- Rocks like silts and shale made up of angular (Fig. 3c) and platy minerals (Fig. 3d) allow for tighter packing than spherical aggregates. Empirical data show that in shale the porosity may be as low as 0.06 (see later).

We still see studies constructing porosity-permeability transforms based on 2D-sections of apparent porosity (Saxena et al., 2017), and in machine learning solutions (Hall et al., 2022), without any reference to the misleading porosity views offered by 2-D sections, which calls for caution. On the other hand, accurate methods have been developed to estimate permeability from 2D sections (Lock et al., 2002).

Table 3
Packing of equal sized basic shapes (after Li et al., 2010).

Object Shape	Ordered Packing		Random Packing	
	Density	Porosity	Density	Porosity
Sphere	0.741	0.259	0.64	0.36
Ellipsoid	0.771	0.221	0.74	0.26
Tetrahedron	0.782	0.218	0.680	0.32
Cone	0.785	0.215	0.67	0.33
Cylinder	0.91	0.09	0.72	0.28
Cube	1	0	0.78	0.22

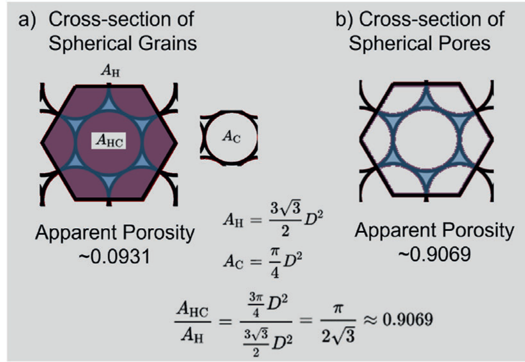

Fig. 2. (a) Cross-section at level of grain equators in hexagonally packed spheres; apparent porosity in 2D is 0.093. (b) For dissolved ooid rock pores, the complementary apparent porosity of 0.907 would occur. Arithmetic shows Lagrange's computations of various surface areas resulting in the space of 0.9069 left between the tightly fitting circles.

2.3. Interconnected porosity pathways

For a rock to be permeable, the pores need to be interconnected in order to allow for fluid transmission. Not all pore space may accommodate fluid flow, but the portion that participates in flow is referred to as the interconnected or hydraulically effective porosity, where pores are connected enough to accommodate fluid flow across the rock formation. The effective porosity is an imperative parameter still required as a key input parameter in reservoir fluid-withdrawal and injection studies, together with the permeability (Satter and Iqbal, 2015).

To investigate how local flow paths result from certain permeability and pore space arrangements, several principal types of approaches are possible: (1) flow path studies through physical (or simulated) micro-fluidic apparatus (Fig. 4a and b), (2) Equivalent numerical simulations of flow through synthetic regular pore-space arrangements (Fig. 4c), (3) Visualization of flow paths through structural domains with assigned local porosity and/or permeability variations (Fig. 4d and e), and (4) Multi-phase pore-scale simulations using imported pore geometry obtained from micro-CT (computerized tomography) scans of real rocks (Alpak et al., 2016; Frank et al., 2018a, 2018b, 2018c).

Detailed flow simulations with systematic variations in permeability and porosity, while examining the resulting flow paths and travel rates, led to the formulation of important practical rules in a prior study (Zuo and Weijermars, 2018). The distinct impacts of the porosity and permeability on fluid flow became apparent and was captured in two rules: (1) An increase in permeability *decreases* the time-of-flight (or duration of fluid transfer) across the reservoir space, whereas an increase in porosity *increases* the time-of-flight of fluid towards a well-system (due to storage effects); (2) The permeability uniquely *controls* the flow path of fluid migration in porous media; however, local porosity variations *do not at all affect* the path of fluid flow. These rules are supported by a very detailed, systematic series of computational flow models (Zuo and Weijermars, 2018).

In short, porosity impacts the flow rate (together with the permeability), but not the flow path, which is exclusively controlled by the permeability alone. The flow-rate dependency is also apparent if we transpose Darcy's Law of Eq. (1a) for the fluid discharge rate, q_j, seeping into the well space (or flux through unit

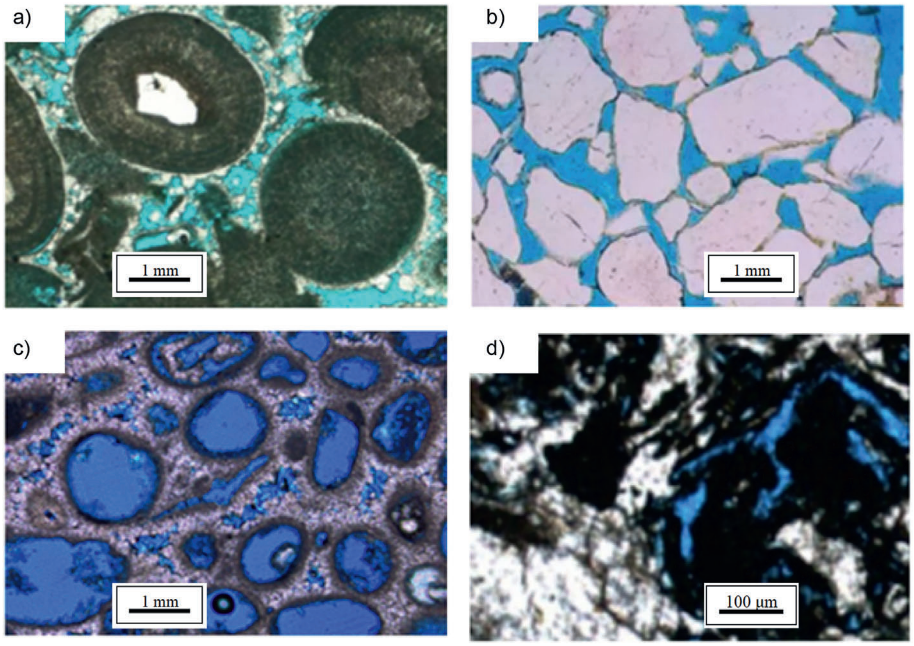

Fig. 3. Examples of apparent pore space (blue shades) as seen in thin sections of rocks. (a) Ooid limestone, (b) Angular quartz grain sandstone, (c) Dissolved ooids in limestone (courtesy Ahmad Al-Bader), (d) Shale (Luo et al., 2021). Blue shaded regions are pore space.

area out of the well's rock face) to the flow rate, u_j, in the reservoir space using Dupuit's formula, $q_j = \phi u_j$ (Phillips, 1991):

$$u_j = -\frac{k_{ij}}{\mu}\frac{\partial_i P}{\phi}, \tag{2}$$

Rather than assuming generalized permeability and porosity parameters, as is the case in commercial simulators, we have now the capacity to CT-scan core samples to characterize the 3D-pore structure of specific core sections, which avoids the simplifications adopted in synthetic pore-network models. Next, the digitized 3D-pore structure can be used as a starting point for modeling the fluid flow through precisely that specific pore structure, to study detailed pore-scale flow phenomena and compute the macroscopic permeability (Alpak et al., 2016). However, such models are computationally rather intensive, thus costly, while still providing only a snapshot of what happens in a particular portion of the CT-scanned rock sample. Also, the detailed CT-scan based flow models, seemingly highly sophisticated and highly precise, are at the same less useful for reservoir-scale studies of fluid withdrawal and pressure depletion, for which upscaled, global parameters for permeability, porosity, and fluid compressibility are needed.

Of course, all model approaches are merited and help improve our understanding of pore-size-driven flow, such as accounting for capillary forces and viscosity-dominated flow, or revealing phenomena like non-Darcy flow associated with a higher Reynolds number that might occur in near-wellbore regions and hydraulic fractures of gas reservoirs, with development of local vortices (*i.e.*, Eq. (2) rather than Eq. (1) applies) which lower the efficiency of fluid transmission (Cheng et al., 2019).

2.4. Porosity-permeability transforms

For reservoir-scale simulations aimed at capturing a realistic range of spatial variability in the permeability and porosity, core samples are taken from vertical pilot (appraisal or delineation) wells in the reservoir zone of interest. The well-log data give initial information on the spatial porosity variation. The readings can be complemented with permeability measurements in physical laboratory experiments, placing the drill-core samples in flood vessels or flow cells. Based on the collected measurements of pairs of porosity and permeability, so-called porosity-permeability transforms can then be constructed.

Fig. 5 shows a compilation of a selected subset of *conventional* sandstone formations (Fontainebleau, Troll, Tarbert and Miocene M65/M66), and *unconventional* shale formations (Eagle Ford, Wolfcamp and Bakken). The construction of such porosity-permeability transforms is very useful to visualize how porosity relates to permeability (as averaged for the individual core-samples), and represents the variation encountered in the formations. The primary data of the 8 formations plotted in Fig. 5 comprised 338 data points. Further details, also for additional data sets introduced later in this paper, are given in Appendix A.

One should note from Fig. 5, that while the porosity varies in practical sense (using a lower limit of 0.01), over only about one order of magnitude 10^{-2}-10^{-1}, the permeability varies over 13 orders of magnitude 10^{-9}-10^{4} mDarcy. The porosity, therefore, is a very poor gauge, largely insensitive to the immense variation in permeability, which persists even when we would focus on samples from just one formation. Also apparent is the dichotomy in the transform fields occupied by conventional sandstones and shales. This dichotomy is in no way following from the porosity variation, but ultimately can be explained by differences in grain shape and pore size, intrinsically related to sedimentary facies and degree of diagenetic compaction (see Section 5.2).

2.5. Well-testing methods

In addition to extracting cores from appraisal wells or pilot wells, the average reservoir permeability can be estimated by conducting in-situ flow tests for the target-section of the reservoir.

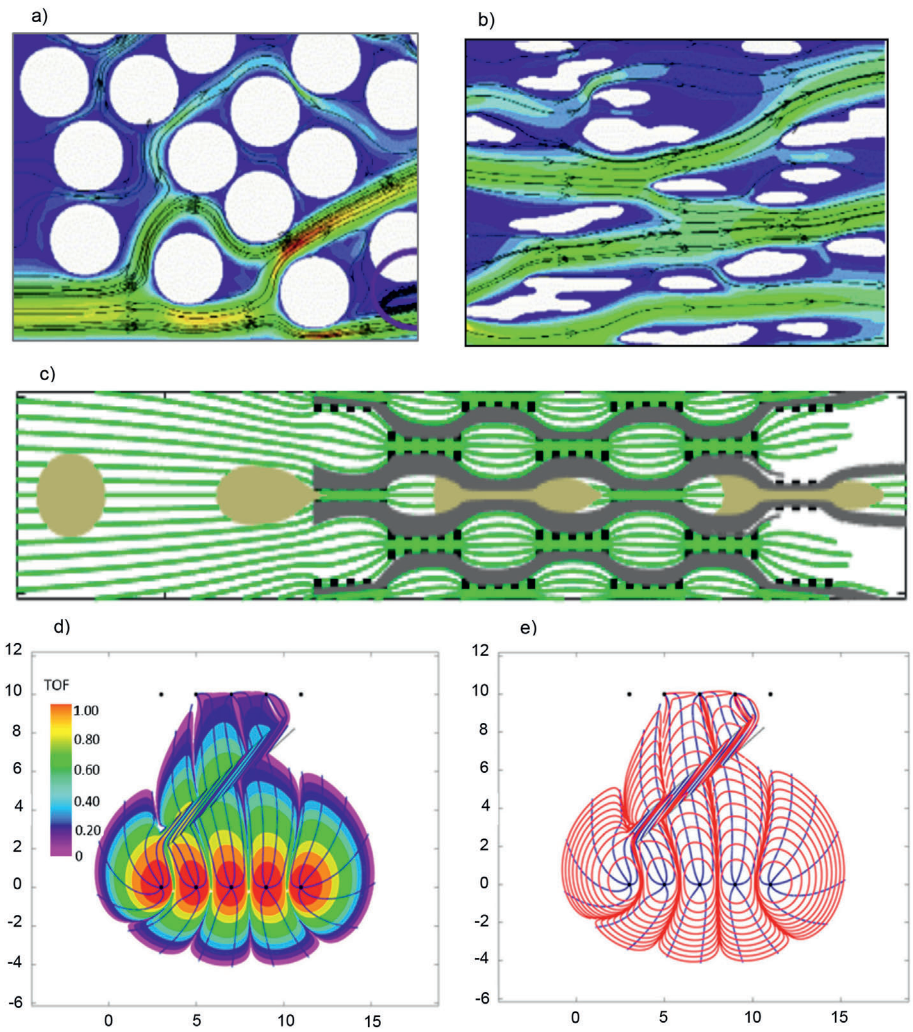

Fig. 4. (a) Synthetic 2D pore structure with flow simulation showing high speed flow paths with the shortest time-of-flight (green and red colors) as compared to the slow regions (blue) around spaced cylinders, which in a thin slice is equivalent to a non-equatorial section of randomly packed spheres (after Cheng et al., 2019). (b) Synthetic pore structure resembling platy mineral aggregate, with preferential flow paths controlled by pore structure, as flow is entered uniformly from the left (after Cheng et al., 2019). (c) Synthetic 2D pore structure with 2-phase flow showing how oil blob stretches when passing through narrow pore throats. Flow paths are marked with green dye (after Weijermars and Khanal, 2019a). (d,e) Flow diversion between 5 injectors (lower row dots) and 5 producer wells (upper row dots) separated by a slanted fault zone of high permeability but same porosity as surrounding matrix. The permeability of the fracture zone is 10 times that of the ambient reservoir space. Left image show time-of-flight (TOF) contours. Right image shows detailed TOF contours (red curves) and flow paths (blue curves). Units along map margin are non-dimensional length (after Weijermars et al., 2020).

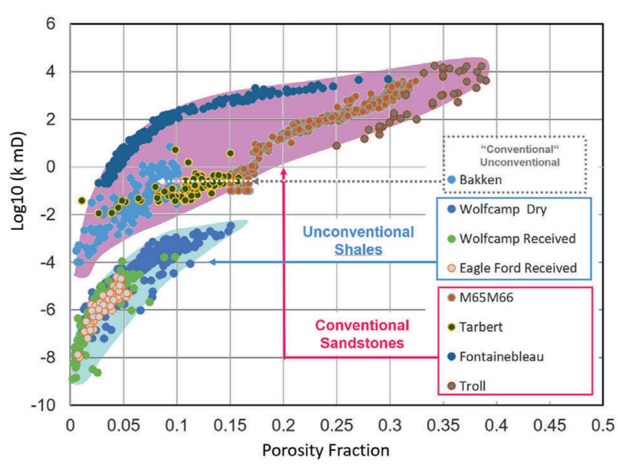

Fig. 5. Comprehensive set of porosity-permeability transforms for a series of formations. Vertical scale is permeability in Log10 mD and horizontals scale is porosity fraction of the rock. More details are given in Appendix A.

Such well-tests are extremely costly to perform. The flow rate of fluid from the reservoir into the well over a certain wellbore section is used to estimate the permeability of the reservoir rock from which the fluid is extracted. The procedure essentially uses an analytical solution for the pressure transient $P(r)$ initiated from the well system, also known as the well-test equation (Horne, 2005):

$$P(r) = P_0 - 141.2 q_{WH} \frac{B_0}{2\pi h} \frac{\mu}{k} \ln\left(\frac{r}{r_w}\right) \tag{3}$$

where, r_w, is the well radius and $r = 2.434x10^{-12}\sqrt{kt/(\phi\mu c_t)}$ the radius of investigation for radial cylindrical reservoir system to understand the tested cylindrical volume at a given time, t, during transient tests. Other parameters in Eq. (3) are the reservoir thickness, h, well rate at the wellhead, q_{WH}, original reservoir pressure, P_0, formation volume factor, B_0, viscosity, μ, and total compressibility, c_t.

Over the short duration of a well test (a few hours) one may assume an approximately constant well rate at the wellhead. The pressure drawdown $P(r)$ can be measured with downhole pressure-gauges and the other parameters like wellbore radius, r_w, original reservoir pressure, P_0, and formation volume factor, B_0, are known, so the permeability can be estimated with some provision for uncertainty such as well-skin factor. It is beyond the present study to review the method in any detail, but a vast body of literature exists, describing the general methodology (Zimmerman, 2018). Recently, an alternative solution to the well-test equation has been proposed for practical use in well-testing assuming a constant bottom-hole pressure (Afagwu and Weijermars, 2024b). Separately, a series of specialized tests such as leak-off tests in response to well shut-in, pressure transient and rate transient analysis, and diagnostic fracture injection tests (DFIT) also can provide permeability estimations (Liu and Ehlig-Economides, 2018; Zanganeh et al., 2020; Al-Shaikh and Weijermars, 2025). However, the estimates are dependable on other uncertain parameters and are not further discussed here.

3. Model development

By far the most accurate method to estimate the permeability of solid rocks and granular aggregates is by core flooding (Section 2.4), which requires a vast number of tests to obtain representative value ranges that capture the spatial variability of the permeability across the reservoir space of interest. The procedure is both costly and time-consuming, because it involves (1) the drilling of numerous pilot wells, (2) extraction of cores from the wells, and (3) core-flooding tests combined with porosity measurements in a dedicated laboratory. There also appears a practical threshold where shale permeability (Fig. 5), which is in the nanoDarcy range, cannot be measured on reasonable time-scales, and only with impractical inaccuracy, in concurrent flooding equipment.

Although coring and petrophysical testing are routine operations in oil companies, reducing the number of samples to be analyzed without reducing accuracy would be desirable. The method developed in this study offers such optimization of the workflow to obtain reliable porosity-permeability transforms from only a limited set of data. The key equations are developed in Sections 3.2-3.3 and will be later augmented by a probabilistic data generation method to deliver amplified data sets. This procedure is physics-based and should not be confused with machine learning or data analytics, which is currently still only rarely physics-grounded. Critical input parameters for the new model are outlined in Section 3.4.

3.1. Traditional Kozeny-Carman models

Because of the ease to measure porosity in rock samples from outcrops and cores, efforts have been made by numerous authors to derive theoretical relationships that predict the permeability analytically, based on porosity and some additional parameters inferred from empirical data. The Kozeny-Carman relationship is such a theoretical model, based on Poiseuille flow and Darcy's Law. The solution path was first explored by Kozeny (1927) and then refined by Carman (1937, 1938a, b, 1939, 1956). Over time, numerous authors have attempted modifications (see reviews in Chapuis and Aubertin, 2003; Costa, 2006; Henderson et al., 2010; Nomura et al., 2018). However, arguably no fundamental conceptual changes to the original approach have been proposed.

A frequently used form of the Kozeny-Carman equation states (Mavko et al., 2009):

$$k=\frac{d^2\phi^3}{72\tau^2(1-\phi)^2}, \tag{4}$$

with permeability, k, characteristic grain size, d, and porosity, ϕ, and tortuosity, τ (Fig. 6). Equation (4) cited here is commonly used to empirically match porosity-permeability transforms to data points. Examples are abundant for data sets such as Fontainebleau sandstone (Bourbie and Zinszner, 1985) or Finney pack (Finney, 1970). Note that a Fontainebleau data set of 165 data pairs was included in Fig. 5 and will be further analyzed later in this study.

Sidestepping grain size and tortuosity estimations, empirical matches to porosity-permeability transform data can be produced using parameters akin to those used in Eq. (4), but much simplified (Rodriquez et al., 2004):

$$k=c_e\frac{\phi^{n+1}}{(1-\phi)^n}, \tag{5}$$

where c_e (unit m^2) and n (non-dimensional) are empirical matching parameters. There is a discussion among some practitioners of traditional Kozeny-Carman followers, that one should use a squared tortuosity (e.g. Paterson, 1983) or even cubed tortuosity (Chapman, 1981). However, such scaling of the tortuosity (a non-dimensional fraction) is not supported by others. During the review of this paper, the use of a squared tortuosity was mandated by one reviewer. Appendix B explains how squared tortuosity came into existence, and why its use in permeability transforms is deemed physically disputable. However, the dispute seems rather pointless, because everything stated in the present paper will conform to the view of the squared tortuosity 'school' when instead of using the tortuosity one uses the squared tortuosity factor $T=\tau^2$ (see Appendix B); everything stated in this study will equally apply.

3.2. Governing equations

Starting from the Poiseuille and Darcy flow solutions, a major insight is immediately obtained by equating the Poiseuille solution for a circular capillary and Darcy's Law. Both solutions are scaled through the pore capillaries of interest. In below examples, there is no difference between the pore tube radii, r_p, used in Poiseuille and Darcy's solution:

$$\text{Poiseuille}:\nabla P=\frac{-8\pi\mu}{\pi r_p^4}Q \tag{6}$$

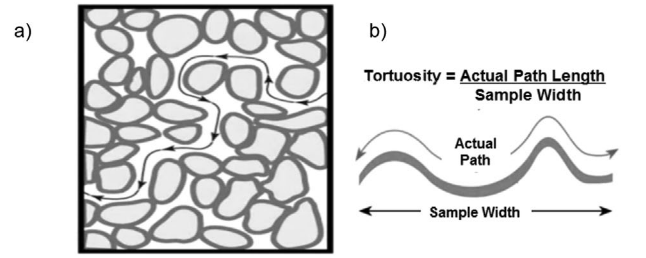

Fig. 6. (a) Flow path across pore space, similar to what is seen in Fig. 4a. (b) Principle sketch tortuosity definition.

$$\text{Darcy}: \nabla P = \frac{-\mu}{k\pi r_p^2} Q \tag{7}$$

$$\text{Permeability}: k = \frac{r_p^2}{8} = 0.125 r_p^2 \tag{8}$$

Eqs. (6)–(8), initially applied to single capillary tubes, are equally valid for bundles of such pores. The macroscopic permeability will be governed by the same parameters. Later, a correction is needed to account for the cross-sectional areas not participating in fluid transport (see Section 3.3), as well as for the tortuosity (see Section 3.3), which was not included in Eqs. (6)–(8).

Equation (8) reveals the fundamental nature of Darcy's scaling parameter, k, here initially approached by a model of straight capillary tubes. For decreasing pore tube radii, r_p, the permeability will decrease according to $r_p = \sqrt{8k}$, which explains the general curving trend seen in porosity-permeability transforms when plotted in log permeability-linear porosity graphs (like in Fig. 5). For rocks we have a wide range of permeability, ranging from 100 Darcy for very coarse sandstones to nanoDarcy for shale. Fig. 7a, b plots the typical permeability-values and the implied pore-throat radii, according to Equation (8). Even with values uncorrected for effective pore volume and tortuosity (see Section 3.3), Fig. 7b explains the trends seen in Fig. 5. And the data of Fig. 5 can be made to fit a straight regression trend when we apply a similar scale transformation as in Fig. 7a (see later).

The relationship of Eq. (8) can be generalized for other shapes of elementary flow tubes in porous media, introducing the cross-sectional area A:

$$\text{Poiseuille}: \nabla P = \frac{-\alpha\mu}{A^2} Q \tag{9}$$

$$\text{Darcy}: \nabla P = \frac{-\mu}{kA} Q \tag{10}$$

$$\text{Permeability}: k = \frac{A}{\alpha} \tag{11}$$

For example, when using Eq. (11) for a circular pore $A = \pi r_p^2$ and $\alpha = 8\pi$, one obtains $k = r_p^2/8$, exactly as was given in Eq. (8). Separately, for flow in circular cylindrical tubes with plaque deposits forming internal harmonic cusps and ridges, elegant solutions exist using the topological parameters, A and α (Mortensen et al., 2005). However, we confine our analysis here to only the most basic pore cross-sectional shapes, limiting our attention to circular, triangular, elliptical and rectangular cross-sections.

For arbitrary *triangular cross-sections*, characterized by triangle lengths a, b and c, we find (Mortensen et al., 2005):

$$A = \frac{a+b+c}{2}\left(\frac{a+b+c}{2} - a\right)\left(\frac{a+b+c}{2} - b\right)\left(\frac{a+b+c}{2} - c\right) \tag{12}$$

and

$$\alpha = \frac{200}{17}\frac{(a+b+c)^2}{\sqrt{\frac{1}{2}\left(a^2+b^2+c^2\right)^2 - \left(a^4+b^4+c^4\right)}} + \frac{40\sqrt{3}}{17} \tag{13}$$

from which k can be computed analytically using Eq. (11) in a spreadsheet. However, Eqs. (12) and (13) can be immediately simplified for practical application if we assume an equilateral triangle ($a = b = c$), which results in:

$$A = \frac{c^2}{4} = 0.25c^2 \tag{14}$$

and

$$\alpha = \frac{225\sqrt{2} - 1200}{17\sqrt{3}} = 6.73. \tag{15}$$

which gives the permeability as a function of the triangular base length, c, of the typical pore cross-section:

$$k \approx \frac{c^2}{27} \tag{16}$$

If we now use the center of mass of the equilateral triangle, occurring at height, h_c, from the mid-base of the triangle, we may substitute $c = 6h_c/\sqrt{3}$ in Eq. (16), we obtain a simplified expression:

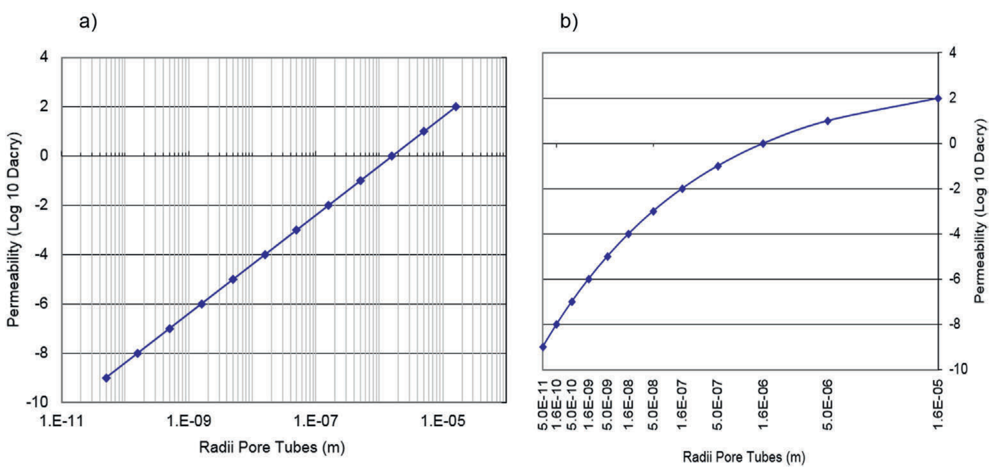

Fig. 7. Pore tube radii versus permeability according to Eq. (8) in log-log plot (a) and linear-log plot (b).

$$k \approx 0.44h_c^2 \tag{17}$$

By comparing Eqs. (8) and (17), one can immediately infer that flow through pore-tubes with equilateral triangular cross-section and inscribed circle of $r = h_c$ will have a permeability 0.44/0.125 = 3.52 times that of a circular cylindrical pore with radius r. The gain in permeability is due to the three corners providing extra flow space.

For pore tubes with an elliptical cross-section, characterized by semi-axes a and b, we find:

$$A = \pi ab \tag{18}$$

and

$$\alpha = 4\pi\left(\frac{a}{b} + \frac{b}{a}\right) \tag{19}$$

which then results in:

$$k = ab \bigg/ \left[4\left(\frac{a}{b} + \frac{b}{a}\right)\right] \tag{20}$$

For $a = b$ we find again the circular tube solution of Eq. (8).

For rectangular cross-sections, like slit-shaped pores, there exist more elaborate solutions (Delplace, 2018), but long and narrow slits can be approximated by the elliptical cross-section solution of Eq. (18). If we consider narrow slits with $b = na$ and $n \gg 1$, then it becomes practical to rewrite Eq. (20) as:

$$k = a^2 \bigg/ \left[4\left(1 + \frac{1}{n^2}\right)\right] \tag{21}$$

For $n \to \infty$, Eq. (21) asymptotically simplifies to:

$$k \approx \frac{a^2}{4} = 0.25a^2 \tag{22}$$

A careful comparison of Eqs. (8) and (22) immediately reveals that flow through narrow slot-shaped pore tubes, with walls separated by distance $2a$, have a permeability twice that of circular cylindrical pore tubes with diameter $2r_p$. However, the maximum flow rate in the center of circular cylindrical tubes reaches twice the average flow rate, whereas inside infinitely-wide rectangular slits (parallel plates) the maximum velocity is only 3/2 times the average velocity (Peszyński et al., 2018). This inverse relationship arises because in the case of the slits, the maximum velocity occurs over a wider front, with thinner boundary layers than for the circular conduits.

A more refined analysis reveals a rectangular slot with aspect ratio $b/a = 2.2693$ will have the same viscous friction loss as a circular tube of radius r_p (Delplace, 2018). This means that for rectangular ducts with aspect ratios $1 < (b/a) < 2.2693$, the maximum velocity will exceed twice the average velocity. Nonetheless, the permeability approximation of Eq. (21) will hold. Table 4 summarizes the simplifications made in the present analysis. Permeability relationships to pore shapes rather similar to those in Table 4 have been derived by Sisavath et al. (2001), using a different solution path with Saint-Venant and Aissen approximations, while utilizing mathematical analogy to torsion of prismatic elastic bars.

3.3. Generalization

So far, we have assumed that the geometry and dimensions of the various flow conduits were corresponding 1:1 to those used in a Darcy flow-test. There can be no logical objection to this simplified approach; the solutions obtained are mathematically correct and physically valid. However, if we are dealing with natural materials rather than synthetic ones with regularly fabricated pore shapes, we must consider several additional scaling parameters.

The relationship derived in Eq. (8) for circular pore tubes holds for any number of pore tube bundles with an assumed average radius. However, the pressure gradient applied to the core sample only corresponds to the pressure gradient in the capillary tube in case the core consists of basically one capillary (Fig. 8a). In practice, the capillary tube will have a radius smaller than the core (Fig. 8b), for which case the analytical permeability solution would need to include the porosity. The same holds when a larger number of capillaries act as the fluid transport conduits in the core material (Fig. 8c). The porosity is factored in for the cases of Fig. 8b and c, because Eq. (6) keeps ∇P unchanged, but for Eq. (7) one needs to use $\nabla P/\phi$ on the left-hand side instead of ∇P. Henceforth, the permeability will be given by $k = \frac{r_p^2}{8}\phi$.

However, Fig. 8c still is a highly idealized core model with perfectly aligned straight capillaries, all providing connected porosity. The capillary core model can be modified to account for (1) blocked capillary tubes (Fig. 9a), and (2) tortuous cylindrical tubes (Fig. 9b) rather than assuming straight cylindrical tube pore geometry.

The hydraulically effective fraction of the pore volume, ϕ_{EFF}, is here related to the regular porosity represented by ϕ_{REG}, via the scaling factor β:

$$\phi_{EFF} = \beta\, \phi_{REG} \tag{23}$$

The factor β gives the unblocked fraction of the porosity represented by the capillary tubes with the hydraulically effective portion of the to the regular porosity, ϕ_{REG}. In effect, β makes sure only cross-sectional area occupied by capillary entrances, able to accommodate fluid flow, is considered. In all cases, $0 \le \beta \le 1$.

Separately, we must account for the reduction in the pressure gradient across flow tubes due to their tortuosity, τ, using:

$$L_{ACTUAL} = \tau L_{MIN} \tag{24}$$

The observed or estimated actual flow path length, L_{ACTUAL}, normalized by the shortest possible travel distance, L_{MIN}, corresponds to the tortuosity (Fig. 6). The tortuous length divided by the shortest length gives $1 \le \tau \le \infty$, and therefore tortuosity is also a time-of-flight factor for fluid transport efficacy. For readers not familiar with the flow modeling term ‘time-of-flight,’ please read Section 2.3 and consult Zuo and Weijermars (2018).

One now realizes that the pressure gradient in the capillaries of Fig. 9b is affected by both the flight path increase and the presence of blocked capillaries. Consequently, the tortuosity is factored in for the case of Fig. 9b, because Eq. (6) needs to use $\nabla P/\tau$ on the left-hand side instead of ∇P, while for Eq. (7) one needs to use $\nabla P/\phi$ on the left-hand side instead of ∇P. This is further examined in Appendix B.

Incorporating the scaling parameters of Eqs. (23) and (24) into Eq. (11) results in a comprehensive expression for porosity-permeability transform (PPT) computations:

$$k = \frac{A}{\alpha}\frac{\beta}{\tau}\phi_{REG} \tag{25}$$

This expression appears to be a novel contribution to the technical literature, which includes the pore-size/shape factor A/α and permeability-reduction factor β/τ. Eq. (25) shares a generic

Table 4
Permeability estimations not corrected for tortuosity and hydraulically effective pore volume.

Pore Shape	Length scale	Permeability	Equation
Circular	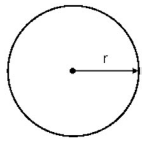	$k = A/\alpha = 0.125 r_p^2$	(8)
Triangular	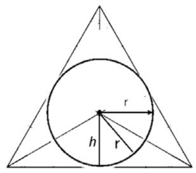	$k = A/\alpha \approx 0.44 h_c^2$	(17)
Elongated Elliptical	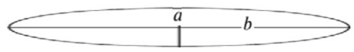	$k = A/\alpha \approx 0.25 a^2$	(22)

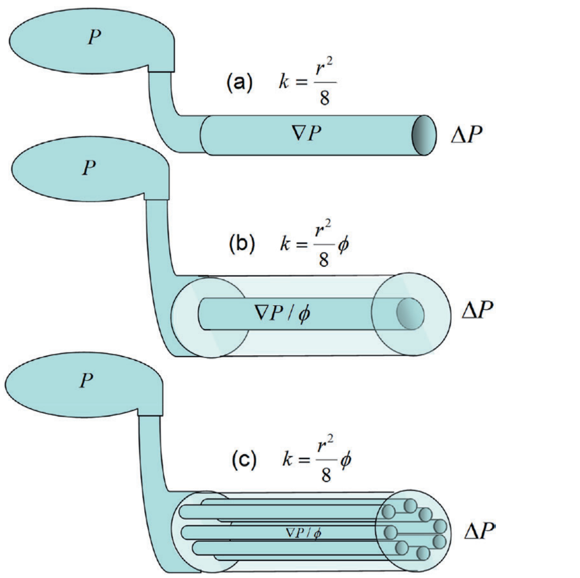

Fig. 8. Idealized core models with circular capillaries. Pore radius r_p is denoted by r for simplicity. The macroscopic pressure gradient ∇P will only correspond to the pressure gradient in the capillary tube if $\phi = 0$, as in (a). More realistically, the pressure gradient in the capillary tube will be $\nabla P/\phi$, as in (b) and (c), and therefore the permeability will be given by $k = \frac{r^2}{8}\phi$.

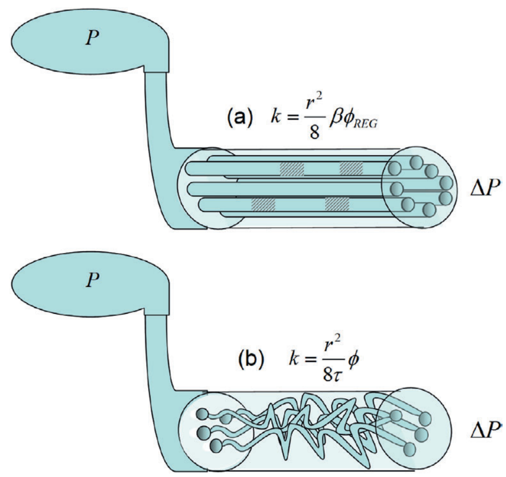

Fig. 9. More realistic core models with circular capillaries, accounting for both blocked capillaries (a) and tortuous capillary tubes (b).

communality with KC-type of equations; there are many different modifications of KC-type of equations (Clennell, 1997). Eq. (25) is believed to be hydraulically rigorous and of practical value, as demonstrated in this study. For use of Eq. (25) in practical applications it becomes now important to explore what constrains the input values of each input parameter (A, α, β, τ and ϕ_{REG}).

3.4. Generic parameter constraints

The remaining objective of the present paper is to explain, using the comprehensive PPT Equation (25), what controls the variety in PPTs observed in natural rocks. Fig. 5 gave a concise overview of how permeability may vary over 13 orders of magnitude, whereas empirically determined porosity in clastic rocks remains confined in a single order of magnitude range $0.01 \le \phi \le 0.4$ (see Section 2.1 and Tables 2 and 3 for explanation). The range $0 \le \phi < 0.01$ can be practically excluded, because such porosity values do not appear in clastic rocks (see Section 3.4.3).

Included in the present analysis are both conventional sandstone and unconventional shale formations, using the reservoir classification typically used in the petroleum industry. Nearly, all data in Fig. 5 was from producing fields, which is why the expenditure was made by the operating companies to drill appraisal wells, collect the cores from numerous wells, and produce high volume of data sets after laboratory analysis (see Appendix A for details on sample size etc.). Each of the two reservoir systems (*i.e.*, conventional sandstones and unconventional shale) will be further analyzed below.

3.4.1. Conventional formations

Addition of further data to the upper half of Fig. 5 populates the central field between the curves of Fontainebleau and Troll/Tarbert sandstones. The added data come from the Hugin, Oseberg, and Flag Sandstone Formations (Fig. 10). Separately, a huge data base of all formations in the Great Artesian Basin (Australia's major aquifer region) provided an additional 14,974 data points (Fig. 11), and the plot also includes some of the transforms of key formations in Fig. 10, to show how the outlines of the leaf-shaped PPT-data fields overlap. Details of the added data sets are also given in Appendix A.

Formations like the Fontainebleau and Troll/Tarbert sandstones cover narrow PPT-trends. The general observation is that the pore-spaces of lower porosity rocks correlate with the more deformed and fine-grained rocks in the formations, which reflects the spatial variation in geological depositional facies and burial history. Fig. 12 gives cross-sections of pore spaces for a mixture of synthetic and real rock samples, showing how the typical pore space varies between curved pentagonal shapes that can be inscribed by circular pore tubes or larger circular pores with internal lobes and cusps (see Mortensen et al., 2005) (Fig. 12a and b). Deformed grains have typical triangular shaped pore conduits (Fig. 12c and d). For the case of Fig. 12a, inner pore circles and outer circles (with lobes and cusps) are inscribed on the pores. Eqs. (8) and (11) gave the permeability depending on capillary tube radius, uncorrected for the further reductions in permeability due to the permeability-reduction factor β/τ. The flow solution through outer circular cross-sections, with cusps and lobes, has been solved by Mortensen et al. (2005), but differs only fractionally from the solution for the inscribed circular-cross-section tubes of Eq. (8). Further analysis in Section 4 will show how one can empirically estimate the permeability-reduction factor.

3.4.2. Unconventional formations

The lowermost half of Fig. 5 represents shale formations, typically made up of rocks with a considerable amount of clay minerals; the PPT is amplified in Fig. 13. It is immediately apparent that the porosity in shales never exceeds 0.15. Also revealing is that the Bakken, which has a relatively high percentage of carbonate minerals, differs from the other, more classical shales (with high clay content) in that it has a higher permeability, which ranks it in the conventional PPT field of Fig. 5, in which is was included. The Bakken may therefore be considered a "conventional" unconventional reservoir, or a "tight" reservoir.

Fig. 14a and b shows micro-structures of platy minerals in shale, packed closely with very little pore space left. The pore conduits appear as approximately elongated elliptical slits, resulting in low porosity due to the clay-dominated mineralogy. Table 3 gave the maximum porosity for randomly packed cubes

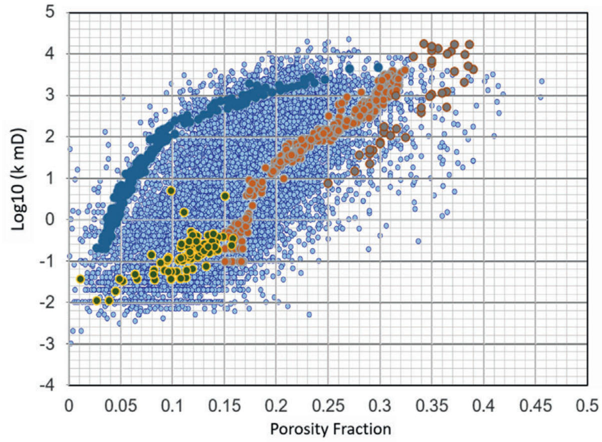

Fig. 11. Porosity-permeability transform (light blue dots) for conventional sandstone formations from the Great Artesian Basin (GAB), the principal aquifer in East Australia, with some key transforms from hydrocarbon basins overlain (Fontainebleau, M65M66, Tarbert, Troll).

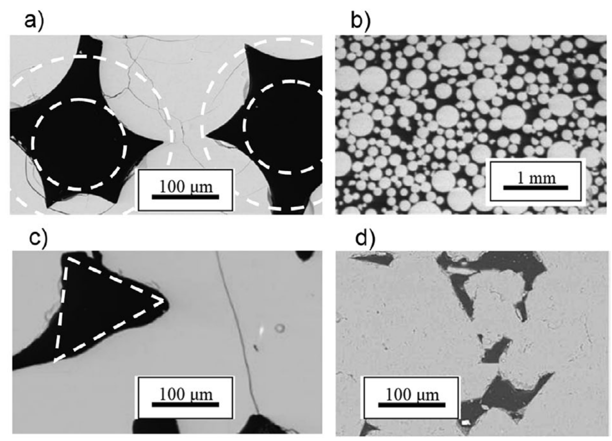

Fig. 12. Thin sections of synthetic pore spaces (black) between spherical grains (grey shades) (a,b) and angular pore spaces (c,d). Sections a-c are synthetic (after Carbillet, 2022), and (d) is from real-world deformed Fontainebleau sandstone (Song and Renner, 2008). Inscribed are approximate flow channel topology of circular tubes (a) and triangular conduit (c), by dashed curves.

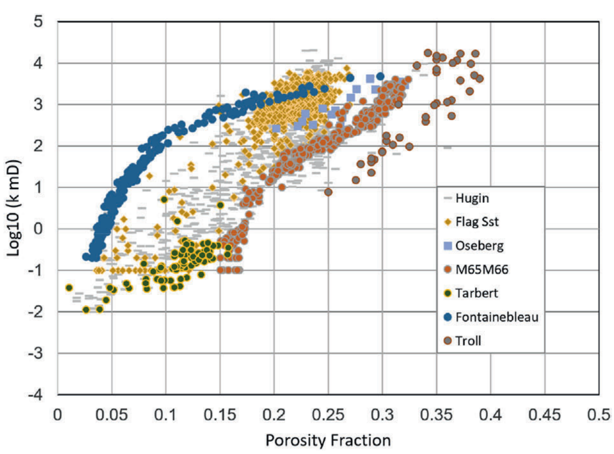

Fig. 10. Porosity-permeability transforms for conventional sandstone reservoirs from different geological epochs and sampled from basins occurring on three different continents (US, Europe and Australia).

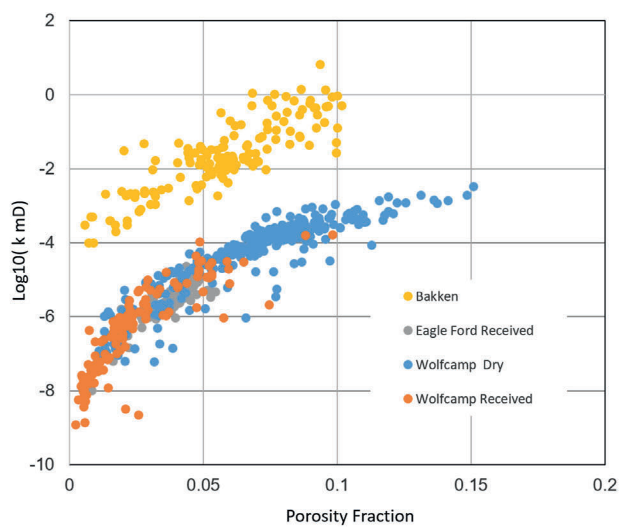

Fig. 13. Porosity-permeability transforms for unconventional shale formations.

to be 22%. However, for flattened platelets that number will be smaller, which is reflected in the empirical 15% upper porosity limit for shale (Fig. 13).

3.4.3. Generic parameter constraints

Regarding the input parameters for the PPT-Equation (25), the following observations are valid.

Porosity: After plotting the data from conventional formations, comprising samples for the combined data sets (Figs. 10 and 11), it appears sandstone formations cover a porosity range which rarely exceeds the theoretical limit of 0.365 for randomly packed regular spheres (Table 2). When that theoretical limit is exceeded, we are dealing with more orderly packed granular aggregates with an upper porosity limit of 0.48 (Table 2). We see from the empirical upper limit of 0.46 (Fig. 11) that the theoretical upper limit of 0.48 is indeed not exceeded in natural sandstone formations. For modeling purposes, the porosity will be assumed to vary between 0 and 0.46, and the type of distribution to be used in the modeling will be based on the actual porosity frequency distribution of real-world sandstone porosity data. For sandstones, it appears the data do not contain porosity values smaller than 0.01 (for example, see distributions for Fontainebleau sand in Figs. C4a, C6a, and C8a), due to which we may truthfully assume ϕ varies over only one order of magnitude.

For unconventional shale formations the maximum observed porosity does not exceed 0.15 (Fig. 13). The empirical number is well below the maximum theoretical porosity of 0.22 for randomly packed rectangular boxes (Table 3), and a rationale was already given (Sections 2.1 and 3.4.2) for why clay minerals cannot reach 0.22 porosity, and even 0.15 occurs in practice as the upper end outlier. For modeling purposes, the porosity of shale may be assumed to vary between 0 and 0.15, and the type of distribution to be used in the modeling will be based on the actual porosity frequency distribution determined using real world shale porosity data. For shales, the lower limit of porosity may also be set at 0.01 in practice (only 2% of the samples have ϕ <0.01 (for example, see porosity distribution for Eagle Ford shale Fig. 22a). Adopting this lower bound limitation significantly simplifies the later Monte-Carlo simulation (see Section 5.1)

Shape parameters: The ratio, A/α, featuring in the PPT Equation (25), will vary according to the shapes of the pore-tubes assumed. Table 4 summarized the key ratios for perfect circular cylindrically shaped pore-throats and triangular pore-throat tubes in sandstones, and elongated, slit-shaped pore-slots in shale. The key inputs are the pore-throat dimensions, for which some empirical constraints are given in Appendix A. Pore-throat diameters generally range from 0.005 to 0.1 μ m in shale, and from about 0.03 to 2 μ m in tight-gas sandstones, and are greater than 2 μ m in conventional reservoir rocks (Nelson, 2009). Screening of thin section and SEM images for pairs of the data sets used (Table A1) and additional data from literature (Fig. A7) revealed 0.01 μ m provided a reliable estimate for the pore-slit half-width, a, in Table 4, which applies to shale. Separately, for sandstone pores, $h = r = 20$ μ m (Table 4), appeared a reliable and nearly universal input for medium and fine-grained sandstones.

Tortuosity: The tortuosity, τ, of Fontainebleau sandstone was suggested to vary between 1 and 25 (Fredrich et al., 1993). The values of τ and β are closely interlinked. In the present study, it was deemed practically impossible to separately estimate these parameters β and τ. However, the pore-throat dimensions used in A/α (Table 4) can be measured on core samples with relative ease (typical values are readily available from literature for many formations). If we have the corresponding empirical data for k, we can solve for the unknown ratio β/τ:

$$\frac{\beta}{\tau}=\frac{k}{(A/\alpha)\phi_{REG}} \tag{26a}$$

In a fundamental analytical approach, Eq. (25) and the rearranged version in Eq. (26a) capture all major parameters that relate ϕ_{REG} to k. The regular porosity can be decomposed into connected and unconnected porosity: $\phi_{REG} = \phi_{EFF} + \phi_{UNC}$ (Bernabe' et al., 2003). In fact, the relationship may be time-dependent, with ϕ_{UNC} increasing over geological time at the expense of ϕ_{EFF}, due plastic compaction of aggregates and elastic-brittle deformation. However, when cores are analyzed, all these processes are assumed to have taken place, and the ratio $\phi_{EFF}/\phi_{REG} = \beta$ has become steady, with $0\leq \beta \leq 1$ in theory but in practice ~$0.8\leq \beta \leq 1$.

When studying cores, CT scans reveal ϕ_{REG} . However, routine core-analyses for oil and gas companies occurs in specialized petrophysical labs (Table A1) that provide pairs of permeability and porosity. For *sandstones* the data output gives (k, ϕ_{EFF})-pairs, because conventional data sets are commonly analyzed with porosimetry that intrudes a nonwetting liquid into the porous structure with increasing pressure and measures the interconnected porosity. For such cases, Eq. (26a) simplifies to:

$$1 / \tau = (\alpha k) / (A\phi_{EFF}) \tag{26b}$$

While Eq. (26b) could be used for sandstone (k, ϕ_{EFF})-data pairs, shale lab data not typically gives ϕ_{EFF}, because traditional Helium-immersion does not work well for intact shale cores. Instead, specialized petrophysical labs (CoreLab, Weatherford, Table A1) use the GRI-method on crushed samples (GRI, 1996; Profice and Lenormand, 2020). The GRI method provides pairs of

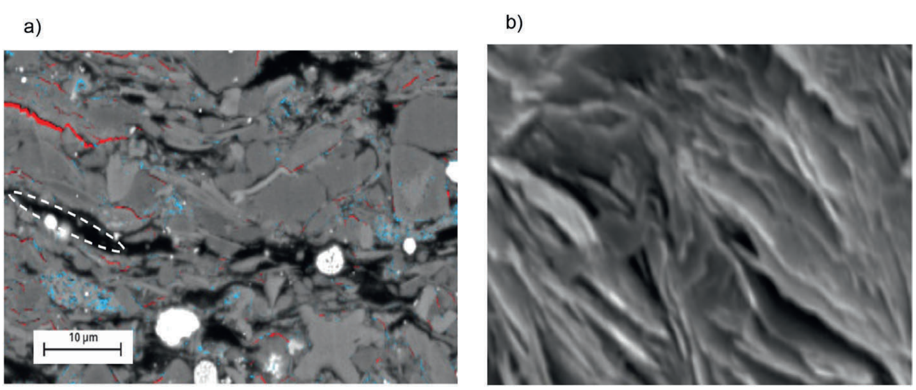

Fig. 14. Thin sections of pore space in shale. (a) Inscribed in the left image is an approximate flow channel topology of pore space by an elliptical slot shape with long elongation (dashed curve). Image from MaP Expert (2015). (b) SEM image of clay minerals in shale (courtesy Hawkwood).

permeability and porosity *for shale* which must be considered closer to (k, ϕ_{REG})-pairs than (k, ϕ_{EFF})-pairs. Consequently, for shale data analysis in this study Eq. (26a) was considered more appropriate. Comparison of GRI porosity and alternative porosity measurements showed ~$0.85 \le \beta \le 1$ (Chen et al., 2019; Jia et al., 2021; Yonghong et al., 2020).

3.5. Critical notion

Altogether, the idea that porosity-permeability transforms provide useful insight on what controls permeability seems useful, but also dangerously wrong-foots the mind in a disturbing and impractical way. After extensive modeling the flow in porous media, and reviewing the relationship between porosity and permeability, the author's conclusion is there is commonly only a poor correlation between porosity and permeability. The hydraulic conduit for flow is only loosely controlled by porosity, but much more so by the size and shape parameters, A/α, and the permeability-reduction factor, β/τ, which accounts for hydraulically connected pores and their tortuousness. While the typical dimension of A is determined by pore size, the pore shape fraction α varies between 0.125 and 0.44. Also, the pore-size distribution in clastic rock systems occupies a very narrow range, characterized by mean values surrounded by nearly triangular distribution with narrow zones of standard deviation (see Figs. A5b and A7a-c). Although the smaller pore sizes for shales bring down their absolute permeability to a certain region, the spread in permeability within the respective sandstone and shale domains is mostly caused by the huge variability in their permeability-reduction factor, β/τ, which accounts for pore-blockage ('arteriosclerosis') and tortuous flow-paths. If there is more compaction by diagenesis and development of mineral growth in the pores, the permeability will be at the lower end of what is characteristic for the type of clastic studied.

This study proposes to largely bypass efforts to measure tortuosity directly and instead focuses on the empirical determination of the permeability-reduction factor β/τ and if ϕ_{EFF} was measured rather than ϕ_{REG}, the simplified permeability-reduction factor $1/\tau$ was used. The solution procedure, using Eq. (26a) to inversely obtain β/τ and Eq. (26b) for $1/\tau$, was subsequently applied to the 13 data sets listed in Table A1 of Appendix A, as detailed in Section 4.

4. Application in case studies

With all required corollary material defined and documented, and the key equations in place, case study applications of porosity–permeability transform-analysis are elaborated in this section. Detailed workflow instructions for data assembly used in the examples are given in Sections 4.1-4.2. The results are given in Section 4.3, distinguishing between sandstone formations (Section 4.3.1) and shale formations (Section 4.3.2). The practical value of the new results is placed in context in Section 4.4.

4.1. Parameter constraints and workflow for conventional formations

Generic constraints for input parameters in the PPT Equation (25) were outlined in Section 3.4. It is apparent from the broad range occupied by PPTs for conventional sandstone formations that the nature of the shape, size and sorting distributions of the sedimentary rock deposits play a major role in the resulting PPT. For example, Fontainebleau sandstone (a pure quartz rock with well-sorted and rounded grains) has a PPT following a narrow trend curve near the upper boundary of the leaf-shaped PPT-field occupied by the representative sandstone formations included in this study (Fig. 10).

The Troll/Tarbert sandstones occur near the lower boundary of the leaf-shaped PPT-field (Fig. 10). Prior studies have shown that dissolving feldspar and precipitation of kaolinite has occurred during early diagenesis in Brent Group sandstones (see details in Appendix A). The kaolinite in turn has been diagenetically converted into illite, and the assorted clay minerals will reduce the permeability by local blockage of pore-pathways (Fig. 15), which may be expected to increase the tortuous length and decreases the effective porosity.

The workflow adopted for constructing synthetic PPTs for sandstones was as follows:

(1) Depositional facies and any subsequent mineralogical changes during diagenesis clearly correlate with the position of the PPT curves in the leaf-shaped PPT-field (Fig. 11). Therefore, permeability transforms require petrophysical study to guide whether reservoir quality will be either near the lower or upper boundary of the PPT-field. The values of β and τ will be adversely impacted when diagenetic clay minerals are blocking fluid pathways.

(2) In the petrophysical laboratory data provided by the oil and gas companies, the porosity of the sandstone cores is routinely measured with fluid-immersion porosimetry, which gives the effective porosity ϕ_{EFF}. The total porosity ϕ_{REG} can be computed from $\phi_{EFF} = \beta\phi_{REG}$, provided β is known. However, β is not always available. It was decided to constrain the ratio β/τ by history matching real data using Eq. (26a) and $1/\tau$ using Eq. (26b), as appropriate.

(3) By far the easiest parameter to ascertain from visual inspection of thin sections and SEM images are the pore dimensions, estimating the values of r, a and/or h_c (as applicable) as outlined in Table 4. The gathered value range is then either matched by probability distributions or one may use a mean value for certain deterministic inputs (as preferred in the present study). For clean sandstones, the circular pore solution can be used (Fig. 12a). For deformed sandstones (like in the Fontainebleau example of Fig. 12c),

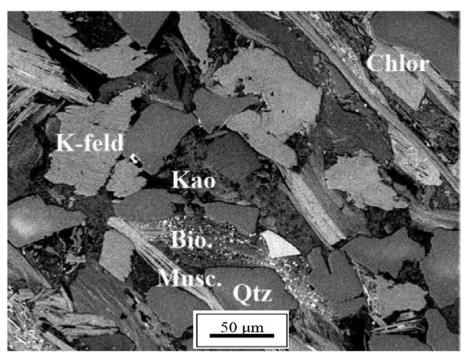

Fig. 15. Thin section of Brent Group sandstone with clay minerals (muscovite, kaolinite and chlorite) reducing transmissibility (Ekre, 2015).

one can use the triangular pore shape solution (Table 4). However, when there is clear evidence of diagenetic clay blocking, such as in some Troll and Tarbert core samples, the pore shape factor for slits may be more appropriate (Table 4). Based on the empirical pore-size distributions found in Figs. A5b for sandstones, and analyses of images, natural pore-size distributions in unaltered sandstones appear to conform closely to triangular probability distributions with very little variance, which is why using a mean pore-size value was deemed reasonable.

Table 5 lists the key model inputs used to reconstruct the porosity-permeability transforms for sandstone systems, using the comprehensive PPT equations derived in Section 3.2.

4.2. Parameter constraints for unconventional formations

The shale formations rich in clay minerals (Eagle Ford, Wolfcamp) were modeled with PPT solutions using the elongated elliptical slot solution as prescribed by the ratio A/α (Table 4). The somewhat diffuse trend seen in Fig. 13 for Wolfcamp and Eagle Ford combined is assumed here to reflect mostly variability in (β/τ)-ratios in combination with variations in pore slit widths. Table 6 lists the key model inputs used to reconstruct the porosity-permeability transforms for shale systems with the comprehensive PPT equation derived in Section 3.3.

4.3. Results

Having presented the key equations, assumptions and model input constraints, all 13 datasets (Table A1) were analyzed using a standardized workflow to generate the following output graphs:

(a) Classical porosity-permeability linear-log cross-plot using the data pairs provided as measured by the data donor company/institution,
(b) Log-log cross-plot of computed permeability factor (beta-tau) versus permeability as measured by the data donor,
(c) Linear-log cross-plot of the same data as in (b),
(d) Linear-linear cross-plot of the computed permeability factor versus the porosity as measured by the data donor.

For brevity, only the results for four out of nine sandstone formations evaluated are given for the conventional formations (Section 4.3.1) and three out of four data sets for the unconventional formations (Section 4.3.2). But the analysis was completed for all 13 data sets and comprehensive summary data is given in this study (Tables 7 and 8).

4.3.1. Conventional sandstone formations

For sandstones, the inverse computation of $1/\tau$ from empirical (ϕ, k)-data pairs used for shape factor $\alpha = 0.44$ and $A/\alpha = 0.44h_c^2$, with for h_c taken half of the typical pore-throat diameter ~20 μm. The standard deviation from the mean for the symmetric triangular distribution in Fig. A5b for Fontainebleau of ~4 μm was concluded to have negligible impact on the computations. Thin sections from core images were available for only a few of the data sets (Hugin, M65-M66); manual measurements revealed pore-throat diameters of the order ~10 μm, which was subsequently assumed to be typical for the sandstone formations analyzed here. Further in-depth analysis of impact of pore-size variability is given in Appendix A2.

(1) Hugin Formation. Fig. 16a is a classical porosity-permeability cross-plot of 687 data pairs for the Hugin Formation, the key reservoir of the Volve Field on the Norwegian Continental Shelf (for details on the Volve Field production analysis, see Weijermars, 2024). The linear regression and associated R^2-value of 0.6904 indicates a moderate correlation exists between the porosity and permeability. Used here is the standard excel trend line output of the squared correlation coefficient, which is also known as the coefficient of determination. R^2 quantifies the degree of correlation. However, when $R^2 \rightarrow 1$, obviously the correlation is excellent: $R = 1$. After computing the simplified permeability-reduction factor, $1/\tau$, using Eq. (26b) for each data pair, Fig. 16b shows a cross-plot of $1/\tau$ against the permeability. The correlation is excellent with $R^2 = 0.9888$, which immediately makes explicit the fundamental role of $1/\tau$ in controlling the permeability of rock formations. Fig. 16c plots the same data of Fig. 16b in linear-log space, which shows the logarithmic curve with the same fit formula as given in Fig. 16b. Comparison of Fig. 16b and c and 16a reveals that $1/\tau$ is an accurate predictor of the permeability, because of the high correlation with the permeability ($R^2 \rightarrow 1$). However, Fig. 16a indicates the correlation between porosity and permeability is weak (R^2~0.7), which makes porosity a relatively poor predictor of permeability. Fig. 16d is a cross-plot of the $1/\tau$ and porosity, which reveals that for very small ($1/\tau$)-values, a broad range of porosities match, which explains why porosity is such a poor predictor of permeability. The correlation between $1/\tau$ and porosity is best matched by a log-linear trend-line with weak correlation, as indicated by $R^2 = 0.57$.

(2) M65-M66 sandstone. Fig. 17a is a classical cross-plot of the porosity-permeability for 335 data pairs from the M65-M66

Table 5
Key model input evaluation comments pertinent to the reconstruction of porosity-permeability transforms for sandstone systems.

Parameter	Value	Comment
ϕ_{EFF}	Can be computed from $\phi_{EFF} = \beta\phi_{REG}$	Left unresolved, because reliable values of β cannot in practice be obtained. Instead, we determined the ratio β/τ as per Eq. (26a) and $1/\tau$ using Eq. (26b), as appropriate.
ϕ_{REG}	0–0.46	Type of input distribution determined by fitting to real porosity distributions. For example, porosity distributions for Fontainebleau and Troll/Tarbert were separately evaluated.
β		Not all pore entries may be hydraulically connected, but for well sorted quartz-sandstones, it is unlikely many blocked arteries occur. However, the value of β is not easy to ascertain, which is why it is preferred to solve instead for the ratio β/τ.
τ	1–25	Based on prior estimations for tortuosity in Fontainebleau sandstone by Fredrich et al. (1993). However, in the present study this value is not separately resolved. Instead β/τ was used.
A/α	Computed from relevant formulas in Table 4.	The respective values of α and A are fixed by formulas given in Section 3.2. The parameters to input are the pore radius, r_p, for cylindrical pore-throats and a, b, c, for the triangular pore throat model.
r_p	Estimated from thin sections	For Fontainebleau sandstone we have prior estimates of 5–10 μ m (Fredrich et al., 1993).
a, b, c, h_c	Estimated from thin sections	Here we enter again μ m dimensions; a simplification made is that we assume for sandstones, $a = b = c$. So, it suffices to estimate a representative dimension for a, and h_c.

Table 6
Key model input evaluation comments pertinent to the reconstruction of porosity-permeability transforms for shale systems.

Parameter	Value	Comment
ϕ_{EFF}	Can be computed from $\phi_{EFF} = \beta\phi_{REG}$	Left unresolved, because reliable values of β cannot in practice be obtained. Instead, we determined the ratio β/τ as per Eq. (26b).
ϕ_{REG}	0–0.15	Type of distribution determined by fitting to real porosity distributions. For example, porosity distributions for Wolfcamp and Eagle Ford shale were separately evaluated.
β		Unlike for sandstones, the platy clay-minerals assemblies of shale are assumed strongly anisotropic. The transforms are for bedding-parallel permeability. However, the value of β is not easy to ascertain, which is why it is preferred to solve instead for the ratio β/τ.
τ		In the present approach, the value of β is not separately resolved; instead β/τ was used.
$A/\ \alpha$	Computed from relevant formulas in Table 4.	The respective values of α and A are fixed by the ellipse solution given in Section 3.2. The parameters to input are the aspect ratios of the elliptical slit dimensions, which is simplified to $2a$ (Table 4).

Table 7
Summary of R^2-values in cross-plots for all formations listed in Table A1.

Set	Reference Name	Nr. of Data	Porosity versus Permeability	Permeability-reduction factor versus Permeability	Permeability-reduction factor versus Porosity
Conventionals					
1	Oseberg	17	0.7276	0.9932	0.642
2	Troll	38	0.7614	0.9994	0.7407
3	Hugin	687	0.6904	0.9888	0.5753
4	Tarbert	79	0.4553	0.8652	0.0741
5	M65M66	335	0.938	0.9995	0.9273
6	Flag Sandstone	1079	0.7712	N/A	N/A
7	Fontainebleau	165	0.9661	0.9977	0.9465
8	Hooray	3672	0.4906	N/A	N/A
9	Great Artesian Basin	14,974	0.4412	N/A	N/A
Unconventionals					
10	Bakken	138	0.6761	0.9658	0.4939
11	Eagle Ford Received	77	0.8241	0.9774	0.6963
12	Wolfcamp Dry	388	0.8532	0.987	0.764
13	Wolfcamp Received	118	0.8011	0.97	0.6468

Table 8
Ranges of the permeability-reduction factor, β/τ, and simplified permeability-reduction factor, $1/\tau$, for all formations listed in Table A1.

Set	Reference Name	Quantity	Minimum Value	Maximum Value
Conventionals				
1	Oseberg	$1/\tau$	7×10^{-3}	9×10^{-2}
2	Troll	$1/\tau$	2×10^{-4}	3×10^{-1}
3	Hugin	$1/\tau$	2×10^{-6}	5×10^{-1}
4	Tarbert	$1/\tau$	2×10^{-6}	3×10^{-4}
5	M65M66	$1/\tau$	3×10^{-6}	1×10^{-1}
6	Flag Sandstone	$1/\tau$	5×10^{-6}	1×10^{-1}
7	Fontainebleau	$1/\tau$	3×10^{-5}	1×10^{-1}
8	Hooray	$1/\tau$	2×10^{-7}	2×10^{-1}
9	Great Artesian Basin	$1/\tau$	2×10^{-7}	2×10^{-1}
Unconventionals				
10	Bakken	β/τ	2×10^{-4}	1×10^{0}
11	Eagle Ford Received	β/τ	5×10^{-5}	2×10^{-2}
12	Wolfcamp Dry	β/τ	8×10^{-5}	10^{0}
13	Wolfcamp Received	β/τ	3×10^{-6}	9×10^{-2}

sandstone, the key reservoir rock of the Horn Mountain Field in the Gulf of Mexico. The best fitting regression curve is a logarithmic solution with associated $R^2 = 0.938$, which indicates an excellent correlation exists between the porosity and permeability. The cross-plot for the permeability-reduction factor versus permeability (Fig. 17b and c) confirms the nearly perfect correlation $R^2 \rightarrow 1$. Because for M65M66 sandstone both the porosity and permeability factor showed excellent correlations with the permeability (with R^2 of 0.938 and 0.9995, respectively), the plot of the permeability factor versus porosity also shows an excellent correlation, with $R^2 = 0.9273$ (Fig. 17d).

(3) Fontainebleau Sandstone. Fig. 18a used 165 data pairs for Fontainebleau sandstone to cross-plot porosity and permeability. Again, an excellent correlation exists with $R^2 = 0.96661$. The cross-plots for $1/\tau$ versus permeability (Fig. 18b and c) give even better regression curve fits ($R^2 = 0.9977$). Predictably, the cross-plot of permeability factor versus porosity shows an excellent fit ($R^2 = 0.9465$) (Fig. 18d).

(4) Great Artesian Basin sandstones. Fig. 19a cross-plots all of the 14,974 data pairs for the key sandstone formations of the Great Artesian Basin (GAB) of eastern Australia (Fig. A6). The linear regression and associated R^2-value of 0.44 (Fig. 19a) indicate only a weak, diffuse correlation exists between the porosity and permeability. In contrast, the cross-plots for $1/\tau$ versus permeability (Fig. 19b and c) reveal surprisingly good correlations. However, neither a regression curve nor correlation coefficient are shown in Fig. 19b and c, because Excel could not fit the trend-line for such a large data set. Fig. 19d confirms the diffuse relationship of porosity and permeability of Fig. 19a carries over to the relationship between $1/\tau$ and porosity. For the full dataset of the GAB, the porosity is a poor predictor of the permeability $R^2 = 0.4412$ (Fig. 19a). However, the simplified permeability-reduction factor, $1/\tau$, with and estimated R^2 of about 0.85 (Fig. 19b and c) is consistently an excellent predictor of permeability.

4.3.2. Unconventional shale formations

In many shale rocks we may observe anisotropic permeability. Below we limit ourselves to estimating the horizontal, layer-parallel permeability. However, the ratio of the vertical and horizontal permeability can be readily modeled by using different (β/τ)-values for flow parallel to bedding and for normal to bedding (see Section 5.2). As a rule, in shale the minimum ratio of k_V/k_H is ~0.1 (Ma et al., 2015; Cao et al., 2024). The permeability used here is the k_H-value, simply denoted by k. For shale, the inverse

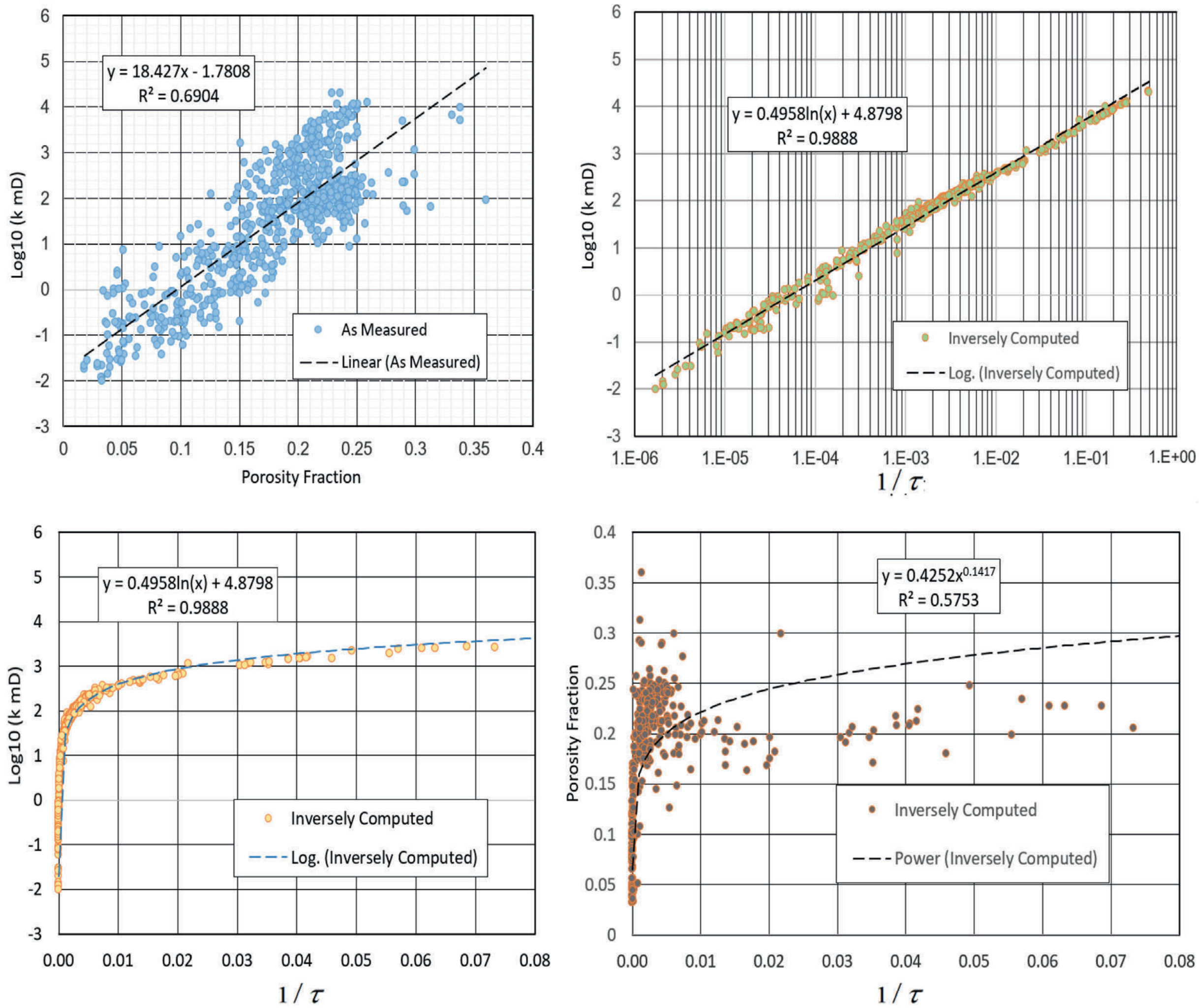

Fig. 16. Transforms for the Hugin Formation (Volve Field, Norwegian Continental Shelf). (a) Linear porosity versus logarithmic permeability. (b) Logarithmic of the simplified permeability-reduction factor $1/\tau$ versus logarithmic permeability. (c) Linear $1/\tau$ versus logarithmic permeability, and (d) Linear $1/\tau$ versus linear porosity.

computation of β/τ from empirical (ϕ, k)-data pairs used for shape factor $\alpha = 0.25$ and $A/\alpha \approx 0.25a^2$, with for a taken half of the typical pore-throat diameter 0.01 μm. The standard deviation from the mean for the symmetric triangular distributions in Figs. A7a,b was ~0.022 μm, which was concluded to have negligible impact on the computations.

(1) Bakken. Fig. 20a cross-plots the porosity-permeability transform using the 38 data pairs for the Bakken Formation, North Dakota (Table A1), which is a major shale play producing oil (for field details, see Weijermars et al., 2017a). The logarithmic regression-curve and associated R^2-value of 0.6761 indicate only a moderate, diffuse correlation exists between the porosity and permeability. However, the cross-plots for the permeability-reduction factor versus permeability (Fig. 20b and c) show excellent correlations ($R^2 = 0.9658$). As expected, the permeability-reduction factor and porosity cross-plot (Fig. 20d) shows only a weak correlation ($R^2 = 0.4939$).

(2) Wolfcamp shale. Fig. 21a cross-plots porosity versus permeability using 388 data pairs from the Wolfcamp shale, a key oil reservoir in the Permian Basin of West Texas (for field details, see Wang and Weijermars, 2019; Tugan and Weijermars, 2022). The best fit regression trend-curve is logarithmic with $R^2 = 0.8532$. However, the permeability-reduction factor versus permeability cross-plot (Fig. 21b and c) shows an even better correlation ($R^2 = 0.987$). Because both the porosity and permeability correlate well with the permeability, the cross-plot of permeability-reduction factor and porosity (Fig. 21d) also reveals considerable correlation exists between the (β/τ)-values and porosity ($R^2 = 0.764$).

(3) Eagle Ford shale. Fig. 22a cross-plots porosity versus permeability using 77 data pairs for the Eagle Ford shale, a key oil reservoir in East Texas (for field details, see Weijermars et al., 2017b). The best fit regression trend-curve is logarithmic with $R^2 = 0.8241$. However, the permeability-reduction factor versus permeability cross-plot (Fig. 22b and c) shows an even better correlation ($R^2 = 0.9774$). Because both the porosity and permeability correlate reasonably well with the permeability, the cross-

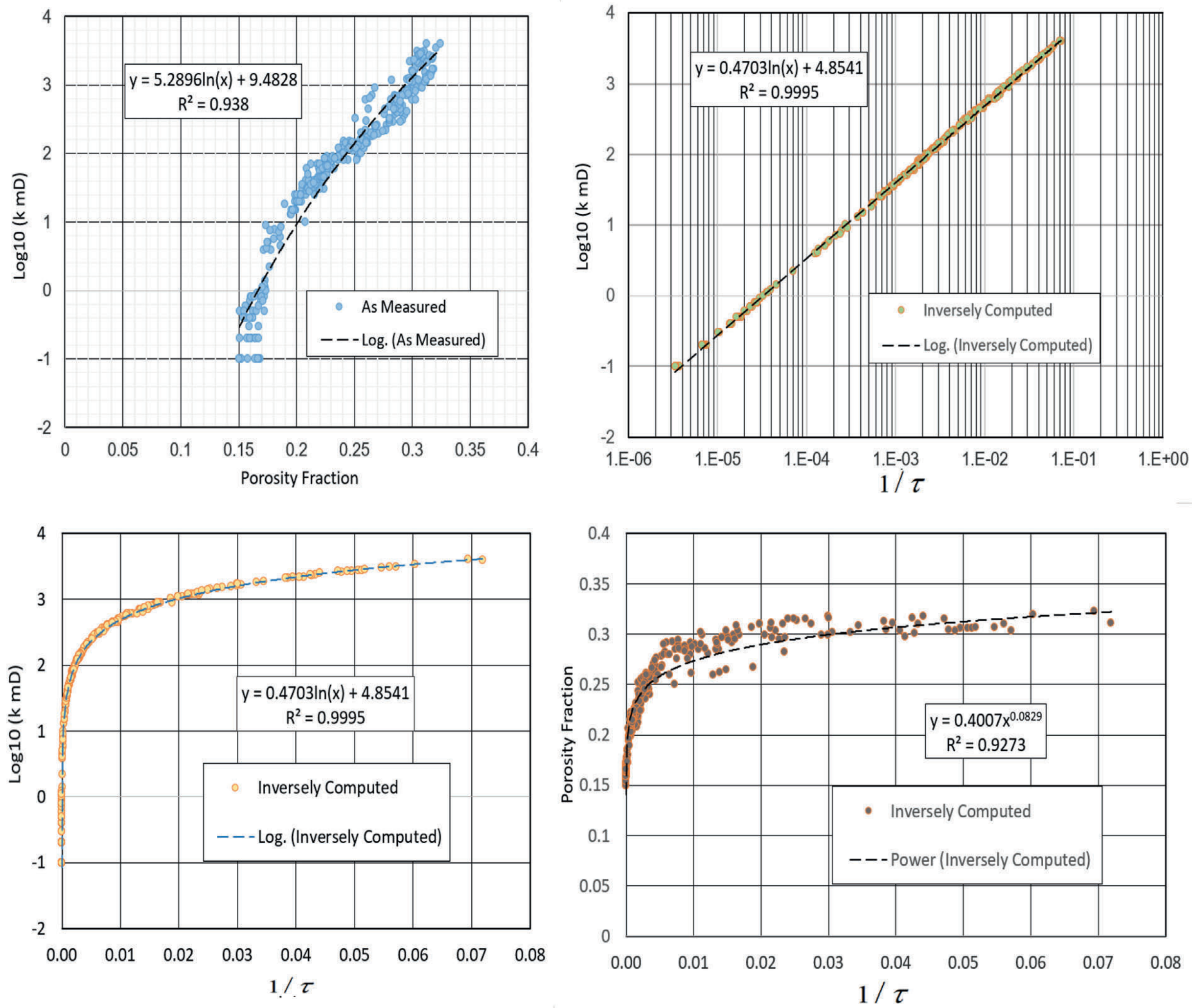

Fig. 17. Transforms for M65-M66 sandstones (Horn Mountain Field, US Gulf of Mexico). (a) Linear porosity versus logarithmic permeability, (b) Logarithmic of the simplified permeability-reduction factor $1/\tau$ versus logarithmic permeability, (c) Linear $1/\tau$ versus logarithmic permeability, and (d) Linear $1/\tau$ versus linear porosity.

plot of permeability-reduction factor and porosity (Fig. 22d) also reveals considerable correlation exists between the (β/τ)-values and porosity ($R^2 = 0.6963$).

4.3.3. Sub-conclusion

The results of the plots of Figs. 16–22 comprehensively show that while porosity correlates sometimes well, but includes correlation factors as low as 0.44 (Table 7), the permeability factor always correlates nearly perfectly with the permeability ($R^2 = 0.86$ and all others >0.97). When the porosity versus permeability has a diffuse correlation, the correlation of the simplified and regular permeability-reduction factors versus porosity may be as low as $R^2 = 0.49$ (last column, Table 7). When the porosity and permeability correlate well ($R^2 \rightarrow 1$), the same holds for the permeability-reduction factors and the porosity.

The cross-plots with the permeability-reduction factors (regular and simplified) versus permeability in Fig. 16b and c to 22b,c show the natural variation occurring in β/τ and $1/\tau$. The log-log scale plots (Fig. 16b–22b) give the best resolution for the smaller range values, which have been abstracted for all of the 13 datasets evaluated and are summarized in Table 8. The values for β/τ and $1/\tau$ generally span between one to six orders of magnitude, with clear clustering of (β/τ) and ($1/\tau$)-values near the lower end of the scale, as is clear from the plots in Fig. 16d–22d. One must remember that the permeability factor, β/τ, is the ratio of the coefficient of hydraulically effective pore space, β, and the tortuosity or time-of-flight factor, τ. While $0 \leq \beta \leq 1$, the tortuosity $\tau \geq 1$, which means $0 \leq (\beta/\tau) \leq 1$. For $1/\tau$, a similar range holds $0 \leq (1/\tau) \leq 1$.

Applying Equation (25) to the 13 selected data sets of porosity-permeability pairs, it appeared that while the pore throat sizes can be represented by very narrow ranges (with average values of 0.01 μm assumed for shale, and 20 μm for sandstones in the present study, see Appendix A; Figs. A5 and A7), the large variation in permeability is actually due to the large range of permeability-reduction factor (β/τ)-values and ($1/\tau$)-values. This finding is supported by analyzing a unique series of 21,767 data pairs of measured porosity–permeability values (Fig. 16b and c to 22b,c). While porosity did not always correlate well with permeability, the permeability correlated extremely well with (β/τ)-values and/or ($1/\tau$)-values.

Table 7 showed the values for β/τ and $1/\tau$ range between 10^{-7} and 1. All probability distributions for β/τ and $1/\tau$ look like the exponential distribution function of Fig. 23b, with strong clustering of β/τ at the lower end of the range, in an exponential

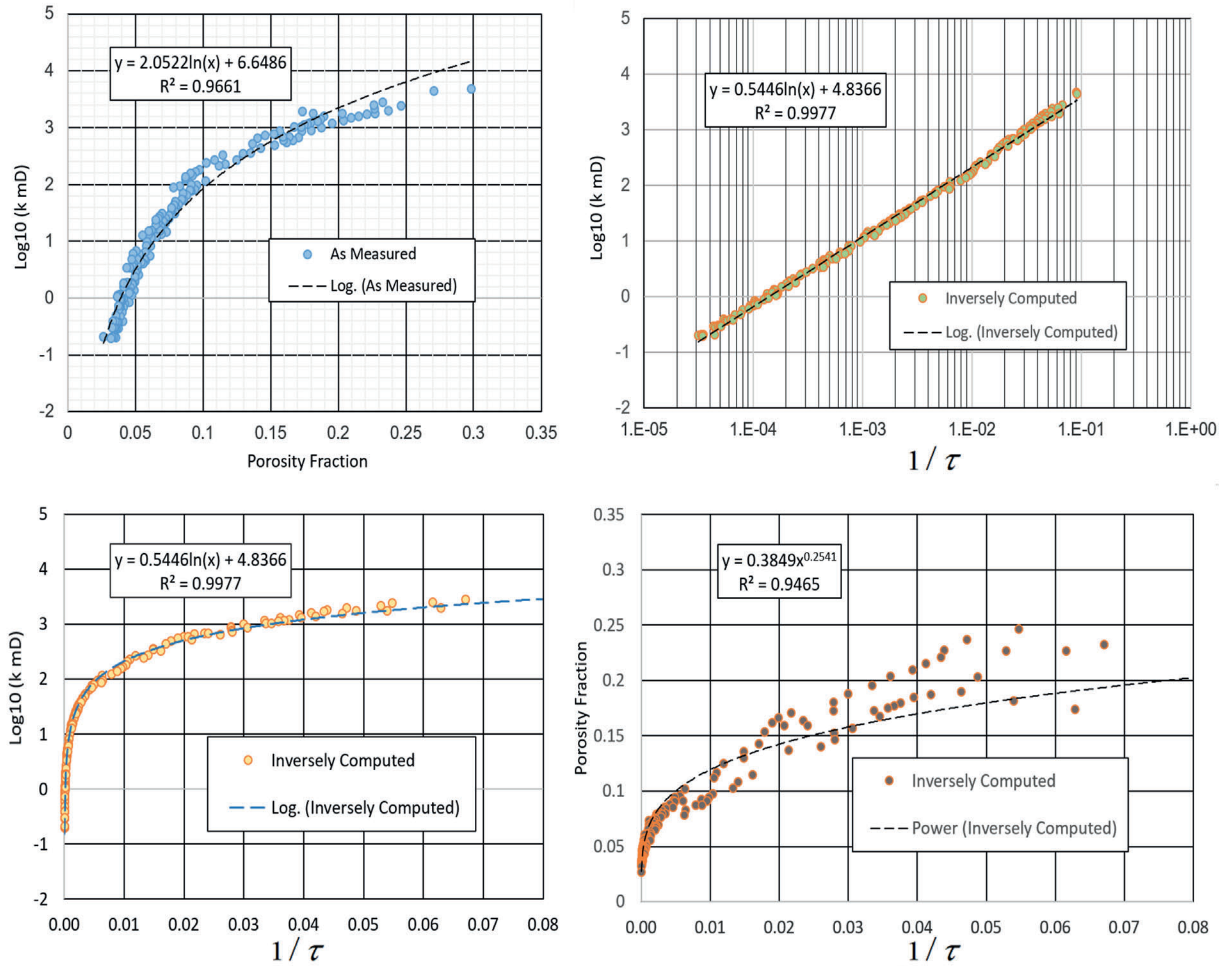

Fig. 18. Transforms for Fontainebleau sandstones (Paris, France). (a) Linear porosity versus logarithmic permeability, (b) Logarithmic of the simplified permeability-reduction factor $1/\tau$ versus logarithmic permeability, (c) Linear $1/\tau$ versus logarithmic permeability, and (d) Linear $1/\tau$ versus linear porosity.

fashion. Physically, the clustering indicates that a surprisingly large number of pore-tubes is poorly connected and with long times-of-flight indicated by tortuosity-values at the lower end of $1/\tau$. The blocking of the pore tubes occurs in sandstones by pyrite and clay mineral growth during diagenesis (Fig. 15) and by deformation closure of pore-tubes after burial (Fig. 12d). In shale, the clay minerals are present as primary minerals and pore-throats are extremely poorly connected shortly after diagenesis and burial as is evident from the analysis in Table 8 and Fig. 14a and b.

4.4. Practical value of synthetic porosity-permeability transforms

The present study proposes a comprehensive method for the practical construction of porosity-permeability transforms. Comprehensive porosity-permeability transforms of 9 sandstone and 4 shale formations (totaling 21,767 data pairs from three different continents) were used to benchmark the hydraulic relationships against real-world data. The sandstones and shale possess a variety of basic pore shapes, partially blocked pore tubes and lengthened flow paths as scaled by β/τ. While $0 \le \beta \le 1$, the tortuosity $\tau \ge 1$, which means $0 \le \beta/\tau \le 1$. When the time-of-flight of fluid transfer across the porous medium is large, the permeability-reduction factor will be small.

The method considers the following criteria: (1) hydraulic characterization based on stream tube topology (*i.e.*, Table 3), (2) geological facies based on depositional environment (sandstone or shale), and (3) diagenetic changes during burial of the rock (pyrite growth, clay mineral growth, and pore coalescence due to deformation). The advantage of the proposed approach is that the equations and workflow are easy to use, with results being satisfactory accurate, as demonstrated by close matches between empirical (using a range of real-world data sets) and theoretically modeled porosity-permeability transforms, comprising both sandstones and shale.

The value of the new insight is substantial in at least two major ways:

(1) The general permeability-reduction factor, β/τ, and simplified permeability-reduction factor, $1/\tau$, can quantitatively scale and conceptually explain, after establishing from a limited number of measured porosity-permeability data pairs the inversely solved (β/τ)-curves and $(1/\tau)$-curves, the huge variety of permeability occurring in natural rock formations (Section 4.3).
(2) Once a (β/τ)-curve or $(1/\tau)$-curve, has been established for a particular rock formation (Sections 4.3.1 and 4.3.2), unlimited number of porosity-permeability pairs can be generated using the forward expression of Eq. (25). Separately, A/α is a conveniently chosen deterministic input, based on mean pore size (see Table 4). Using a shale formation example, the

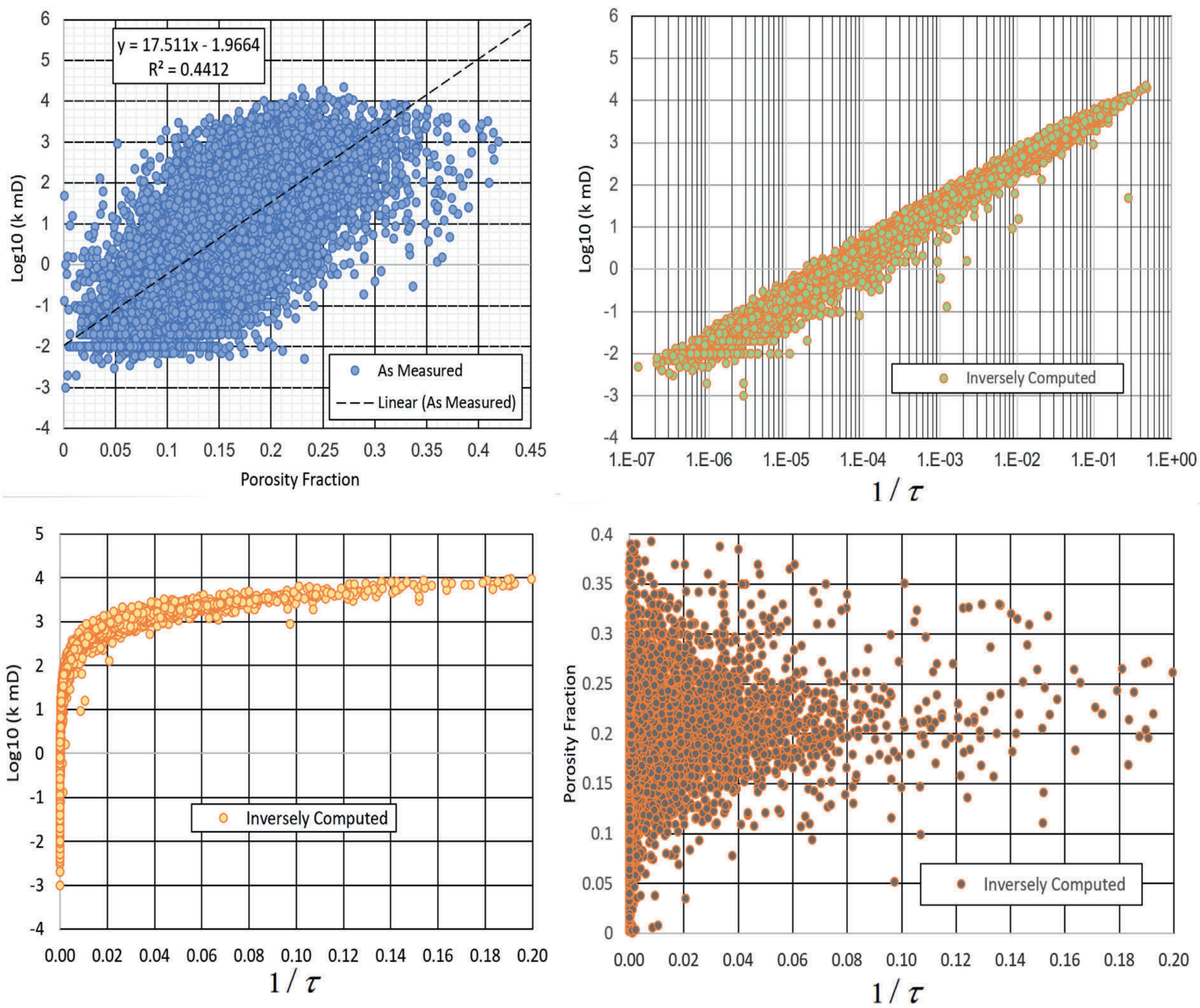

Fig. 19. Transforms for the Great Artesian Basin sandstones (Australia). (a) Linear porosity versus logarithmic permeability, (b) Logarithmic of the simplified permeability-reduction factor $1/\tau$ versus logarithmic permeability, (c) Linear $1/\tau$ versus logarithmic permeability, and (d) Linear $1/\tau$ versus linear porosity.

correlated probability distribution functions of ϕ_{REG} (Fig. 23a) and β/τ (Fig. 23b), can be used to regenerate the porosity-permeability transforms, populated by an unlimited (but finite) number of data points, corresponding to the number of iterations used in the Monte-Carlo simulation.

The process to generate comprehensively populated porosity-permeability transforms from only a limited number of measured data pairs is straightforward. The porosity and permeability are correlated in all cases, which requires establishment of their correlation from the real-world equivalent, before constructing the synthetic porosity-permeability transform. Next, the synthetic porosity-permeability transform can be computed probabilistically by Monte-Carlo simulation, using the probabilistic distribution curves for porosity and the permeability-reduction factor as inputs to produce probabilistic outputs for the permeability.

Fig. 24a shows how 250 new data pairs were synthetically generated for Eagle Ford shale, which 'trained' (to use a machine learning term) on the 77 data points actually measured (Fig. 24b). If we superimpose the two populations of the synthetic and measured values (Fig. 24c), close matches appear, with very satisfactory correlation factors for both the synthetic transform with (250 data points; $R^2 = 0.7745$) and for the measured transform (with 77 data pairs; $R^2 = 0.8241$).

The two distributions for porosity ϕ_{REG} (Fig. 23a) and β/τ (Fig. 23b) were used to generate the data pairs of Fig. 24a. Monte Carlo simulation can regenerate any desired population size of transform data pairs, but was here capped at 250 iterations (resulting in 250 pairs) to not overcrowd the plots of Fig. 24a and c. The Monte Carlo simulation was performed using the @Risk plug-in for Excel and the syntax for the two correlated distributions is given in Table 9. Further explanation of how forward porosity-permeability transforms can be generated from existing datasets is given in Appendix C. Considering the relative speed and ease at which the synthetic porosity-permeability transforms can be generated, and given the considerable time and cost of laboratory measurements required to correlate the data for porosity-permeability transforms, it is now obvious the method proposed here represents considerable practical and commercial value.

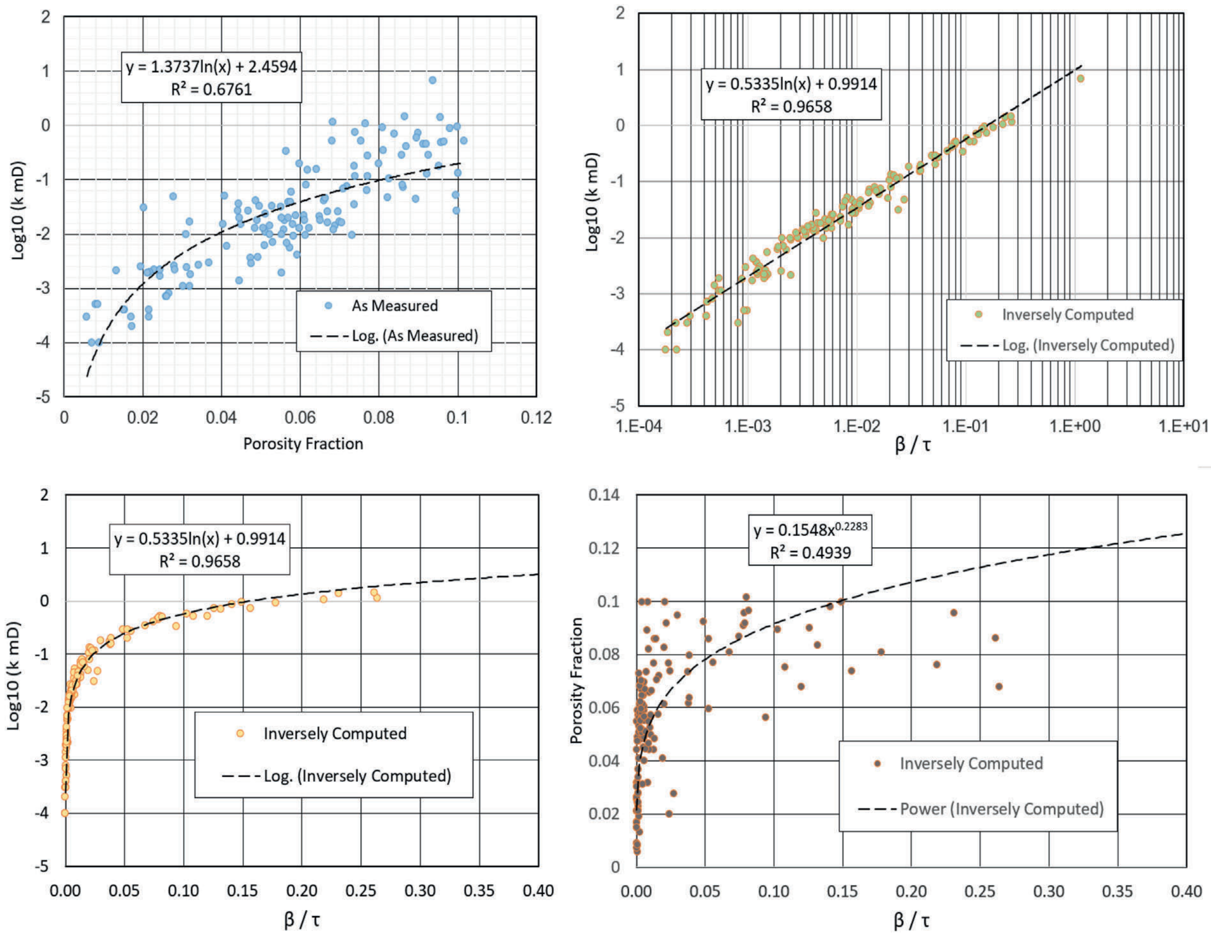

Fig. 20. Transforms for Bakken Shale Formation (North Dakota). (a) Linear porosity versus logarithmic permeability, (b) Logarithmic permeability-reduction factor versus logarithmic permeability, (c) Lnear permeability-reduction factor versus logarithmic permeability, and (d) linear permeability-reduction factor versus linear porosity.

5. Discussion

This section highlights the innovative nature of the proposed solution and methodology (Section 5.1). Next, the findings are translated into a conceptual model highlighted in Section 5.2. The practical value for probabilistic reserves and storage capacity estimations is outlined in Section 5.3. New directions for future research are briefly mentioned in Section 5.4.

5.1. Innovation

The present generic solution for estimating the permeability uses topological parameters, A and α, of pore-tube flow space geometry, and scalars for representing effective pore volume, β, and the tortuosity or time-of-flight factor, τ. The present study clearly drew from prior studies what was relevant for a modern and improved approach, and combines the power of the generic solutions of Eqs. (25) and (26) with modern Monte-Carlo simulation techniques to produce accurate porosity-permeability transforms, as was demonstrated in the case studies given in Section 4. Additionally, the advent of computing power and Monte-Carlo simulation postdates the early pioneers. Aspects of pre-existing solutions by Kozeny (1927) and Carman (1937, 1956) were used. However, the prior solutions did not expand in the direction of the general solution given here. For example, consider one commonly used solution based on Kozeny-Carman theory (Costa, 2006):

$$k = c_f \frac{r^2 \phi}{8\tau} \tag{27}$$

One can immediately see that the empirical scaling parameter, c_f, featuring in Eq. (27) modifies the Poiseuille solution for a circular cylindrical tube. Eq. (25) in the present study starts from a general solution of Eq. (11) and then derives specific solutions as per Table 4. One reviewer claimed Eq. (27) would be sufficient and no need for Eq. (25) existed. It is true using $c_f = 1$ gives a correct solution for circular capillaries. However, for other pore tube shapes like elliptical, triangular, rectangular or other topologies, multiplying $\frac{r^2\phi}{8\tau}$ with a dimensionless 'fixing parameter' c_f is only in part related to the pore shape, because the factor 8 came from the assumption of a circular pore shape, which in Eq. (27) is kept as an unchangeable, fixed parameter. Therefore, Eq. (27) and (25) have similarities, but also some fundamental differences are upheld. Although some resemblances exist with prior work, the present study uses a scaling approach with permeability-reduction factor, β/τ, and the size and shape parameters, A/α.

Furthermore, this study is distinctive from prior work by reducing the focus on porosity as a predictor of permeability. One should break away from the classical contention that porosity is a strong indicator of permeability; although some correlation exists, the direct correlation quality generally is very poor. For example, if we take an arbitrary sample of GAB clastics (Fig. 19a),

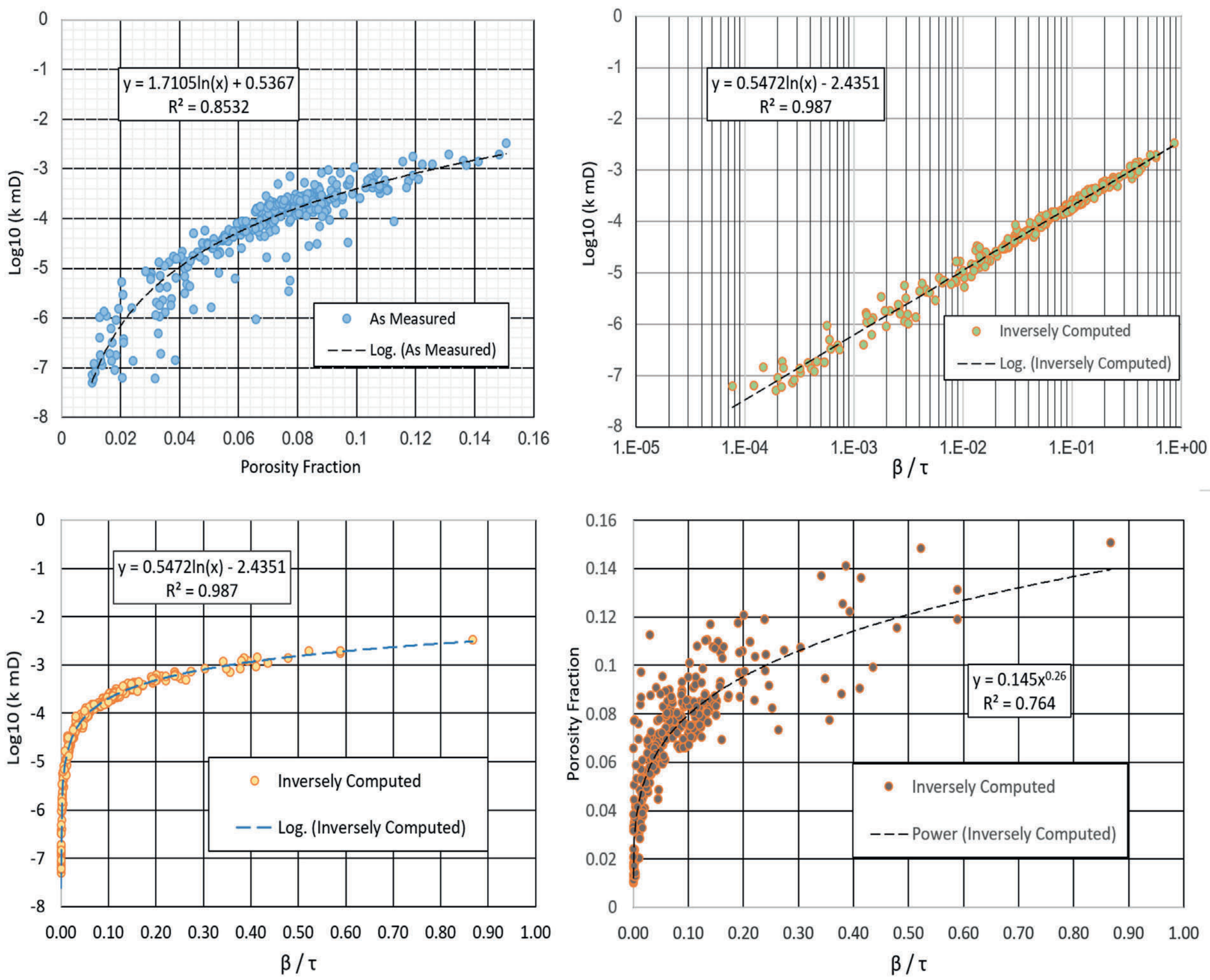

Fig. 21. Transforms for Wolfcamp Shale Formation (Permian Basin, West Texas). (a) Linear porosity versus logarithmic permeability, (b) Logarithmic permeability-reduction factor versus logarithmic permeability, (c) Linear permeability-reduction factor versus logarithmic permeability, and (d) Linear permeability-reduction factor versus linear porosity.

for any porosity value, one finds the permeability varies between 10^{-3} and 10^4 mDarcy – a variation over 7 orders of magnitude. Now consider simple physics of flow in porous media: if we decrease the porosity from 0.38 to 0.038 in a sandstone sample, the storage is reduced by one order of magnitude and the flow rate would increase 10-fold. However, the area occupied by circular pores reduces at a rate given by the square radius and therefore permeability reduces 100-fold. The overall effect of the 10-fold reduction in porosity therefore would be a 100-fold net decrease in permeability, and no more, whereas we observed a 7-order of magnitude range for tortuosity. Therefore, if one inspects Fig. 19c and d, very good correlations can be inferred between the permeability and the simplified permeability-reduction factor $1/\tau$. The strong correlation between the permeability and the permeability-reduction factors (regular β/τ and simplified $1/\tau$) is evidence of physical soundness that the parameters in the permeability-reduction factors are the dominant ones responsible for the observed variability in permeability. Pores may be blocked (as accounted for by β) and travel-paths may become very tortuous (as accounted for by τ), to the extent that β/τ varies over 6–7 orders of magnitude with much of the variation taking place at the lower end of the (β/τ)-scale ($0< \beta/\tau <0.02$). So while β/τ and k correlate well (Fig. 19b and c), neither ϕ and k (Fig. 19a), nor ϕ and β/τ (Fig. 19d) correlate well. This confirms that ϕ is a poor measure of permeability.

The pore-size distribution of Fontainebleau sandstone varies in a triangular distribution between a minimum of 10 μm and maximum value of 30 μm, with a mean value of 20 μm (Fig. A5b). The pore shape factor α has been physically constrained to vary for circular and triangular pores between 0.44 and 0.25 (Table 4). Consequently, neither A nor α can explain why permeability would vary over 5 orders of magnitude (Fontainebleau) or 7 orders of magnitude (GAB sandstones). Counter to what is seen for GAB clastics, Fontainebleau sandstones give a very good correlation for ϕ and k (Fig. 18a). This good correlation is only apparent, because there is a reasonably good correlation between ϕ and $1/\tau$ (Fig. 18d), due to which porosity can act as a proxy for $1/\tau$ and correlates well with permeability. Uncompacted Fontainebleau pores are rarely blocked, because it is such a well-sorted pure quartz sand. However, in the lower porosity Fontainebleau sandstone, which is from regions with more compaction, there is pressure-solution fusion between grains, due to which pore tubes may become blocked with increasing compaction. As a result, flow-paths become tortuous and Fontainebleau sandstone has a permeability varying over five orders of magnitude. This again can be ascribed to ($1/\tau$)-reductions, not to pore size variability. Neither A nor α can explain why permeability would vary over 5 orders of magnitude (Fontainebleau) or 7 orders of magnitude (GAB sandstones).

History-matching to theoretical models is standard practice in petroleum engineering, and the inferred values of β/τ (shale) and

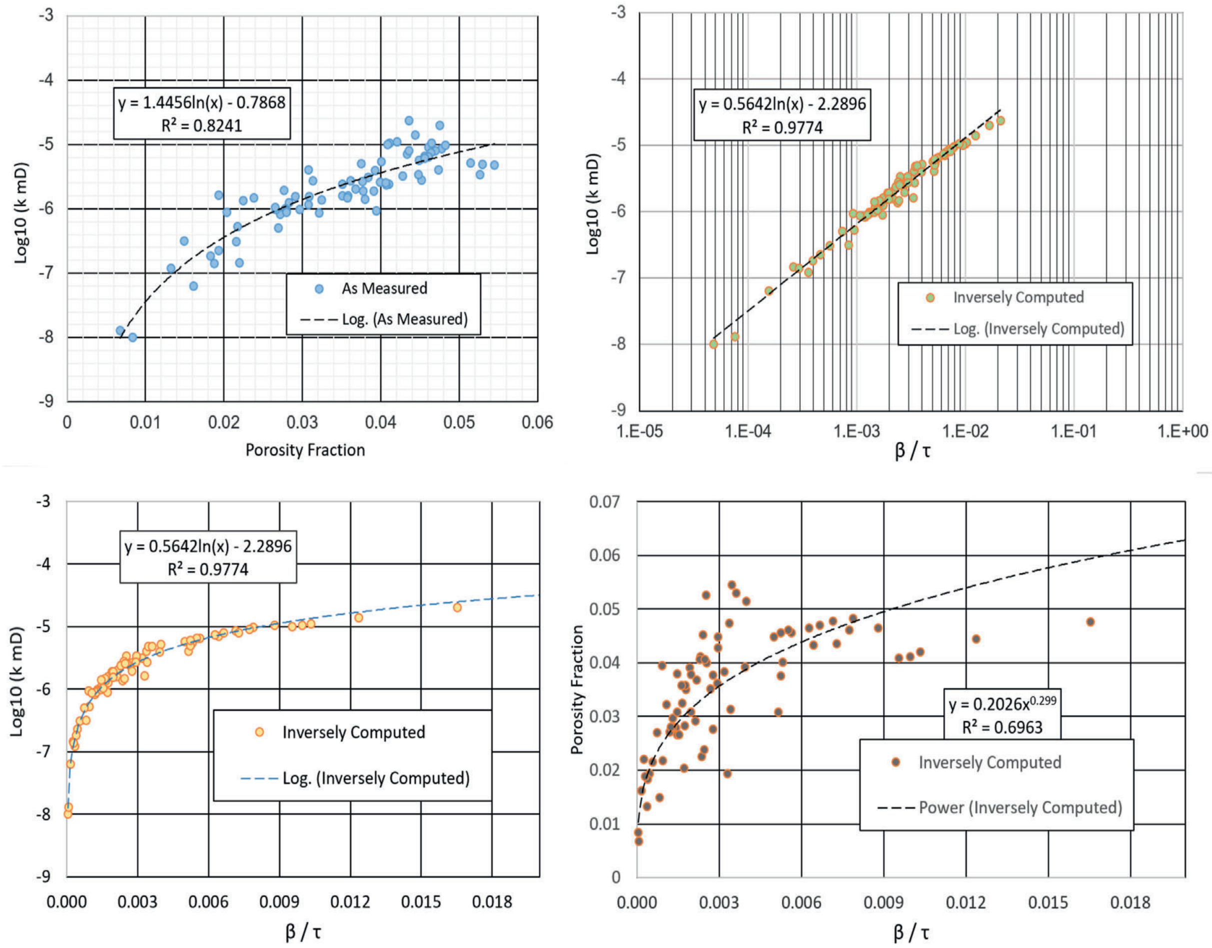

Fig. 22. Transforms for Eagle Ford Shale Formation (East Texas). (a) Linear porosity versus logarithmic permeability, (b) Logarithmic permeability-reduction factor versus logarithmic permeability, (c) Linear permeability-reduction factor versus logarithmic permeability, and (d) Linear permeability-reduction factor versus linear porosity.

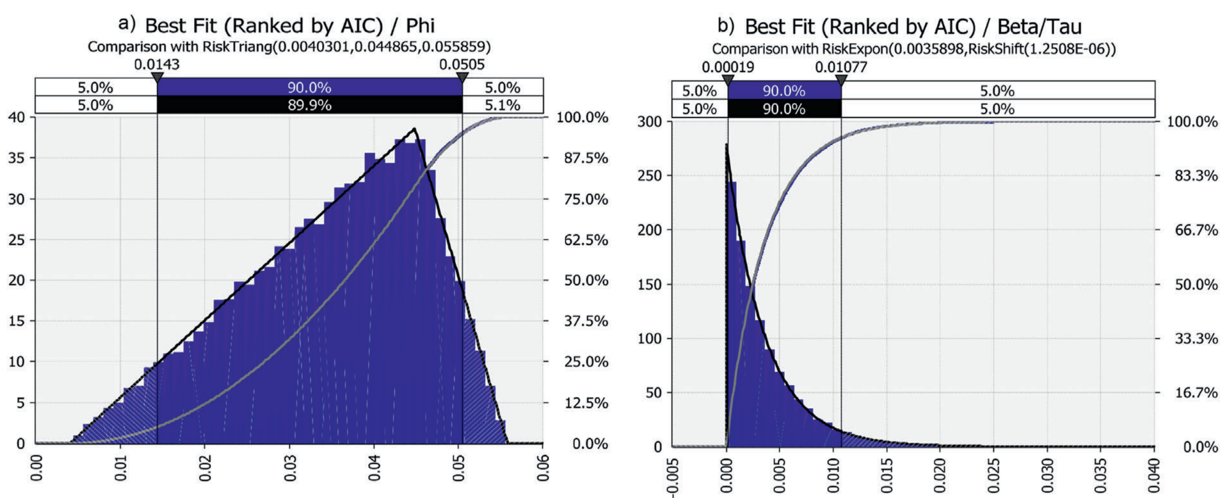

Fig. 23. Eagle Ford shale. Probability density distribution functions (PDFs) for (a) regular porosity ϕ_{REG} and (b) permeability-reduction factor (β/τ). Left scale gives frequency for the PDF-values, and right scale is for the cumulative distribution.

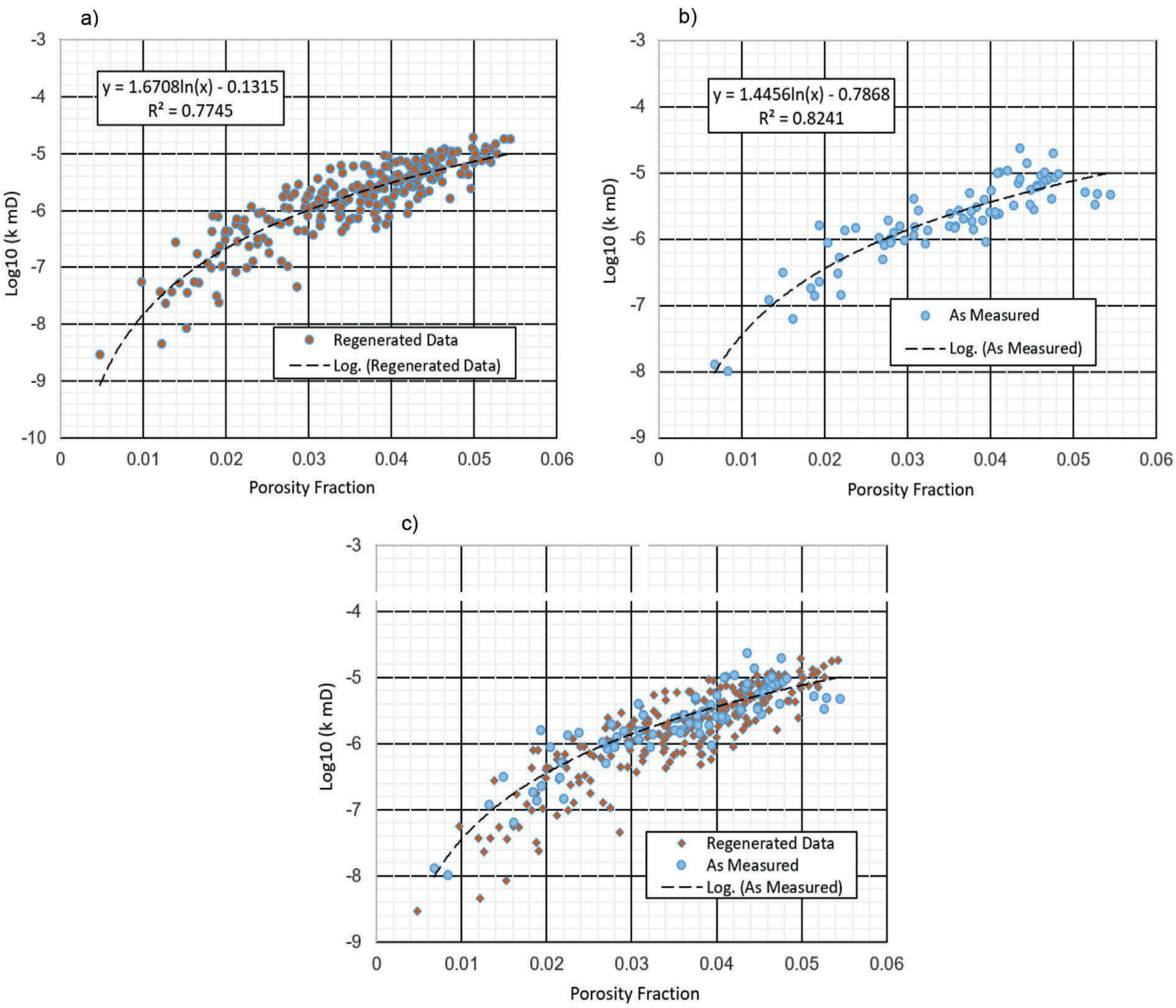

Fig. 24. Transforms for Eagle Ford Shale Formation (East Texas). (a) Synthetic copies of 250 porosity-permeability data-pairs re-generated, (b) Original 77 data-pairs measured by operator, and (c) superposed results of (a) and (b).

Table 9
Correlated distribution functions used for generating the synthetic porosity-permeability transforms of Fig. 24a.

Parameters	Type	Distribution	Unit
ϕ_{REG}	Probabilistic	RiskTriang (0.0040301,0.044865,0.055859,RiskCorrmat (CorrelationMatrix1,1))	–
β/τ	Probabilistic	RiskExpon (0.0035898,RiskShift (0.0000012508),RiskCorrmat (CorrelationMatrix1,2))	–
A/α	Deterministic	$0.44*(0.01)^2$	μ m^2
Correlation	R^2	0.797	–

$1/\tau$ (sandstone) give excellent matching data. For shale, the pore-size distributions cluster around 0.01 μm with little standard deviation (Figs. A7a-c). The recommended α-value for shale is 0.125 (Table 4). Consequently, the limited variation in A and α cannot explain the observed permeability range between 10^{-9} and 10^{-2} mDarcy (Fig. 5). Consequently, the (β/τ)-values must explain the observed permeability range. The present author takes this as confirmation that the permeability-reduction factors (regular and simplified) are pre-eminent predictors of permeability.

Finally, a comparison between the permeability-reduction factor β/τ introduced in the present study, and other, prior attempts to name KC-type scaling parameters are briefly reviewed here. The use of a reservoir quality index (RQI) given by k/ϕ, was proposed by Amaefule et al. (1993). More recently, Kassab et al. (2022) showed a high degree of correlation between log (RQI) and log(k) for their samples of the Arab A formation (with $R^2 > 0.989$) and a power-law exponent close to 0.5, which was in agreement with the KC-equation used by the authors: RQI ~ r_p ~ $k^{0.5}$. On the other hand, a poor correlation was observed between log (RQI) and porosity ($R^2 = 0.33$, see their Figs. 6 and 5). The ratio $k/\varnothing$ is different from β/τ used in the present study.

Separately, the definition of an effective hydraulic radius, $r_{eff}^2 = 8k\tau^2/\phi$ (e.g., Pape et al., 1999), was based on a certain type of KC-equation, and the authors put much emphasis on the proportionality between $r_{eff}^2 \sim k$, with the further contention that therefore k/ϕ is a suitable proxy for evaluation of the effective hydraulic radius: $A \sim r_{eff}^2 \sim (k/\phi)$. There is a certain truth in that

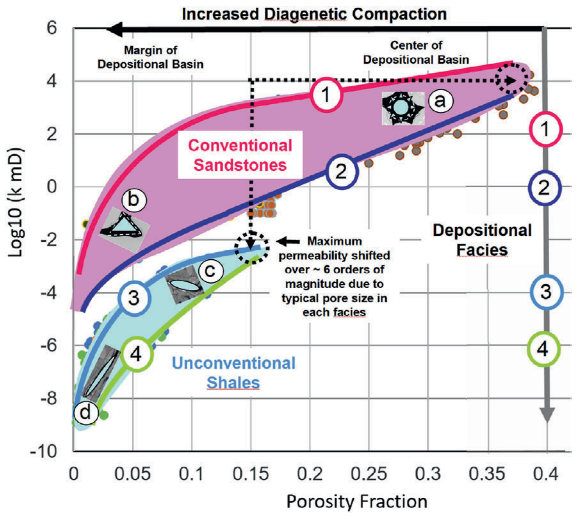

Fig. 25. Permeability transforms for conventional sandstone and unconventional shale reservoirs can be characterized as resulting from the interplay of depositional facies and diagenetic compaction and accompanying mineral alterations. Generalization based on data in Fig. 5 and further analyses.

contention, as the shift in overall permeability between sandstone and shale is due to their respective $A \sim r_{eff}^2$, as pointed out above, and further illustrated in Fig. 25 (see Section 5.4).

The shift between the permeability fields of sandstones as compared to that of shale seen in Fig. 5 is here ascribed to a typical sandstone pore diameter of 10–20 μm and shale pore diameter of 0.01 μm; the squared values imply a permeability shift over 6 orders of magnitude. The nature of this shift is further elaborated in the conceptual model outlined in Section 5.2.

5.2. Conceptual model improvement

The transform analysis presented here, generated significantly improved conceptual insight regarding the root causes of the large permeability variation found in clastic rocks. This insight is succinctly graphed in Fig. 25. Two major geological processes determine the permeability of the clastic rocks: (1) Depositional facies, and (2) Degree of diagenetic compaction.

The principal depositional facies are marked in Fig. 25, with the upper and lower boundaries for the sandstones given by Facies Types 1 and 2; those for shale are marked as Facies Types 3 and 4. Table 10 summarizes the characteristics of these facies-types. The conventional sandstones have permeability varying between 10^4 and 10^{-4} mDarcy. The maximum porosity correlates with permeability of about 10^4 mDarcy, while the minimum porosity correlates with permeability of about 10^{-4} mDarcy. The shales have permeability varying between 10^{-2} and 10^{-9} mDarcy. The maximum porosity correlates with permeability of about 10^{-2} mDarcy, while the minimum porosity correlates with permeability of about 10^{-9} mDarcy,

In the sandstone facies, any diagenetic compaction will reduce the porosity and also tends to deform the dominant pore shape from circular (marked “a” in Fig. 25) to triangular (marked “b” in Fig. 25). In the shale facies, the diagenesis will flatten the elliptical pores (marked “c” in Fig. 25) to long elongated slots (marked “d” in Fig. 25), with the solutions of Table 4. The diagenetic process is here assumed to be slowest in the center of sedimentary basins, where relatively rapid subsidence will lead to sediment burial with less time for pore water to escape. The formation likely will stay over-pressured in these regions. Therefore, central basin rocks are less impacted by diagenetic mineral alteration and less mineral growth occurs in the pore space as compared to that seen in the same formation in the margins of the basin. The slower burial in the margins leads to a higher degree of water expulsion and the decreased pore pressure facilitates higher diagenetic compaction. There is also more mineral growth in the pore space of the distal basin regions due to enhanced hydrothermal fluid circulation. The central basin regions commonly combine high hydrocarbon maturity with less compaction and less mineral alteration, and therefore possess better reservoir quality.

The shift between the permeability ranges occupied by the two types of clastics (i.e. 10^4 -10^{-4} mDarcy for sandstone, and 10^{-2} - 10^{-9} mDarcy for shale) is ascribed to the typical sandstone pore diameter being 10–20 μm, while the typical shale pore diameter is 0.01 μm; the squared values of the pore size imply a permeability shift over 6 orders of magnitude. This shift is marked in Fig. 25.

Although pore-size plots of individual samples suggest very little standard deviation occurs (Fig. A5b, A7a-c) about the mean pore-size values, different cores from the same formation in other locations may reveal other typical pore sizes. This problem of spatial variation in petrophysical properties remains unresolved in the present study. Some trade-off between A/α and β/τ is possible: if A/α decreases, β/τ increases, given a certain pair of measured permeability and total porosity. The fractal nature of pore size distributions suggests variations in A/α may be captured in fractal permeability models (Pape et al., 1999; Schmitt-Rahner et al., 2018; Xiao et al., 2021; Zhang et al., 2017; Zhang and Weller, 2014). However, such details are beyond the scope of the present study.

5.3. Practical value

5.3.1. Permeability transform optimization

The proposed method is particularly powerful when the permeability measurements are at the lower resolution limit of laboratory methods, as is the case for shale (Goral et al., 2020; Zhang et al., 2020). Estimating the permeability of shale is important to optimize the production forecasts and actual production of hydrocarbons from shale formations, now accounting for at least 8.3% of global oil and 18.9% of global natural gas production (IEA, 2022). Being able to improve laboratory-measured porosity-permeability transforms with synthetically produced transforms of unlimited data pairs (see Fig. 24a and details in Section 4.4) has great practical significance and represents considerable commercial value, because of the number of core samples to be analyzed in the laboratory can be reduced.

Table 10
Principal sedimentary facies distinguished in Fig. 25.

Type	Characteristics
1	Mature, clean quartz sand deposits fed by long river system eroding sediment sources in cratonic igneous and metamorphic rocks; due to long supply route and high flow rates only clean, well-rounded and well-sorted quartz grains survive the long transportation to the depositional basin.
2	Less mature, clastic deposits fed by river systems comprising quartz, feldspar and micas from igneous rocks in hinterland such as cratonic shield areas, with relatively short supply route such that feldspar and micas survive transportation to the depositional basin.
3	Low energy deposits on flood plains and coastal lagoons acting as clay settlement zones.
4	Slowest flow rates of sediment supply due to which only shale with the largest proportion of clay minerals may form.

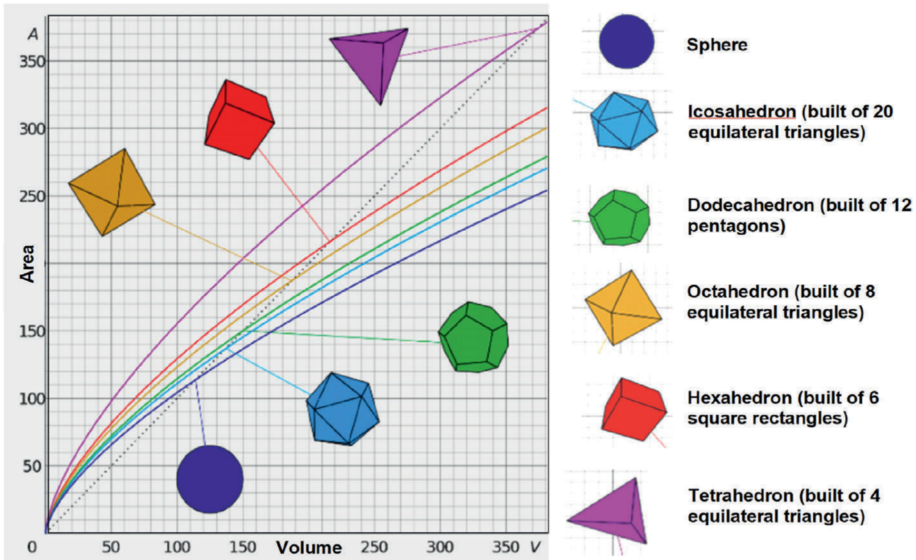

Fig. 26. Curves showing that the ratio of *non-dimensional* surface area (vertical scale) to *non-dimensional* volume (horizontal scale) is smallest for pore spaces closer to spherical shapes and largest for pyramidal pore shapes. For any particular finite volume of fluid, the surface contact area with the pore wall varies with pore shape and in a non-linear fashion when pore volume increases (adapted from Weijermars and Khanal, 2019a).

5.3.2. Reserves estimation

Analytical solutions exist to predict the performance of wells in both conventional and unconventional formations, while accounting for well completion design parameters such as the hydraulic fracture spacing and fracture half-length (Alvayed et al., 2023). The largest uncertainty in the input parameters for well productivity forecasting and reserves estimation resides in the permeability, which also factors into the hydraulic diffusivity used in well-rate forecast based on Gaussian pressure-transient solutions (Weijermars, 2022). The probabilistic permeability curves and correlation with porosity can provide more reliable estimations for probabilistic reserves classification, after data acquisition and hydrocarbon discovery in appraisal wells, but prior to drilling costly production wells. Likewise, analytical solutions exist for carbon sequestration in conventional formations (Weijermars et al., 2025). These solutions for the estimation of storage capacity can now also be used with probabilistic estimations of storage capacity based on probabilistic inputs for permeability and porosity, and their correlation as determined in Section 4.4. Thus, armed with the permeability transforms produced probabilistically using only limited source data, one may classify P90-P50-P10 reserves in hydrocarbon extraction projects, as well as P90-P50-P10 storage capacity in geological carbon sequestration projects, as required by the respective SPE reporting frameworks (PRMS, 2024; SRMS, 2024).

5.4. Strengths, limitations and future research directions

At this stage, the provided solution and methodology seem to hold great promise for practical application. Initially developed for application in porosity-permeability transforms for rocks, the application potential may reach far beyond reservoir engineering purposes. At present, no specific application limitations are known. Application in mechanical engineering, chemical engineering, biological and medical studies may be possible, but are not further explored in the present work.

5.4.1. Expansion to non-clastic rocks

The present study focused on the analysis of porosity-permeability transforms for clastic rocks (sandstones and shale), for which a suitable and substantial series of data sets was available to the author (Appendix A). Another major rock type forming important reservoir rocks is comprised of carbonates (Lucia, 1995, 1999). Carbonates host some of the world's largest oil and gas reserves, but these are primarily developed by national oil companies. Unfortunately, national oil companies are reluctant to participate in the data-driven research advances, because they do not routinely share drill-core data with other research institutions. However, the present methodology will likely be suitable and applicable to construct porosity-permeability transforms for carbonate reservoirs.

5.4.2. Anisotropic permeability

The model can be readily applied to the estimation of transversely isotropic permeability by choosing two elementary volumes parallel to and perpendicular to the plane of isotropy. Fig. 12a and b showed typical shale micrographs, the principal factor changing is again the permeability-reduction factor, which normal to the foliation will have much longer time of flight. The importance of scaling such anisotropic permeability has been demonstrated in several prior studies (Weijermars and Khanal, 2019; Nandlal and Weijermars, 2019).

5.4.3. Single phase flow versus relative permeability

The present study focused on absolute permeability estimations, which apply to single phase flow without capillary pressure effects. For multi-phase flow, capillary pressure effects, varying with fluid saturation of the pore space, will start to impact the relative permeability curves. Having the absolute permeability constrained, one may attempt reconstructing relative permeability curves based on capillary pressure relationships, wettability, and pore morphology. For example, the ratio of fluid surface contact area and fluid volume will vary for different pore shapes. Fig. 26 shows that the ratio of pore space surface area to fluid volume decreases for pore space closer to spherical shapes. The graph also shows how the surface area of the pores in contact with a fluid increases when pore network spaces change from spherical, via polyhedron approximations of the sphere, when they become progressively confined by fewer surfaces. It can be mathematically shown that a dodecahedron leaves 33.5% space when fit inside the tightest sphere, while a icosahedron leaves slightly more free space (around 39.5%).

Exposure of fluids to surface area of a pyramid (or very angular pore spaces with many acute inner angles) is substantially larger (Fig. 26) than for the same fluid volume in spherical pores. Consequently, reservoir fluids moving through pore shapes being angular (pyramidal) will have a much larger interfacial contact line with the pore space than for spherical pores. One may conjure that multi-phase flow effects will be more pronounced in angular pore spaces as compared to cylindrical and spherical pores.

6. Conclusions

This study introduced a novel approach for estimating permeability in porous media, aiming to overcome the limitations of existing methods. Permeability, a crucial parameter in various engineering applications, reflects the ability of a material to transmit fluids under pressure gradients. While traditional methods often require cumbersome flow-tests or rely on simplified geometric inputs, the proposed approach introduces an improved theoretical framework based on pore-tube flow dynamics and geometric characterization of pore morphology. The proposed solution adapts to varied pore geometries, including elliptical, triangular, and rectangular shapes, while addressing limitations of traditional methods. Its ability to handle complex pore geometries and produce reliable permeability estimates for various geological formations makes the proposed model a valuable tool for hydrocarbon production and carbon sequestration projects. In addition, the probabilistic permeability-porosity data generation method, first developed in this study, supports the probabilistic classification of reserves and storage capacity, compliant with reporting frameworks such as PRMS (2024) and SMRS (2024), while reducing reliance on extensive core sample testing.

A key contribution of this study is challenging the classical view that porosity is a strong predictor of permeability. Instead, it highlights the importance of the permeability-reduction factor, which accounts for pore blockage and tortuosity, as a more important and more accurate determinant. The observed weak correlation between porosity and permeability in clastics such as GAB sandstones and shales is contrasted with Fontainebleau sandstones, where an apparent correlation is attributed to minimal pore blockage. The results reaffirm the relative robustness in connecting permeability values to the physical nature of the permeability-reduction factor β/τ. This factor and the new conceptional model for its explanation (Section 5.2) compares favorably to prior scaling parameters. In combination with Monte Carlo simulation, use of β/τ can regenerate accurate porosity-permeability transforms even for challenging materials like shale, where permeability measurement resolution is low. The importance of these advancements is underscored by their practical value for optimizing hydrocarbon production and reducing laboratory analysis reliance.

The study identifies depositional facies and diagenetic compaction as primary factors influencing permeability variation in clastic rocks. It categorizes facies into sandstone and shale types, with permeability ranges of mDarcy for sandstone and nanoDarcy for shale, reflecting principal differences in pore diameters. The conceptual model accounts for basin-centered and marginal differences in diagenesis, offering a detailed framework for understanding permeability variation in reservoir rocks.

Key insights highlighted in the present study are: The introduction of the permeability-reduction factor, β/τ, which combines hydraulically effective pore space and tortuosity. This factor inversely relates to the time-of-flight of fluid transfer, providing insights into macroscopic permeability. The method is validated using comprehensive permeability transforms from various sandstone and shale formations, demonstrating its applicability across different geological facies. By integrating theoretical insights with core data, and history matching the new derived analytical model against the empirical data, the proposed method offers a robust framework for estimating permeability in geological porous media.

The proposed methodology offers broad utility across disciplines, from reservoir engineering to mechanical, chemical, and biological studies. While initially focused on clastic rocks, future applications could include carbonates. The model is extendable to anisotropic permeability estimation and multi-phase flow, incorporating capillary pressure and wettability effects. For example, angular pore spaces exhibit more pronounced multi-phase flow effects due to larger fluid-wall interfacial areas.

CRediT authorship contribution statement

Ruud Weijermars: Writing – review & editing, Writing – original draft, Visualization, Validation, Supervision, Software, Resources, Project administration, Methodology, Investigation, Funding acquisition, Formal analysis, Data curation, Conceptualization.

Compliance with ethical standards

Author affirms adherence to the ethical standards of journal publication.

Data availability

Data and code relating to this work are proprietary.

Declaration of competing interest

The author declares that he has no known competing financial interests or personal relationships that could have appeared to influence the work reported in this paper.

Acknowledgements

The author acknowledges the generous support provided by the College of Petroleum Engineering & Geosciences (CPG) at King Fahd University of Petroleum & Minerals (KFUPM).

List of acronyms and variables

Acronyms

GAB	Great Australian Basin
KC	Kozeny-Carman
RQI	Reservoir Quality Index

Greek symbols

α	Shape factor
β	Coefficient of hydraulically effective pore space
β/τ	Permeability-reduction factor
$\partial_i P$	Pressure gradient elements
ΔP	Pressure difference
∇P	Pressure gradient operator
ϕ	Porosity
ϕ_{EFF}	Effective porosity
ϕ_{REG}	Regular porosity
ϕ_{UNC}	Unconnected porosity
μ	Dynamic viscosity
ρ	Density
τ	Tortuosity
ξ	Turbulence factor

Latin symbols

a, b, c	Pore dimensions
A	Typical pore cross-sectional area
B_0	Formation volume factor
c_t	Total compressibility
c_e	Empirical pore cross-sectional area match parameter
c_f	KC scaling factor
d	Characteristic grain size
h	Thickness of reservoir
h_c	Height in triangular pore tube
k	Scalar permeability
k_{ij}	Permeability tensor
k_H	Layer-parallel permeability
k_V	Permeability perpendicular to bedding
L	Flow-path length
n	Dimensionless exponent
P	Pressure
P_0	Original reservoir pressure
$P(r)$	Pressure transient
q	Flux into well at reservoir level
q_{WH}	Well-rate at the wellhead
Q	Volume rate in Darcy and Poiseuille solutions
r	Radial coordinate; where specified equal to pore radius
r_{eff}	Effective hydraulic radius
r_p	Pore tube radius
r_w	Well radius
R	Correlation factor
R^2	Coefficient of determination
t	Time
u	Fluid velocity in pore tubes

Appendix A. Data sets used

A1. Sample series

This study used 13 proprietary data sets with a total sample size of 21,767 data pairs of porosity and permeability. The data were provided for research purposes. The values used were as provided by the companies and institutions listed in Table A1. For shale samples, the difference between 'dry' and 'as received' for shale permeability measurements is that ‘dry’ porosity is measured on rocks without any water or fluid in their pores, after heating up to 110 °C. Permeability and porosity values were determined by specialized petrophysical service companies (last column, Table A1). Porosity in conventional sandstone measured by traditional porosimetry commonly corresponds to total interconnected pore space, while porosity in shale is measured by the GRI method, which is assumed to correspond closer to total porosity (connected and unconnected).

Figs. 5, 10 and 11 were based on data sets selected from Table A1 as deemed practical for each of these figures. A complete set of transforms for non-GAB data is plotted in Fig. A1. The Great Australian Basin (GAB) data is plotted in Fig. A2. The GAB-formations include the Marburg, Winton, Evergreen, Boxvale, Precipice, Adori, Birkhead, Hutton, Westbourne, Mackunda, Poolowannan, Walloon, Springbok, Gubberamunda, Orallo, Bungil, Mooga, Blantyre, Gilbert, Helidon, Winton, Doncaster, Juandah, Taroom, Tangalooma, Cadna-Owie and Hooray sandstones. The most important aquifers of the system are the Cadna-Owie/Hooray Formations, for which a separate transform was plotted in Fig. A2.

In the course of this research, it became clear that (1) the geological facies due to depositional environment and (2) the diagenetic mineral alterations during the burial history play a major role in where the porosity-permeability transform of a rock will plot in the PPT-field of Figs. A1 and A2**;** for details, see Section 5.4.

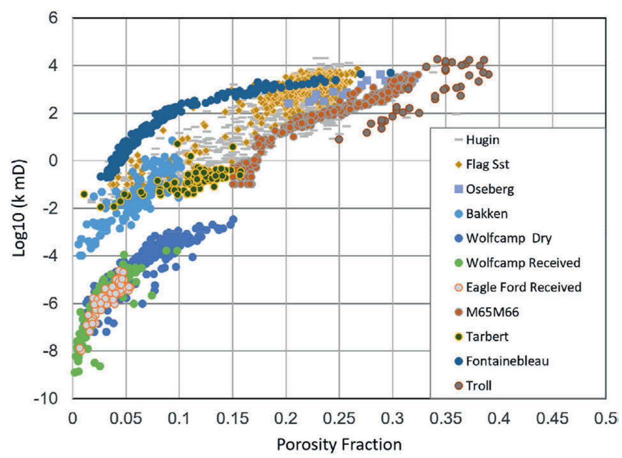

Fig. A1. Porosity-permeability transforms for unconventional shale formations and conventional sandstone formations.

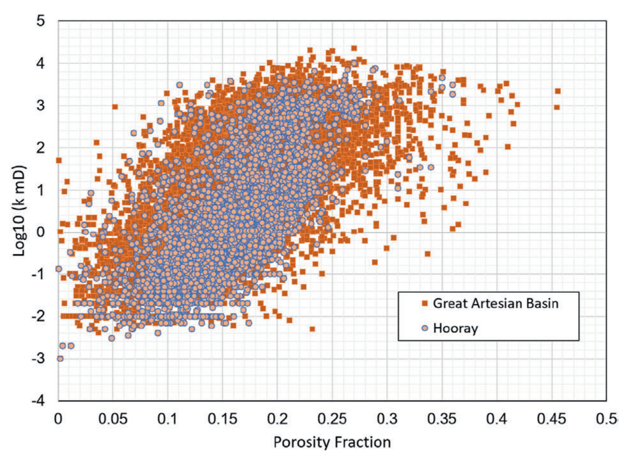

Fig. A2. Porosity-permeability transforms for conventional sandstones in the Great Australian Basin, with the Hooray Formation separately marked.

The Flag Sandstone Formation is part of the Barrow Group occurring in the Barrow Basin (NW Australia). The formation has an average porosity of 0.22 and permeability of 800 mDarcy to 5 Darcy (Boer and Collins, 1988; Gibson-Poole, 2009). With increasing depth of burial, early micritic siderite was partially recrystallized, and kaolinite formed as a pore filling and lining

Table A1
Data sets used for constructing porosity-permeability transforms.

Set	Reference Name	Nr. of Data	Location	Company/ Institution	Petrophysical Analysis
Conventionals					
1	Oseberg	17	NCS, Norway	Equinor	Ingrain
2	Troll	38	NCS, Norway	Equinor	Ingrain
3	Hugin	687	NCS, Norway	Equinor	Ingrain
4	Tarbert	79	NCS, Norway	OMV	Stratum
5	M65M66	335	US Gulf	BP	Schlumberger
6	Flag Sandstone	1079	Barrow Basin, Australia	Chevron	N/A
7	Fontainebleau	165	France	Stanford	Schlumberger
8	Hooray	3672	GAB, Australia	RESFAC	N/A
9	Great Artesian Basin	14,974	GAB, Australia	RESFAC	N/A
	SubTotal	21,046			
Unconventionals					
10	Bakken	138	North Dakota, US	Marathon	Weatherford
11	Eagle Ford Received	77	East Texas, US	Marathon	Weatherford
12	Wolfcamp Dry	388	West Texas, US	Pioneer	CoreLab
13	Wolfcamp Received	118	West Texas, US	Pioneer	CoreLab
	SubTotal	721			

phase, both before and synchronous with authigenic quartz. The depositional environment is syn-rift to post-rift turbidites which has been analyzed in great detail (Paumard et al., 2018).

The Oseberg and Tarbert Formations (Oseberg Field) are both part of the Brent Group, Norwegian Continental Shelf (Helland-Hansen et al., 1992). Both formations are part of a fan-delta depositional complex. The sandstones grade from fine-to medium-grained, locally calcite-cemented rocks with subordinate, thin siltstones, mudstones and coals.

The Hugin Formation (Middle Jurassic) is part of the Vestland Group. The depositional environment was a transgressive syn-tectonic deposit during rifting and subsidence. The flooding of the graben system created the ‘Brent Delta’ mega-sequence (Kieft et al., 2010). Fig A3 shows thin sections with coarse angular mineral fragments locally blocking flow paths. There occur complex spatial variations in facies within the Hugin Formation.

The Miocene M65-M66 sandstone (Horn Mountain Field, Gulf of Mexico) results from diagenetic alterations of rocks with well-connected intergranular macro-pores at shallow depth (where total porosity tends to be high) to poorly connected moldic pores at greater depth (where total porosity and permeability are much reduced) (Ehrenberg, 1990; Ehrenberg et al., 2008; Loucks et al., 1984; Nelson, 1994). The sands have been originally deposited in a deep water turbidite channel-levee-overbank system during the Lower to Middle Miocene (Ardo and Aminu, 2018). Fig A4 shows a thin section of relatively good reservoir quality rock.

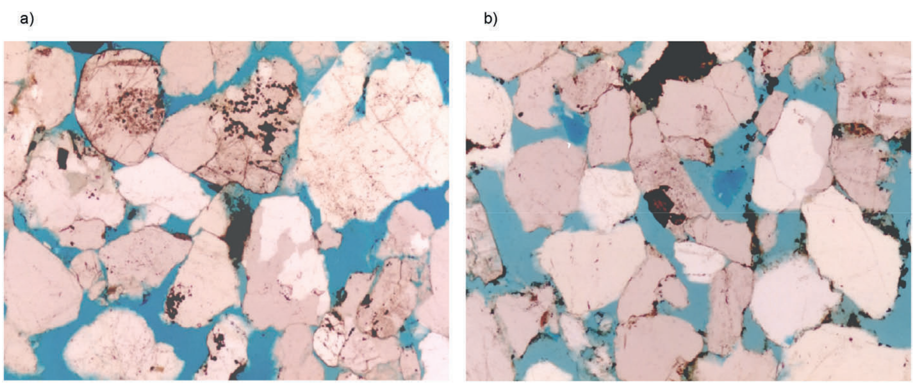

Fig. A3. (a,b) Micrographs of Hugin core samples (Volve Field; courtesy Equinor). Field of view scale length is about 1 mm. Blue shaded regions are pore space.

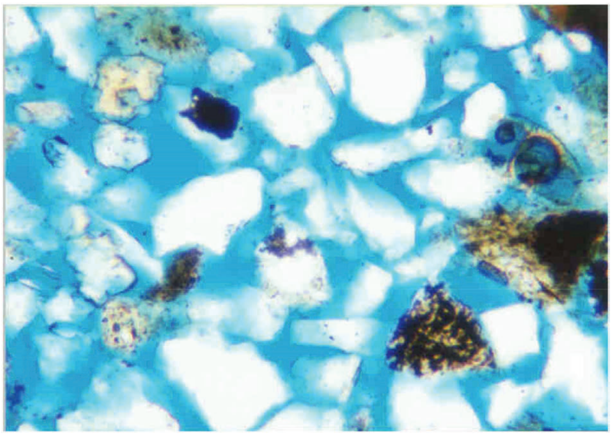

Fig. A4. Micrographs of core sample M65-M66 sandstone (Horn Mountain Field; courtesy BP). Field of view scale length is about 1 mm. Blue shaded regions are pore space.

The Fontainebleau Formation (Fig. A5) comprises very pure quartz sandstones (99% Quartz) with no clay minerals present, which explains its good pore connectivity. Variation in porosity was accomplished over geologic time by dissolution and precipitation of silica from mobile pore fluids (Fredrich et al., 1993), as well as by mechanical compaction (Song and Renner, 2008). Pore-throat diameter ranges from 16 to 30 μm (Al-Saadi et al., 2017). The standard deviation for the triangular distributions is 1.67.

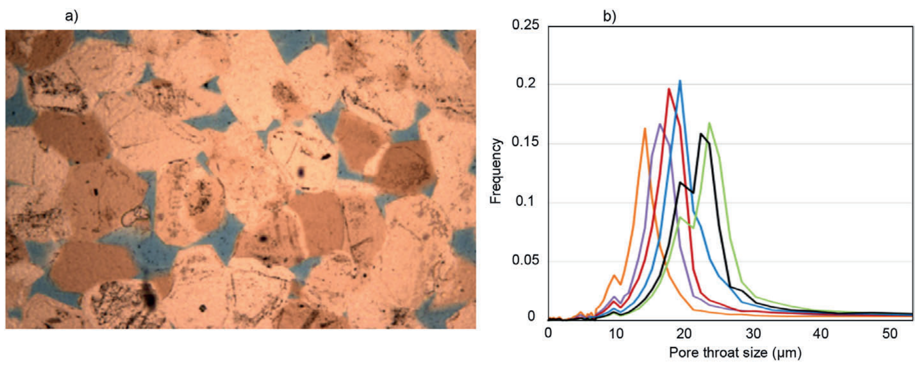

Fig. A5. (a) Micrograph of Fontainebleau sandstone; blue shaded regions are pore space. Field of view scale length is about 1 mm. (from Al-Saadi et al., 2017). (b) Pore-throat size from Mercury injection capillary pressure (from Al-Saadi et al., 2017).

The Hooray sandstone (Early Cretaceous) is the principal aquifer in the Great Artesian Basin (GAB), and is comprised of transgressive valley fill sands (Gorter, 1994). The GAB covers more than 1.7 million km^2 of eastern Australia, with rocks formed 65–250 million years ago and has both aquifers and aquitards (Fig. A6).

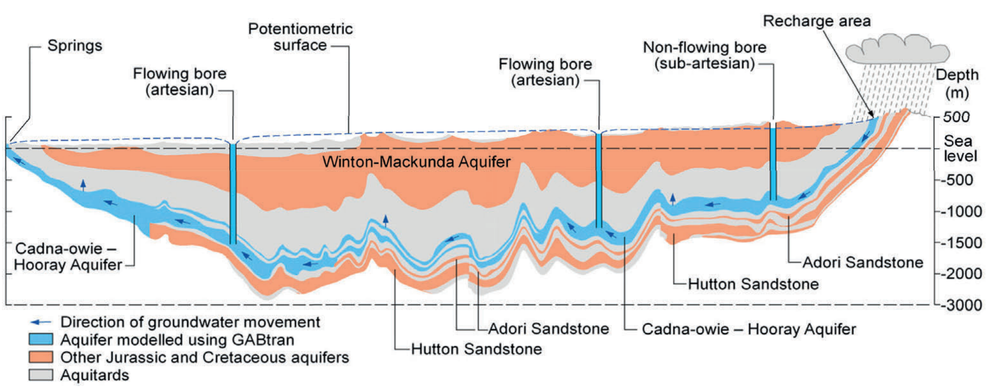

Fig. A6. Schematic section of the Great Artesian Basin with aquifers of Jurassic and Cretaceous sandstone beds (blue), and aquitards (grey), and other aquifers (orange). Vertical scale is exaggerated (after Radke et al., 2000).

The Bakken is best described as an argillaceous limestone. Brief geological descriptions for each of the three shale formations are given in prior studies: Bakken (Weijermars et al., 2017a), Eagle Ford (Weijermars et al., 2017b), and Wolfcamp (Wang and Weijermars, 2019). The triangular pore-size distributions for these formations (Fig. A7) range between 3 and 300 nm (Liu et al., 2017; Liu et al., 2018).

effective radii of 0.3–10 μm, and 0.12–3.5 μm for Sheia Formation rocks. These values actually confirmed that pore size values commonly vary over just two orders of magnitude. However, pore-sizes in clastic rocks are not uniformly distributed between the minimum and maximum, but typically show a strong clustering around a mean value in a triangular distribution, with little standard deviation (less than 1.33 in examples of Fig. A7). This means about 75% of the data differ less than ± 133% from the mean value,

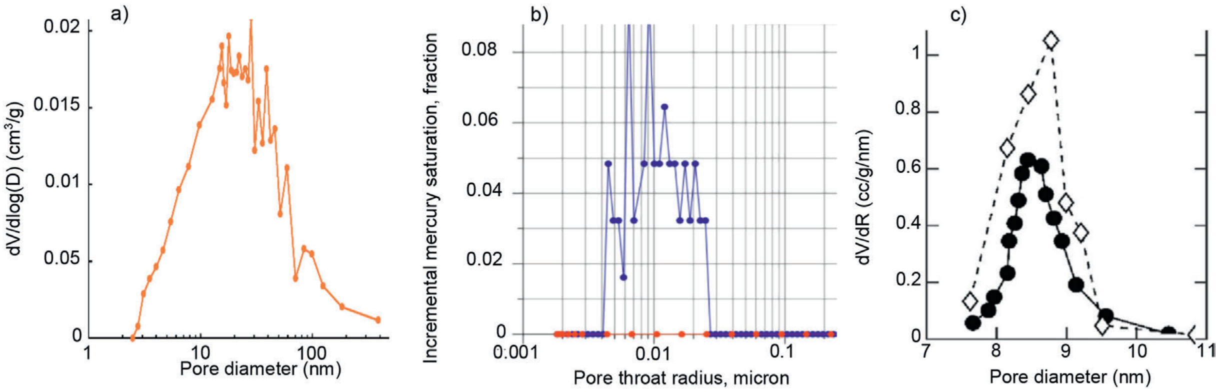

Fig. A7. Pore-throat size from Mercury injection capillary pressures. (a) Middle Bakken ranges between 0.002 and 0.1 μm (Liu et al., 2018). (b) Eagle Ford ranges between 0.002 and 0.03 μm (Cho et al., 2016). (c) Wolfcamp shale (Ojha et al., 2017). The respective standard deviations are (a) 1.33, (b) 1.17, and (c) 0.17.

A2. Impact of pore size variability

The pore-size distribution of Fontainebleau sandstone varies in a triangular distribution between a minimum of 10 μm and maximum value of 30 μm, with a mean value of 20 μm and standard deviation of 1.67 (Fig. A5b). The pore shape factor α has been physically constrained to vary for circular and triangular pores between 0.44 and 0.25 (Table 4). Consequently, neither A nor α can explain why Fontainebleau sand's permeability would vary over 5 orders of magnitude. For Bakken and Eagle Ford shale, the pore-size distributions cluster around 0.01 μm with standard deviations 1.17 and 1.33 (Figs. A7a,b). The recommended α-value for shale is 0.125 (Table 4). Consequently, the limited variation in A and α cannot explain the observed permeability ranges over 7 orders of magnitude, between 10^{-9} and 10^{-2} mDarcy (Fig. 5). Therefore, the permeability-reduction factor ($\beta/\ \tau$)-values must provide the root cause for the observed permeability range, and thus are pre-eminent predictors of permeability.

The pore size in the present study were gleaned from two sources:

- Pore size variation of individual samples based on Mercury saturation. Fig. A8 gives examples of the cumulative distribution of pore sizes for two distinct Bakken shale samples, each having a mean pore size of 20 μm based on 118 data points.
- Micro-graphs of core samples, allowing for visual inspection of pore size using the scale of the micrographs. Such micrographs were readily available to the author and confirmed the clustering around the mean - values used in this study.

One reviewer contended that the use of a typical pore-size would be a strong simplification that does not correspond to reality, quoting his own samples: Nubia Formation rock with

which is the rationale for not using probabilistic inputs for pore sizes in the analysis of Section 4.3. To demonstrate the validity of the claimed insensitivity to the limited standard deviation from the mean pore size, the Bakken permeability transforms were rerun, using the typical distribution of the pore size data fits of Fig. A8. The simulation output was visually indistinguishable from the ones shown in Fig. 20. The reason being, again, that the pore-size distribution between the extremes is not uniform but strongly clustering around the mean value, as apparent from the standard deviation of 0.35 (computed with excel) for each of the data sets in Fig. A8.

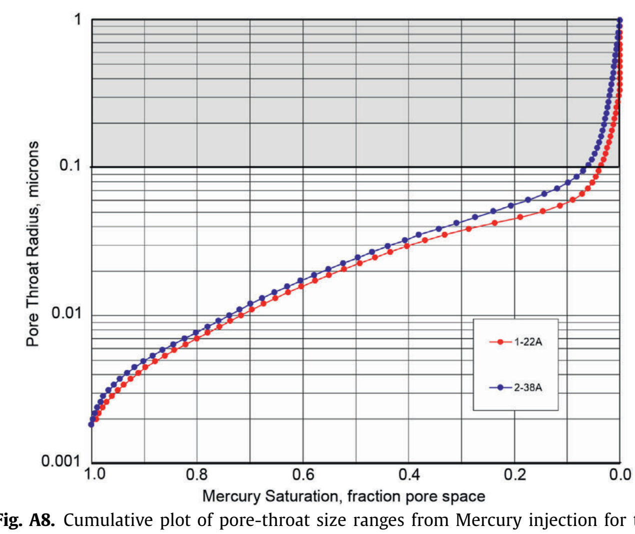

Fig. A8. Cumulative plot of pore-throat size ranges from Mercury injection for two Bakken shale samples (Mountrail County, North Dakota, US). Sample 1–22A is from a well-depth of 11,201 ft and Sample 2–38A from 11,276 ft. Despite of 75 ft sample spacing, pore-size distributions in the two samples are nearly identical. Also, 95% of the pores range between 2 and 100 μm, with the P50 mean at 20 μm, excluding the less than 5% data in the grey-shaded upper part of the graph. Courtesy Marathon Oil.

Appendix B. Darcy's Law and the introduction of squared tortuosity by some authors in Kozeny-Carman transforms

The literature on Kozeny-Carman (KC) type transforms at some point adopted a vision that a squared tortuosity should be included. Kozeny (1927) defined tortuosity ($\tau = L'/L$) and did not use a squared tortuosity. However, Carman (1937) introduced a squared tortuosity when analyzing the internal flow rate in the porous medium (see also Bear, 1972). Paterson (1983) posited the incorporation of a squared tortuosity in permeability transforms, which was subsequently followed by some petrophysicists (Costa, 2006; Pape et al., 1987; Peshtani et al., 2024; Peters et al., 2023).

During the review process of the present paper, the use of a square tortuosity was mandated by a reviewer, claiming it would be physically more correct to do so. It appears the review of Clennell (1997) is still timely; different measures of tortuosity are employed in various disciplinal contexts and differences in use and interpretation will persist. The present author shows a squared tortuosity comes only into permeability transform equations if permitting a physically unwarranted adaptation of Darcy's Law. This appendix aims to clarify when the squared tortuosity arises, starting from basic principles, and depending on choices made.

B1. Darcy's Law, fluid flow rates, and permeability

Darcy introduced a macroscopic measure for permeability. His apparatus uses a pressure difference, ΔP, between the two ends of the porous medium through which fluid flows in steady state during the experiment. Crucially, the macroscopic gradient, ∇P, is assumed invariant:

$$\nabla P = \frac{\Delta P}{L} \tag{B1}$$

where L is invariably assumed the macroscopic straight distance between the two ends of the Darcy apparatus where the different pressures are maintained. Darcy's Law, as used by ground water specialists and petroleum engineers, uses the macroscopic length L to determine the macroscopic flux q out of the total area at the outer end of the porous medium:

$$q = \frac{k}{\mu}\frac{\Delta P}{L} \tag{B2}$$

The gradient ∇P is the macroscopic gradient that proportionates the macroscopic flux out of the porous core plug or sand core to a permeability, k, given a certain viscosity, μ, of the fluid moving through the core:

$$k = \frac{q\mu}{\nabla P} \tag{B3}$$

The value of Darcy's Law is that the production rate of wells (water, oil and/or gas) can be computed with it, where the porous structure of the medium (ending against the free surface of the wellbore) is entirely scaled by the a permeability scalar, k (if anisotropic it will be a tensor quantity k_{ij}).

Critically, Darcy's definition of ∇P in Eq. (B1) means that for the macroscopic flux and definition of k, the pore structure of the porous medium is not considered. However, if one is not only interested in the flux into the well at the open end of the porous reservoir, but also likes to study the core's internal fluid velocity, u_r, and in the reservoir space, we need to introduce the effective porosity, ϕ, for which case Darcy's Law can be modified into (Woessner and Poeter, 2020; Zimmerman, 2018):

$$u_r = \frac{k}{\mu\phi}\nabla P \tag{B4}$$

The solution of Eq. (B4) is well-known among modelers of fluid flow in porous media and is based on Dupuit's relation $q = \phi u_r$ and replacing q by the right-hand side of Eq. (B2). Importantly, u_r is the internal velocity through the reservoir but along an assumed straight travel path if we assume the pressure gradient to consistently act unidirectionally.

If locally less porous, the porous medium transports the same macroscopic flux according to Darcy's Law (Eq. (B2)) but achieves this by flowing faster internally through pore spaces that are locally narrower, with higher flow velocity, which will be achieved due to the internal pressure gradient being locally larger in such narrower pore spaces (see Eq. (B4)). The pressure gradient inside a core plug tested with Darcy's apparatus will locally vary with porosity, but keeps the pressure difference at the two ends of the porous medium constant; the macroscopic ∇P remains unchanged. For a systematic understanding of how porosity changes internal flow rates and stream paths, the reader is referred to Zuo and Weijermars (2018).

Eq. (B4) is valid for steady-state flow, which ignores the transient flow occurring when the pressure transient still diffuses into the reservoir (or porous medium like sand as used in Darcy's original test apparatus). Such transient pressure propagation can be quantified using solutions of the diffusion equation for a variety of well configurations (Weijermars, 2021, 2022; Weijermars and Afagwu, 2024). Both transient and steady-state flow models incorporate the effective porosity in the modified Darcy Law of Eq. (B4) to model fluid flow in the reservoir.

B2. Kozeny's tortuosity

The pertinent equations for the KC-type transforms in this study use the original definition of tortuosity by Kozeny (1927) in the following key steps:

$$\text{Hagen} - \text{Poiseuille}: \frac{\nabla P}{\tau} = \frac{-8\pi\mu}{\pi r^4}u_c \tag{B5}$$

$$\text{Darcy's Law}: \frac{\nabla P}{\phi} = \frac{-\mu}{k\pi r^2}u_c \tag{B6}$$

Here the flow rate u_c inside a single capillary is conditioned such that originally $u_c = u_r$, and the tortuosity is factored into Eq. (B5), which applies to the case of Fig. 9b (illustrated in the main text); Eq. (6) of the main text needs to use $\frac{\nabla P}{\tau}$ on the left-hand side. However, for Darcy's Law, the tortuosity may not feature; one needs to use $\frac{\nabla P}{\phi}$ on the left-hand side of Eq. (7), as shown in Eq. (B6); both Eqs. (B5) and (B6) assume $\nabla P = \Delta P/L$, as per Eq. (B1).

The pressure gradient acts on the pore scale and therefore Q for both Darcy and Poiseuille are equal; effectively equating Eqs. (B5) and (B6) gives:

$$k = \frac{r^2}{8\tau}\phi \tag{B7}$$

Eq. (B7) is considered here the physically correct scaling of the permeability.

B3. Using squared tortuosity in permeability transforms

There is a decisive step when introducing a squared tortuosity in KC-type transforms; the squared tortuosity arises when Darcy's Law of Eq. (B4) is altered into:

$$u_c = \frac{k}{\mu\phi}\frac{\Delta P}{L'} = \frac{k\tau}{\mu\phi}\nabla P \tag{B8}$$

L' is now assumed a new length, through the tortuous capillary tubes of the flow. However, this is not how Darcy's Law defined Q. Eq. (B8) effectively multiplies the macroscopic gradient $\nabla P = \Delta P/L$ with a non-dimensional factor τ over which the linear gradient is contorted by tortuosity; now Darcy's equation is no longer a macroscopic measure (unlike that what was intended when permeability was defined by Darcy). In this approach of Paterson (1983), ∇P in both Poiseuille and Darcy's Law is implied to be equal to $\Delta P/L'$.

Classical Darcy flow always uses for the gradient the macroscopic ∇P as defined in Eq. (B1), where the length L is invariably the minimum distance across the porous medium across which the pressure difference exists. Only with this consistent approach can meaningful macroscopic permeability be defined from the Darcy apparatus test. The present author therefore uses Eq. (B4) for KC-type of permeability transfer derivations, which does not result in a squared tortuosity.

The squared tortuosity introduced by Paterson (1983) and followed by numerous petrophysicists (Costa, 2006; Pape et al., 1987; Peshtani et al., 2024; Peters et al., 2023) arises when instead of Eq. (B4) one uses Eq. (B8) as a starting point to derive KC-type of permeability transforms, in combination with the Hagen-Poiseuille equation for this case:

$$\text{Hagen} - \text{Poiseuille} : u_c = \frac{\pi r^4}{-8\pi\mu}\frac{\Delta P}{L'} = \frac{\pi r^4}{-8\pi\mu}\frac{\Delta P}{\tau} \tag{B9}$$

A squared tortuosity arises when one equates u_c of Eqs. (B8) and (B9), which gives:

$$k = \frac{r^2}{8\tau^2}\phi \tag{B10}$$

The solution of Eq. (B10) is here considered physically incorrect, because it is based on an erroneous use of Darcy's Law; one should not use Eq. (B8); only Eq. (B6) is correct. Using Eq. (B8) for Darcy's Law violates Darcy's definition of permeability as the macroscopic property resulting from the porous media test with the gradient given by the pressure differential divided by the shortest distance between the two ends of the test apparatus. The present author is of the opinion that using Eq. (B7) is correct, and Eq. (B10) incorrect. This appendix is an attempt to clarify, based on sincere reasoning, the contrarian points of view.

Finally, the dispute seems rather pointless, because everything stated in the present paper will conform to the view followed by the squared tortuosity 'school' if instead of using $k = \frac{r^2}{8\tau}\phi$ as in Eq. (B7) one uses the squared tortuosity factor, $k = \frac{r^2}{8T}\phi$, with $T = \tau^2$ as defined; everything stated in this study will equally apply.

Appendix C. Constructing porosity-permeability transforms by Monte-Carlo simulation

The construction of synthetic porosity-permeability transforms for Eagle Ford shale based on a limited number of measured data pairs was outlined in Section 4.4 of the main text. The original data sets, although containing significant sample size (see Table 3), can be augmented by (1) fitting the primary data for porosity and permeability to closely fitting distribution functions, (2) determining the correlation factors, and (3) running a Monte-Carlo simulation with a large number of iterations to create a solutions cloud showing the full statistical spread of the residual uncertainty in the porosity-permeability transform. The procedure, described here, was newly developed by the author and has not been published before.

A probabilistic method can regenerate porosity-permeability transforms based on the two sample sets (see workflow below). First one fits continuous probability distributions to the each of the data sets (*i.e.*, porosity and permeability) using, for example, @Risk software. Next, one regenerates new correlated data point pairs by Monte-Carlo simulation, seeding random variates to resample the distributions in any number of desired iterations; each iteration regenerates one new data pair. While Section 4.4 showed how the input distributions for porosity, permeability factor and shape factor (Table 9) can be used to construct synthetic porosity-permeability transforms, here we show examples of using (ϕ_{REG}, k)-data pairs to generate synthetic transforms populated by large data sets.

C1. Workflow Monte-Carlo simulation

The workflow description is as follows:

A. Data handling

(1) Start out with real data pairs of porosity and permeability (assume these are calibrated from laboratory measurements on core plugs).
(2) Select an appropriate continuous distribution with least error fit on the real data for porosity.
(3) Select an appropriate continuous distribution with least error fit on the real data for permeability.
(4) Cross check with Excel correlation matrix on the real data (of Step 1) for correlation coefficient.
(5) Include a correlation coefficient matrix – based on the established correlation between the real data (Step 4) – in the previously obtained least error fit distributions of porosity (Step 2) and permeability (Step 3).

B. Simulation

(6) Run iterative Monte-Carlo simulations to generate new pairs of plausible data pairs of porosity and permeability by randomly recombining samples from the two correlated continuous distributions for porosity and permeability (Step 5).
(7) Plot in the same plot both the real (original) data pairs (Step1) and the data pairs regenerated by simulation (Step 6).
(8) Add in the plot (of Step 7) trend lines for both the real (original data) pairs and the data pairs regenerated by simulation.
(9) Compare the regressions and coefficient of determination for each of the two pairs of data sets to check for match quality.

C2. Oseberg sandstone (North Sea, Norwegian Continental Shelf)

The data set is listed in Appendix A, Table A1. The fits to the binned real data (blue) by the selected cumulative uniform distributions (red) are given in Figs. C1a,b for respectively porosity and permeability (Steps 2 and 3). Using excel, $R^2 = 0.853$ (Step 4). The two final correlated distributions are constrained (Step 5) by Table C1.

Table C1
Correlated distribution functions used for generating the synthetic porosity-permeability transforms of Fig. C2.

Parameters	Type	Distribution	Unit
ϕ_{REG}	Probabilistic	RiskUniform (0.19491,0.32799,RiskTruncate (0.2,0.32),RiskName ("Phi_PDF"),RiskCorrmat (NewMatrix1,1))	–
k	Probabilistic	RiskUniform (2.3426,3.7051,RiskTruncate (2.4,3.6),RiskName ("log10 (k_mD)"),RiskCorrmat (NewMatrix1,2))	mDarcy
Coefficient of determination	R^2	0.853	–

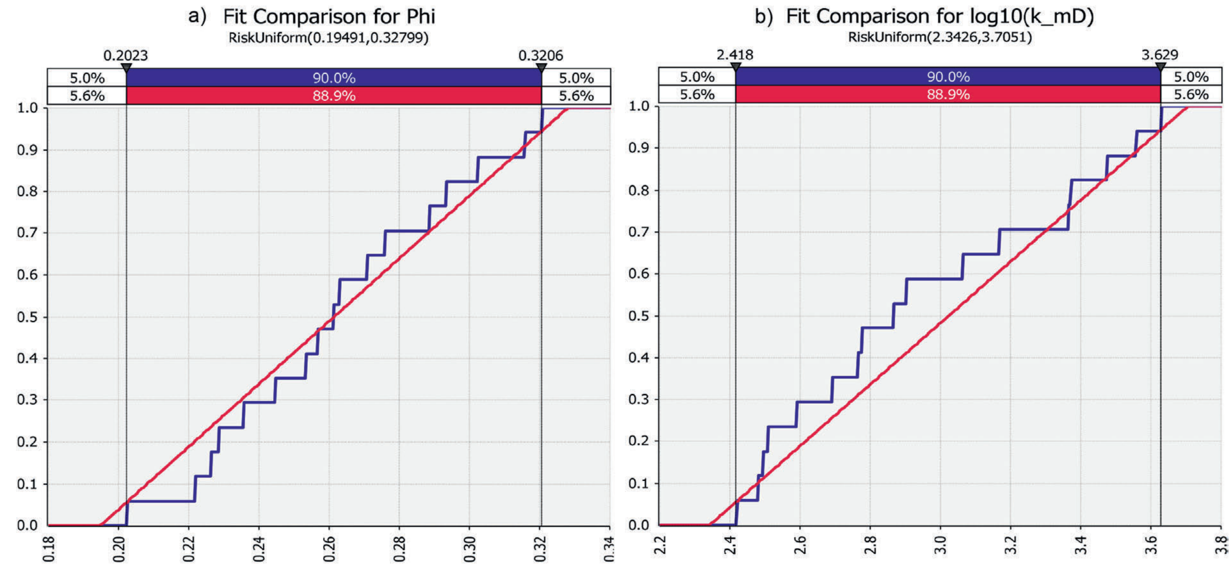

Fig. C1. The 17 data pairs for Oseberg sandstone are fit with cumulative distribution functions for (a) porosity, and (b) permeability. Both data sets are best fit by uniform distributions.

Adding the correlation is essential, as follows from below outputs. Fig. C2a shows both the real (original) data pairs (Step 1) and the synthetic data pairs regenerated by simulation (Step 6) accounting for the correlation (Step 5). The match between the regression lines of the simulated and real data is deemed reasonable (Step 9, see regression data in boxes of graph Fig. C2). However, if the simulation is run without correlations, the match will be very poor (Fig. C3). The recreated data for porosity and permeability appear in the right range, but the data pairs are totally randomly correlated as follows from $R^2 \rightarrow 0$ (0.088) for the simulated data set.

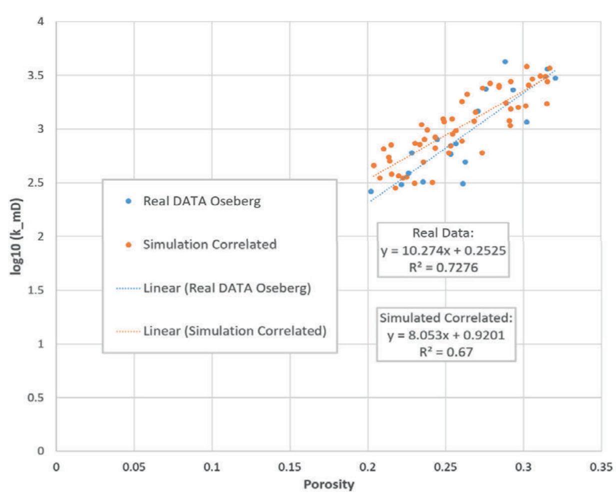

Fig. C2. Measured (blue dots) and recreated data pairs (red dots) for Oseberg sandstone. Their respective trend lines have comparable coefficients of determination $R^2 = 0.73$ and 0.67.

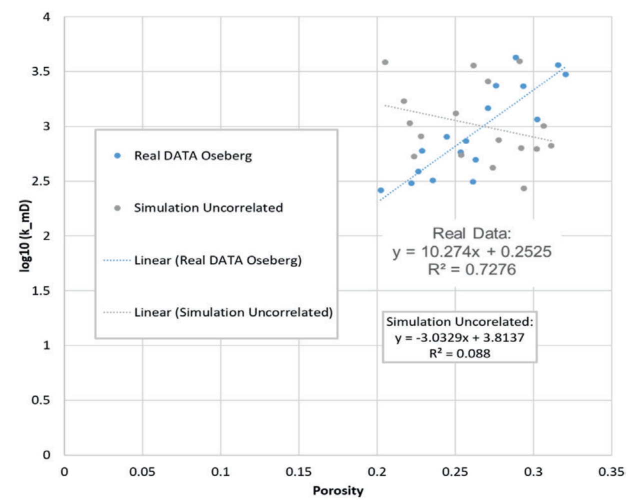

Fig. C3. Oseberg sandstone. If no correlation is used between the individual distribution functions of porosity and permeability, the trend line of the recreated data is strongly misaligned relative to the trend line of the actual data.

C3. Troll Sandstone (North Sea, Norwegian Continental Shelf)

The data set is listed in Appendix A, Table A1. The fits to the binned real data (blue) by the selected cumulative triangular distributions (red) are given in Figs. C4a, b for respectively porosity and permeability (Steps 2 and 3). Using excel, $R^2 = 0.87$ (Step 4). The two final correlated distributions are constrained (Step 5) by Table C2.

Table C2
Correlated distribution functions used for generating the synthetic porosity-permeability transforms of Fig. C5.

Parameters	Type	Distribution	Unit
ϕ_{REG}	Probabilistic	RiskTriang (0.23642,0.39000,0.39000,RiskCorrmat (NewMatrix2,1))	–
k	Probabilistic	RiskTriang (0.39937,4.2480,4.2480,RiskCorrmat (NewMatrix2,2))	mDarcy
Coefficient of determination	R^2	0.678	–

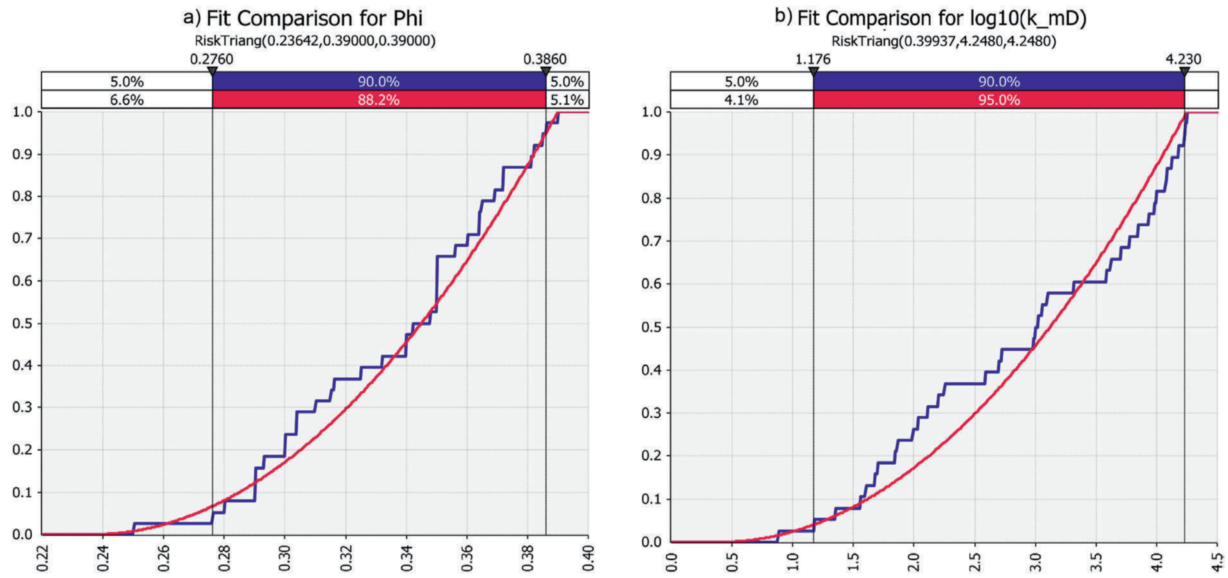

Fig. C4. The 38 data pairs for Troll sandstone are fit with cumulative distribution functions for (a) porosity, and (b) permeability. Both data sets are best fit by triangular distributions.

Fig. C5 shows both the real (original) data pairs (Step1) and the data pairs regenerated by simulation (Step 6) accounting for the correlation (Step 5). The match between the regression lines of the simulated and real data is deemed reasonable (Step 9, see regression data in boxes of graph Fig. C5).

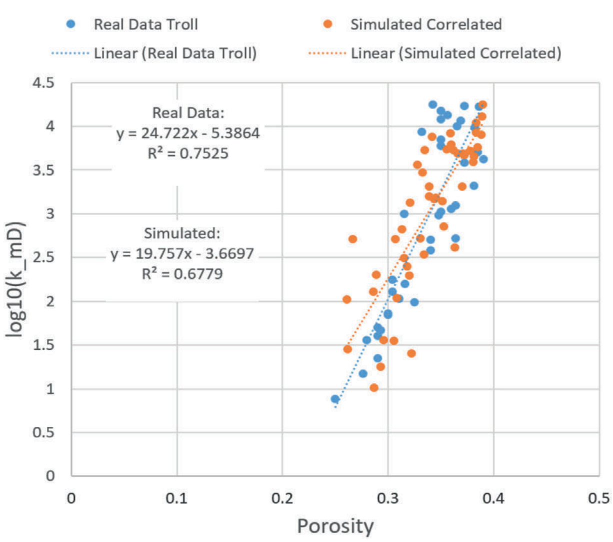

Fig. C5. Measured (blue dots) and recreated data pairs (red dots) for Troll sandstone. Their respective trend lines have comparable coefficients of determination $R^2 = 0.753$ and 0.678.

C4. Fontainebleau sandstone

The data set is listed in Appendix A, Table A1. The Fontainebleau porosity-permeability transform (Fig. 16a, main text) can be partitioned into two domains, comprising porosities respectively larger than 0.1 and smaller than 0.1. Each of the two domains was analyzed separately. The lower porosity domain fits to the binned real data (blue) by the selected cumulative triangular and uniform distributions (red) are given in Figs. C6a,b for respectively porosity and permeability (Steps 2 and 3). Using excel, $R^2 = 0.97$ (Step 4). The two final correlated distributions are constrained (Step 5) by Table C3.

Table C3
Correlated distribution functions used for generating the synthetic porosity-permeability transforms of Fig. C7.

Parameters	Type	Distribution	Unit
ϕ_{REG}	Probabilistic	RiskTriang (0.025699,0.037700,0.106000, RiskCorrmat (NewMatrix2,1))	–
k	Probabilistic	RiskUniform (-0.72911,2.2791, RiskCorrmat (NewMatrix2,2))	mDarcy
Coefficient of determination	R^2	0.928	–

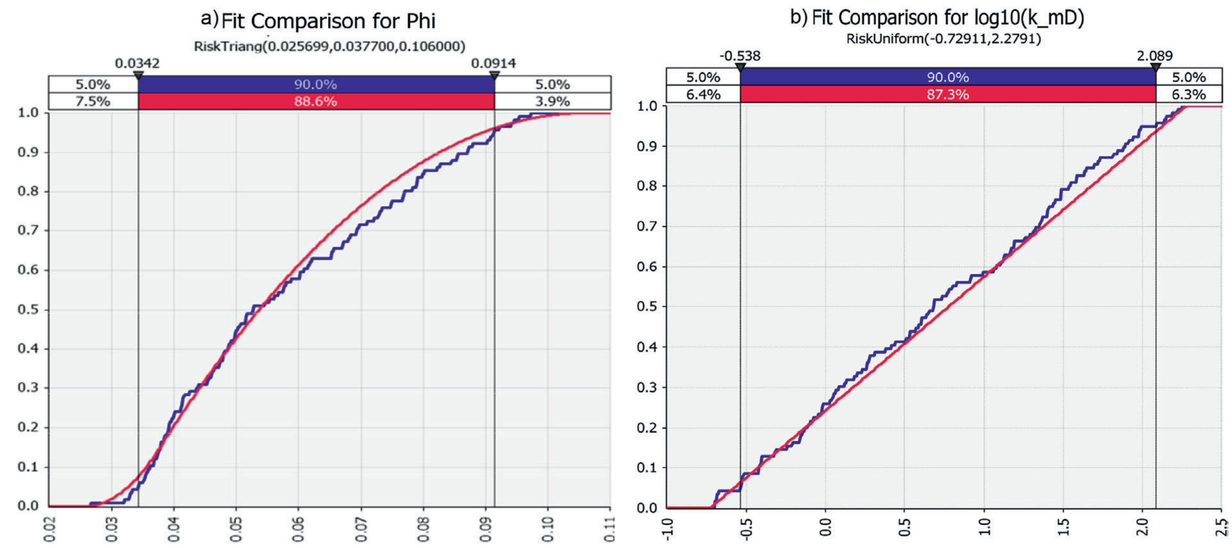

Fig. C6. Data pairs for Fontainebleau sandstone with ϕ_{REG} <0.1 fit with cumulative distribution functions for (a) porosity, and (b) permeability. The porosity is best fit by a triangular distribution, and the permeability by a uniform distribution.

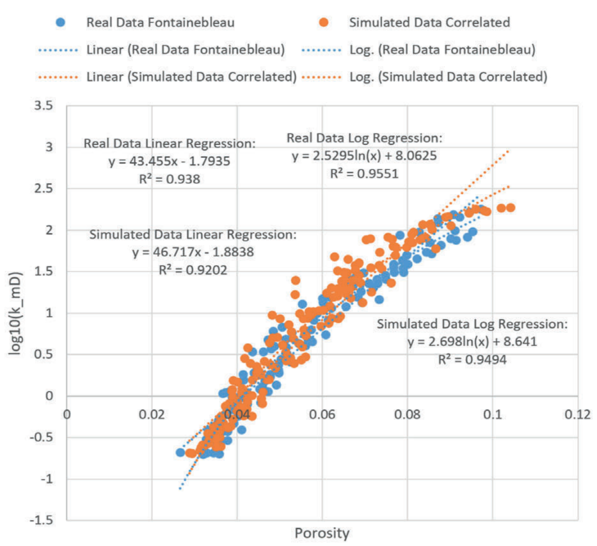

Fig. C7. Measured (blue dots) and recreated data pairs (red dots) for Fontainebleau sandstone with ϕ_{REG} <0.1. Their respective trend lines have comparable coefficients of determination $R^2 = 0.955$ and 0.949.

Fig. C7 show the real (original) data pairs (Step1) and the data pairs regenerated by simulation (Step 6) accounting for the correlation (Step 5). The match between the regression lines of the simulated and real data is deemed reasonable (Step 9, see regression data in the graph).

The higher porosity domain fits to the binned real data (blue) by the selected cumulative Weibull and Normal distributions (red) are given in Figs. C8a,b for respectively porosity and permeability (Steps 2 and 3). Using excel, $R^2 = 0.94$ (Step 4). The two final correlated distributions are constrained (Step 5) by Table C4.

Table C4
Correlated distribution functions used for generating the synthetic porosity-permeability transforms of Fig. C9.

Parameters	Type	Distribution	Unit
ϕ_{REG}	Probabilistic	RiskWeibull (2.0552,0.096091, RiskShift (0.090271),RiskCorrmat (NewMatrix3,1))	–
k	Probabilistic	RiskNormal (2.94807,0.35381, RiskCorrmat (NewMatrix3,2))	mDarcy
Coefficient of determination	R^2	0.897	–

Fig. C9 show the real (original) data pairs (Step1) and the data pairs regenerated by simulation (Step 6) accounting for the correlation (Step 5). The match between the regression lines of the

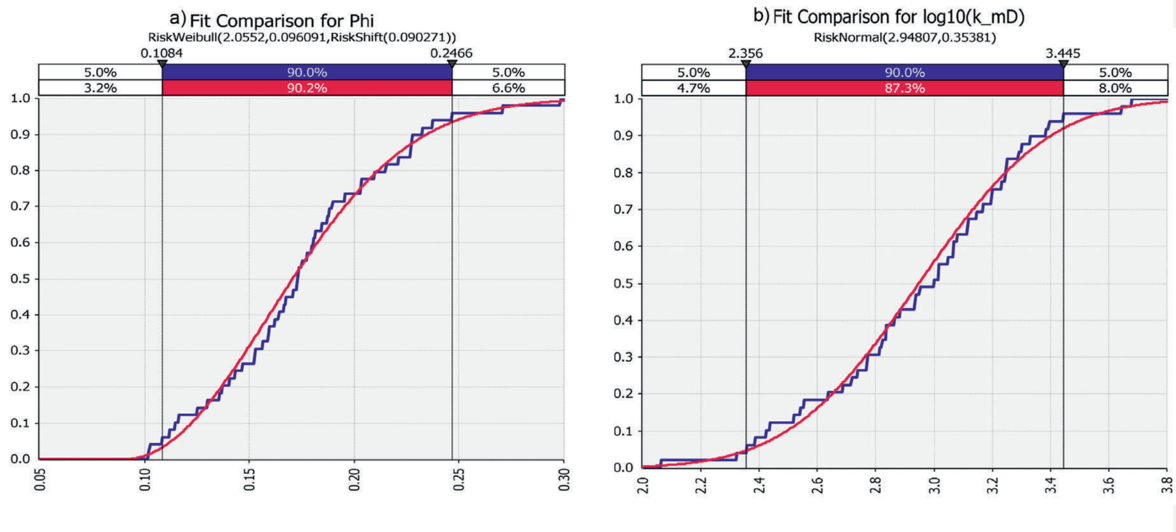

Fig. C8. Data pairs for Fontainebleau sandstone with ϕ_{REG} >0.1 fit with cumulative distribution functions for (a) porosity, and (b) permeability. The porosity is best fit by a Weibull distribution, and the permeability by a normal distribution.

simulated and real data is deemed reasonable (Step 9, see regression data in boxes in the graph).

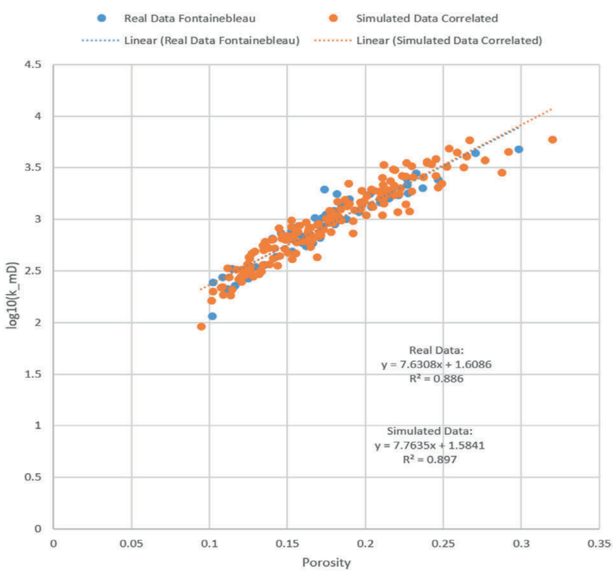

Fig. C9. Measured (blue dots) and recreated data pairs (red dots) for Fontainebleau sandstone with ϕ_{REG} >0.1. Their respective trend lines have comparable coefficients of determination R^2 = 0.886 and 0.897.

References

Afagwu, C., Weijermars, R., 2024a. Sensitivity analysis of CO2-Migration paths in geological carbon-dioxide sequestration: case study of the Gorgon GCS project. SSRN. https://doi.org/10.2139/ssrn.4985775.

Afagwu, C., Weijermars, R., 2024b. Rapid well-test analysis based on Gaussian pressure-transients. Geoenergy Sci. Eng. 241, 213168. https://doi.org/10.1016/j.geoen.2024.213168.

Al-Saadi, F., Wolf, K., Kruijsdijk, C.V., 2017. Characterization of fontainebleau sandstone: Quartz overgrowth and its impact on pore-throat framework. J. Petrol Environ. Biotechnol. 7, 328. https://doi.org/10.4172/2157-7463.1000328.

Al-Shaikh, A., Weijermars, R., 2025. Fast Analysis Method of Diag nostic Fracture Injection Test Data: Examples from Four Different Shale Formations (Bakken, Three Forks, Wolfcamp, and Eagle Ford). In: SPE Hydraulic Fracturing Conference 2025, SPE 226622-MS.

Alpak, F.O., Riviere, B., Frank, F., 2016. A phase-field method for the direct simulation of two-phase flows in pore-scale media using a non-equilibrium wetting boundary condition. Comput. Geosci. 20, 881–908.

Alvayed, D., Khalid, M.S.A., Dafaalla, M., Ali, A., Ibrahim, A., Weijermars, R., 2023. Probabilistic estimation of hydraulic fracture half-lengths: validating the Gaussian pressure-transient method with the traditional RTA-method (Wolfcamp case study). J. Pet. Explor. Prod. Technol. https://doi.org/10.1007/s13202-023-01680-9.

Amaefule, J.O., Altunbay, M., Tiab, D., Kersey, D.G., Keelan, D.K., 1993. Enhanced reservoir description: using core and log data to identify hydraulic (flow) units and predict permeability in uncored intervals/wells. In: SPE Annual Technical Conference and Exhibition.

Ardo, B.U., Aminu, M.D., 2018. Reservoir description of the Middle Miocene M sand, horn Mountain field. Oil Gas Res. 4, 155. https://doi.org/10.4172/2472-0518.1000154.

Bear, J., 1972. Transport in Porous Media. Dover Publications, New York.

Bernabé, Y., Mok, U., Evans, B., 2003. Permeability-porosity relationships in rocks subjected to various evolution processes. Pure Appl. Geophys. 160, 937–960. https://doi.org/10.1007/PL00012574.

Boer, R., de Collins, L.B., 1988. Petrology and diagenesis of the flag sandstone, harriet field, barrow sub-basin. In: the north west shelf Australia. In: P.G, Purcell, R.R. (Eds.), Proceedings of Petroleum Exploration Society Australia Symposium, pp. 225–236. Perth.

Bourbie, T., Zinszner, B., 1985. Hydraulic and acoustic properties as a function of porosity in Fontainebleau sandstone. J. Geophys. Res. 90, 11524–11532.

Campos, M., Jenssen, M., Michelen, M., Sahasrabudhe, J., 2023. A New Lower Bound for Sphere Packing arXiv:2312.10026 [math.MG].

Cao, G., Jiang, W., Chao, L., Lili, C., Zhuo, C., Mian, L., Xing, H., 2024. Permeability anisotropy and non-darcy effect of gas shale: a case study of S1111-1 sublayer of longmaxi formation in Sichuan basin, China. SSRN. https://doi.org/10.2139/ssrn.5001896. https://ssrn.com/abstract=5001896or.

Carbillet, L., 2022. From grains to rocks: the evolution of hydraulic and mechanical properties during diagenesis (Thesis). Université de Strasbourg.

Carman, P.C., 1937. Fluid Flow Through Granular Beds. Transactions, vol. 15. Institution of Chemical Engineers, London, pp. 150–166.

Carman, P.C., 1938a. Fundamental Principles of Industrial Filtration (A Critical Review of Present Knowledge). Transactions, vol. 16. Institution of Chemical Engineers, London, pp. 168–188.

Carman, P.C., 1938b. Determination of the specific surface of powders I. Transactions. Journal of the Society of Chemical Industries 57, 225–234.

Carman, P.C., 1939. Permeability of saturated sands, soils and clays. J. Agric. Sci. 29, 263–273.

Carman, P.C., 1956. Flow of Gases Through Porous Media. Butterworths, London.

Chapman, R.E., 1981. Geology and Water: an Introduction to Fluid Mechanics for Geologists. Martinus Nijhoff, The Hague.

Chapuis, R.P., Aubertin, M., 2003. On the use of the Kozeny–carman equation to predict the hydraulic conductivity of soils. Can. Geotech. J. 40, 616–628. https://doi.org/10.1139/T03-013.

Chen, F., Lu, S., Ding, X., Zhao, H., Ju, Y., 2019. Total porosity measured for shale gas reservoir samples: a case from the Lower Silurian longmaxi formation in southeast chongqing, China. Minerals 9 (1), 5. https://doi.org/10.3390/min9010005.

Cheng, Z., Ning, Z., Wang, Q., Zeng, Y., Qi, R., Huang, L., Zhang, W., 2019. The effect of pore structure on non-Darcy flow in porous media using the lattice boltzmann method. J. Petrol. Sci. Eng. 172, 391–400. https://doi.org/10.1016/j.petrol.2018.09.066.

Cho, Y., Eker, E., Uzun, I., Yin, X., Kazemi, H., 2016. Rock Characterization in Unconventional Reservoirs: a Comparative Study of Bakken, Eagle Ford, and Niobrara Formations. SPE Low Perm Symposium, Denver, Colorado, USA.

Clennell, M.B., 1997. Tortuosity: a guide through the maze. Geol. Soc. Spec. Publ. 122, 299–344.

Costa, A., 2006. Permeability-porosity relationship: a reexamination of the Kozeny-Carman equation based on a fractal pore-space geometry assumption. Geophys. Res. Lett. 33 (2), L02318. https://doi.org/10.1029/2005GL025134.

Darcy, H., 1856. Les Fontaines Publiques De La Ville De Dijon : Exposition Et Application Des Principes À Suivre Et Des Formules À Employer Dans Les Questions De Distribution D'Eau. Recherche.

Delplace, F., 2018. Laminar flow of Newtonian liquids in ducts of rectangular cross-section: a model for both physics and mathematics. J. Math. Theor. Phys. 1 (5), 198–201.

Ehrenberg, S.N., 1990. Relationship between diagenesis and reservoir quality in sandstones of the Garn formation, Haltenbanken, Mid-Norwegian continental shelf. AAPG (Am. Assoc. Pet. Geol.) Bull. 74, 1538–1558.

Ehrenberg, S.N., Nadeau, P.H., Steen, Ø., 2008. A megascale view of reservoir quality in producing sandstones from the offshore Gulf of Mexico. AAPG (Am. Assoc. Pet. Geol.) Bull. 92 (2), 145–164. https://doi.org/10.1306/09280707062.

Ekre, P.C., 2015. Petrographic Evaluation of the Middle Jurassic Sandstones of the Brent Group, North Sea A Petrographic Study of the Ness, Etive and Rannoch Formations (Master Thesis). University of Olso.

Finney, J., 1970. Random packing and the structure of simple liquids .I. the geometry of random close packing. Proceedings of the Royal Society 319, 479–493.

Frank, F., Liu, C., Alpak, F.O., Berg, S., Riviere, B., 2018a. Direct numerical simulation of flow on pore-scale images using the phase-field method. SPE J. 23, 1833–1850.

Frank, F., Liu, C., Alpak, F.O., Riviere, B., 2018b. A finite volume/discontinuous Galerkin method for the advective Cahn–Hilliard equation with degenerate mobility on porous domains stemming from micro-CT imaging. Comput. Geosci. 22, 543–563.

Frank, F., Liu, C., Scanziani, A., Alpak, F.O., Riviere, B., 2018c. An energy-based equilibrium contact-angle boundary condition on jagged surfaces for phase-field methods. J. Colloid Interface Sci. 523, 282–291.

Fredrich, J.T., Greaves, K.H., Martin, J.W., 1993. Pore geometry and transport properties of Fontainebleau sandstone. International Journal of Rock Mechanics and Mining Sciences & Geomechanics 30 (7), 691–697. https://doi.org/10.1016/0148-9062(93)90007-Z.

Gibson-Poole, C.M., 2009. Site Characterization for Geological Storage of Carbon Dioxide: Examples of Potential Sites from Northwest Australia (Ph.D. Thesis). University of Adelaide, Adelaide, Australia, p. 258.

Goral, J., Panja, P., Deo, M., Andrew, M., Linden, S., Schwarz, J.O., Wiegmann, A., 2020. Confinement effect on porosity and permeability of shales. Sci. Rep. 10, 49. https://doi.org/10.1038/s41598-019-56885-y.

Gorter, J.D., 1994. Sequence stratigraphy and the depositional history of the Murta member (Upper Hooray Sandstone), SE Eromanga basin, Australia: implications for the development of source and reservoir facies. APPEA Journal 34, 644–673. https://doi.org/10.1071/AJ93049.

GRI (Gas Research Institute), 1996. Development of Laboratory and Petrophysical Techniques for Evaluating Shale Reservoirs (Final Technical Report). Gas Research Institute.

Guo, B., 2019. In: Well Productivity Handbook, second ed. Elsevier.

Hales, T.C., 2005. A proof of the Kepler conjecture. Ann. Math. 162, 1065–1185.

Hall, A., Gillespie, M., Everett, P., Christodoulou, V., Walsh, J., 2022. Machine learning applied to pore-space geometry in sandstones: a tool for evaluating grain-scale similarity? Q. J. Eng. Geol. Hydrogeol. 55 (1). https://doi.org/10.1144/qjegh2020-183.

Helland-Hansen, W., Ashton, M., Lomo, L., Steel, R., 1992. Advance and retreat of the Brent delta: recent contributions to the depositional model. In: Morton, A. C., Haszeldine, R.S., Giles, M.R., Broom, S. (Eds.), Geology of the Brent Group, vol. 61. Geological Society Special Publication, pp. 109–127.

Henderson, N., Brêttas, J.C., Sacco, W.F., 2010. A three-parameter Kozeny–Carman generalized equation for fractal porous media. Chem. Eng. Sci. 65 (150), 4432–4442. https://doi.org/10.1016/j.ces.2010.04.006.

Horne, R.N., 2005. In: Modern Well Test Analysis, second ed. Petroway Inc., Palo Alto, California.

Hudson, D.R., 1949. Density and packing in an aggregate of mixed spheres. J. Appl. Phys. 20 (2), 154–162. https://doi.org/10.1063/1.1698327.

Jia, B., Jin, L., Smith, S.A., Bosshart, N.W., 2021. Extension of the gas research institute (GRI) method to measure the permeability of tight rocks. J. Nat. Gas Sci. Eng. 91, 103756. https://doi.org/10.1016/j.jngse.2020.103756.

Kassab, M.A., Weller, A., 2011. Porosity estimation from compressional wave velocity: a study based on Egyptian sandstone formations. J. Petrol. Sci. Eng. 78, 319. https://doi.org/10.1016/j.petrol.2011.06.011, 315.

Kassab, M., Weller, A., Abuseda, H., 2022. Integrated petrographical and petrophysical studies of sandstones from the Arab A formation for reservoir characterization. Arabian J. Geosci. 15, 944.

Kieft, R.L., Jackson, C.A.-L., Hampson, G.J., Larsen, E., 2010. Sedimentology and sequence stratigraphy of the Hugin formation, quadrant 15, Norwegian sector, South Viking Graben. Petroleum Geology Conference Series 7, 157–176. https://doi.org/10.1144/0070157.

Kozeny, J., 1927. Ueber kapillare Leitung des Wassers im Boden. Sitzungsberichte Wiener Akademie 136 (2a), 271–306.

Krause, M., Perrin, J.-C., Benson, S., 2011a. Recent progress in predicting permeability distributions for history matching core flooding experiments. Energy Proc. 4, 4354–4361. https://doi.org/10.1016/j.egypro.2011.02.387.

Krause, M., Perrin, J.C., Benson, S.M., 2011b. Recent progress in predicting permeability distributions for history matching core flooding experiments. Energy Proc. 4 (1), 4354–4361. https://doi.org/10.1016/j.egypro.2011.02.387.

Laat, de D., Oliveira, de F.M., Vallentin, F., 2014. Upper bounds for packings of spheres of several radii. Forum of Mathematics, Sigma 2 (e23). https://doi.org/10.1017/fms.2014.24.

Li, S., Zhao, J., Lu, P., Xie, Y., 2010. Maximum packing densities of basic 3D objects. Chin. Sci. Bull. 55, 114–119.

Liu, G., Ehlig-Economides, C., 2018. Practical considerations for diagnostic fracture injection test (DFIT) analysis. J. Petrol. Sci. Eng. 171, 1133–1140. https://doi.org/10.1016/j.petrol.2018.08.035.

Liu, K., Ostadhassan, M., Zhou, J., Gentzis, T., Rezaee, R., 2017a. Nanoscale pore structure characterization of the Bakken shale in the USA. Fuel 209, 567–578. https://doi.org/10.1016/j.fuel.2017.08.034.

Liu, L., Li, Z., Jiao, Y., Li, S., 2017b. Maximally dense random packings of cubes and cuboids via a novel inverse packing method. Soft Matter 13, 748. https://doi.org/10.1039/c6sm02065h.

Liu, Y., Shen, B., Yang, Z., Zhao, P., 2018. Pore structure characterization and the controlling factors of the bakken formation. Energies 11, 2879. https://doi.org/10.3390/en11112879.

Liu, L., Li, H., Zhou, H., Lin, S., Li, S., 2022. Design and application of a rock porosity measurement apparatus under high isostatic pressure. Minerals 12, 127. https://doi.org/10.3390/min12020127.

Lock, P.A., Jing, X.D., Zimmerman, R.W., Schlueter, E.M., 2002. Predicting the permeability of sandstone from image analysis of pore structure. J. Appl. Phys. 92, 6311–6319.

Loucks, R.G., Dodge, M.M., Galloway, W.E., 1984. Regional controls on diagenesis and reservoir quality in lower tertiary sandstones along the Texas Gulf Coast. In: McDonald, D.A., Surdam, R.C. (Eds.), Clastic Diagenesis, vol. 37. AAPG Memoir, pp. 15–45.

Lucia, F.J., 1995. Rock fabric/petrophysical classification of carbonate pore space for reservoir characterization. AAPG Bull. 79 (9), 1275–1300.

Lucia, F.J., 1999. Carbonate Reservoir Characterization. Springer-Verlag, Berlin, Heidelberg, New York, p. 226.

Luo, X., Zhao, Z., Zhang, L., 2021. Identification of oil produced from shale and tight reservoirs in the Permian lucaogou shale sequence, Jimsar Sag, Junggar Basin, NW China. ACS Omega 2021 (6), 2127–2142. https://doi.org/10.1021/acsomega.0c05224.

MaP Expert, 2015. Pore Space Quantification and Distribution in an organic-rich Shale. https://m-a-p.expert/assets/img/MaP-Application-Note-BIB-SEM-Shale-high-quality.pdf.

Marshall, G.W., Hudson, T.S., 2010. Dense binary sphere packings. Contrib. Algebra Geometry 51 (2), 337–344.

Mavko, G., Mukerji, T., Dvorkin, J., 2009. The Rock Physics Handbook. Cambridge University Press.

Mortensen, N.A., Okkels, F., Bruus, H., 2005. Reexamination of Hagen-Poiseuille flow: shape dependence of the hydraulic resistance in microchannels. Phys. Rev. E71, 057301. https://link.aps.org/doi/10.1103/PhysRevE.71.057301.

Nandlal, K., Weijermars, R., 2019. Impact on drained rock volume (DRV) of storativity and enhanced permeability in naturally fractured reservoirs: upscaled field case from hydraulic fracturing test site (HFTS), Wolfcamp formation, Midland basin, West Texas. Energies 12, 3852. https://doi.org/10.3390/en12203852.

Nelson, P.H., 1994. Permeability-porosity relationships in sedimentary rocks. Log. Anal. 35, 38–62.

Nelson, P.H., 2009. Pore-throat sizes in sandstones, tight sandstones and shale. AAPG (Am. Assoc. Pet. Geol.) Bull. 93 (3), 329–340. https://doi.org/10.1306/10240808059.

Nomura, S., Yamamoto, Y., Sakaguchi, H., 2018. Modified expression of Kozeny–Carman equation based on semilog–sigmoid function. Soils Found. 58 (6), 1350–1357. https://doi.org/10.1016/j.sandf.2018.07.011.

Ojha, S.P., Misra, S., Tinni, A., Sondergeld, C., Rai, R., 2017. Pore connectivity and pore size distribution estimates for Wolfcamp and Eagle Ford shale samples from oil, gas and condensate windows using adsorption-desorption measurements. J. Petrol. Sci. Eng. 158, 454–468. https://doi.org/10.1016/j.petrol.2017.08.070.

Oliver, D.S., Reynolds, A.C., Liu, N., 2008. Inverse Theory of Petroleum Reservoir Characterization and History Matching. Cambridge University Press.

Oquendo-Patiño, W.F., Estrada, N., 2020. Densest arrangement of frictionless polydisperse sphere packings with a power-law grain size distribution. Granul. Matter 22 (4). https://doi.org/10.1007/s10035-020-01043-9.

Pape, H., Riepe, L., Schopper, J., 1987. Theory of self-similar network structures in sedimentary and igneous rocks and their investigation with microscopical and physical method. J. Microsc. 148 (2), 121–147. https://doi.org/10.1111/j.1365-2818.1987.tb02861.x.

Pape, H., Clauser, C., Iffland, J., 1999. Permeability prediction based on fractal pore-space geometry. Geophysics 64, 1447–1460.

Paterson, M.S., 1983. The equivalent channel model for permeability and resistivity fluid-sturated rock – a re-appraisal. Mech. Mater. 2, 345–352.

Paumard, V., Bourget, J., Payenberg, T., Ainsworth, R.B., George, A.D., Lang, S., Posamentier, H.W., Peyrot, D., 2018. Controls on shelf-margin architecture and sediment partitioning during a syn-rift to post-rift transition: insights from the barrow group (Northern Carnarvon Basin, North West Shelf, Australia). Earth Sci. Rev. 177, 643–677. https://doi.org/10.1016/j.earscirev.2017.11.026.

Peshtani, K., Weller, A., Slater, L., 2024. Permeability and induced polarization of mudstones. Water Resour. Res. 60, e2024WR037455. https://doi.org/10.1029/2024WR037455.

Peszyński, K., Olszewski, L., Smyk, E., Perczyński, D., 2018. Analysis of the velocity distribution in different types of ventilation system ducts. EPJ Web Conf. 180, 02081. https://doi.org/10.1051/epjconf/201818002081.

Peters, A., Iden, S.C., Durner, W., 2023. Full prediction of unsaturated hydraulic conductivity - comparison of four different capillary bundle models. Hydrol. Earth Syst. Sci. https://doi.org/10.5194/hess-2023-134.

Phillips, O.M., 1991. Flow and Reactions in Permeable Rocks. Cambridge University Press.

PRMS, 2024. Call for Public Input for Possible Revisions of PRMS 2018 Petroleum Resources Management System. Society of Petroleum Engineers. https://jpt.spe.org/petroleum-resources-management-system-public-comments-period-open.

Profice, S., Lenormand, R., 2020. Low permeability measurement on crushed rock: insights. Petrophysics – The SPWLA Journal of Formation Evaluation and Reservoir Description 61 (2), 162–178. https://jgmaas.com/SCA/2019/SCA2019-016.pdf.

Radke, B., Ferguson, J., Creswell, R., Ransley, T., Habermehl, R., 2000. Hydrochemistry and Implied Hydrodynamics of the Cadna-owie – Hooray Aquifer. Australian Government Technical Report.

Rodrigues, S.J., Vorhauer-Huget, N., Richter, T., Tsotsas, E., 2023. Influence of particle shape on tortuosity of non-spherical particle packed beds. Processes 11. https://doi.org/10.3390/pr11010003.

Satter, A., Iqbal, G.M., 2015. Reservoir Engineering. Gulf Professional Publishing.

Saxena, N., Mavko, G., Hofmann, R., Srisutthiyakorn, N., 2017. Estimating permeability from thin sections without reconstruction: digital rock study of 3D properties from 2D images. Comput. Geosci. 102, 79–99. https://doi.org/10.1016/j.cageo.2017.02.014.

Schmitt Rahner, M., Halisch, M., Fernandes, C.P., Weller, A., Sampaio Santiago dos Santos, V., 2018. Fractal dimension of pore spaces in unconventional reservoir rocks using X-ray nano- and micro-computed tomography. J. Nat. Gas Sci. Eng. 55, 298–311. https://doi.org/10.1016/j.jngse.2018.05.011.

Sisavath, S., Jing, X.D., Zimmerman, R.W., 2001. Laminar flow through irregularly-shaped pores in sedimentary rocks. Transport Porous Media 45, 41–62.

Song, I., Renner, J., 2008. Hydromechanical properties of Fontainebleau sandstone: experimental determination and micromechanical modeling. J. Geophys. Res. 113, B09211. https://doi.org/10.1029/2007JB005055.

SRMS, 2024. Call for Public Input on SRMS Draft 6 of 2024 Revisions of SRMS 2017. https://www.spe.org/media/filer_public/6f/2f/6f2ff44b-abae-4894-821a-f17c35df22ea/srms_draft6_public_review.pdf.

Sun, S., Zhang, T., 2020. Reservoir Simulations. Machine Learning and Modeling. Gulf Professional Publishing.

Tugan, M.F., Weijermars, R., 2022. Searching for the root cause of shale well rate variance: highly variable fracture treatment response. J. Petrol. Sci. Eng. 210 (183), 109919. https://doi.org/10.1016/j.petrol.2021.109919.

Wang, J., Weijermars, R., 2019. Expansion of Horizontal Wellbore Stability Model for Elastically Anisotropic Shale Formations with Anisotropic Failure Criteria: Permian Basin Case Study. American Rock Mechanics Association, New York.

Weijermars, R., 2021. Diffusive mass transfer and Gaussian pressure transient solutions for porous media. Fluids 6 (11), 379. https://doi.org/10.3390/fluids6110379.

Weijermars, R., 2022. Production rate of multi-fractured Wells modeled with Gaussian pressure transients. J. Petrol. Sci. Eng. 210, 110027. https://doi.org/10.1016/j.petrol.2021.110027.

Weijermars, R., 2024. Fast production and water-breakthrough analysis methods demonstrated using volve field data. Petroleum Research 9 (3), 327–346.

Weijermars, R., Afagwu, C., 2024. Pressure-transient solutions for unbounded and bounded reservoirs produced and/or injected via vertical well-systems with constant bottomhole-pressures. Fluids 9 (9), 199. https://doi.org/10.3390/fluids9090199.

Weijermars, R., Khanal, A., 2019a. Elementary pore network models based on complex analysis methods (CAM): fundamental insights for shale field development. Energies 12, 1243. https://doi.org/10.3390/en12071243.

Weijermars, R., Khanal, A., 2019b. High-resolution streamline models of flow in fractured porous media using discrete fractures: implications for upscaling of permeability anisotropy. Earth Sci. Rev. 194, 399–448.

Weijermars, R., Paradis, K., Belostrino, E., Feng, F., Lal, T., Xie, A., Villareal, C., 2017a. Re-appraisal of the bakken shale play: accounting for historic and future oil prices and applying fiscal rates in North Dakota, Montana and Saskatchewan. Energy Strategy Rev. 16, 68–95.

Weijermars, R., Sorek, N., Seng, D., Ayers, W., 2017b. Eagle ford shale play economics: U.S. versus Mexico. J. Nat. Gas Sci. Eng. 38, 345–372.

Weijermars, R., Khanal, A., Zuo, L., 2020. Fast models of hydrocarbon migration paths and pressure depletion based on complex analysis methods (CAM): mini-review and verification. Fluids 5, 7. https://doi.org/10.3390/fluids5010007.

Weijermars, R., Afagwu, C., Tian, Y., Alves, I., 2025. Estimation of storage capacity coefficients: Porthos GCS project case study. Geoenergy Science and Engneering.

Weller, A., Slater, L.D., 2015. Induced polarization dependence on pore space geometry: empirical observations and mechanistic predictions. J. Appl. Geophys. 123, 310–315. https://doi.org/10.1016/j.jappgeo.2015.09.002.

Weller, A., Slater, L., Binley, A., Nordsiek, S., Xu, S., 2015. Permeability prediction based on induced polarization: insights from measurements on sandstone and unconsolidated samples spanning a wide permeability range. Geophysics 80 (2), D161–D173.

Woessner, W.W., Poeter, E.P., 2020. Hydrogeologic Properties of Earth Materials and Principles of Groundwater Flow. The Groundwater Project. https://gw-project.org/books/hydrogeologic-properties-of-earth-materials-and-principles-of-groundwater-flow/.

Wu, Y., Fan, Z., Lu, Y., 2003. Bulk and interior packing densities of random close packing of hard spheres. J. Mater. Sci. 38 (9), 2019–2025. https://doi.org/10.1023/A1023597707363.

Xiao, B., Huang, Q., Wang, Y., Chen, H., 2021. A fractal model for capillary flow through a single tortuous capillary with roughened surfaces in fibrous porous media. Fractals 29, 2150017. https://doi.org/10.1142/S0218348X21500171.

Yonghong, F., Yuqiang, J., Hu, C., Keming, Z., Xunxi, Q., Haijie, Z., Xiongwei, L., Yifan, G., Zengzheng, J., 2020. Analysis and enlightenment of porosity differences between shale plug samples and crushed samples. Petroleum Geology & Experiment 2, 302–310.

Zanganeh, B., Clarkson, C.R., Yuan, B., Zhang, Z., 2020. Field trial of a modified DFIT (pump-in/flowback) designed to accelerate estimates of closure pressure, reservoir pressure and well productivity index. J. Nat. Gas Sci. Eng. 78, 103265. https://doi.org/10.1016/j.jngse.2020.103265.

Zhang, Z., Weller, A., 2014. Fractal dimension of pore-space geometry of an Eocene sandstone formation. Geophysics 79, D377–D387.

Zhang, Z., Weller, A., Kruschwitz, S., 2017. Pore radius distribution and fractal dimension derived from spectral induced polarization. Near Surf. Geophys. 15, 625–632.

Zhang, H., Jiang, J., Zhou, K., Fu, Y., Zhong, Z., Zhang, X., Qi, L., Wang, Z., Jiang, Z., 2020. Connectivity of pores in shale reservoirs and its implications for the development of shale gas: a case study of the Lower Silurian long-maxi formation in the southern Sichuan basin. Nat. Gas. Ind. B 7 (4), 348–357. https://doi.org/10.1016/j.ngib.2019.12.003.

Zhao, C., Zhou, W., Hu, Q.H., Xu, H., Zhang, C., 2021. Porosity measurement of granular rock samples by modified bulk density analyses with particle envelopment. Mar. Petrol. Geol. 133, 105273. https://doi.org/10.1016/j.marpetgeo.2021.105273.

Zimmerman, R.W., 2018. Fluid flow in porous media. The Imperial College Lectures in Petroleum Engineering 5. https://doi.org/10.1142/q0146.

Zuo, L., Weijermars, R., 2018. 20178. Rules for flight paths and time of flight for flows in heterogeneous isotropic and anisotropic porous media. Geofluids (3), 1–18.